Development of low-scaling methods for the description of vibronic transitions and application in gas-phase ion chemistry

Dissertation zur Erlangung des Doktorgrades der Naturwissenschaften
vorgelegt beim Fachbereich Chemie der Philipps-Universität Marburg

von Sabrina Marquardt, M.Sc.
geboren in Hanau am Main

Marburg, 2018

eingereicht am 28.05.2018
bei der Philipps-Universität Marburg (Hochschulkennziffer 1180)
und vom Fachbereich Chemie als Dissertation angenommen.

Tag der Disputation: 17.10.2018
1. Gutachter: Prof. Dr. Robert Berger
2. Gutachter: Prof. Dr. Karl-Michael Weitzel

Abstract

Theoretical methods are developed and applied in relation to three gas phase experiments: Neutralization Reionization Mass Spectrometry (NRMS), laser cooling and Cold Target Ion Momentum Spectroscopy (COLTRIMS). All three are important techniques in gas phase ion chemistry research and can be described using similar theoretical models: The molecules under investigation undergo electronic transitions from an initial electronic state to a final electronic state and may at the same time also change their vibrational quantum number. Those vibronic transitions are in the Franck-Condon limit described with Franck-Condon factors (FCFs) which modulate the probability of the different electronic transitions.

Whereas in NRMS state transitions are used to generate highly reactive molecular species from stable precursors, laser cooling achieves translational cooling of molecules by repeated electronic transitions and COLTRIMS provides information on electronic and geometrical structure.

In this work a time-dependent generating function ansatz for the calculation of FCFs by Huh [PhD thesis, Johann Wolfgang Goethe-Universität Frankfurt am Main, **2010**] is extended in order to calculate vibrational population distributions in the final state after one or several subsequent vibronic transitions. The calculated trajectories are discontinuous in some cases, which makes it necessary to implement algorithmic changes to the former developments. The method is applied to the molecule HNSi and combined with reaction rate calculations within the Statistical Adiabatic Channel Model (SACM) to predict signals in the mass spectrum. The results are compared to NRMS experiments. An extended version of the developed method is discussed which includes the description of a laser excitation with specific frequency. It is applied to a system with one vibrational degree of freedom in a laser cooling cycle.

In the year 2013 Pitzer et al. [*Science* **2013**, *341* (6150), 1096 1100] have shown that direct assignment of the absolute configuration for the molecule CHBrClF is possible with COLTRIMS. In this dissertation experimental data from synchrotron experiments in the year 2016 by Pitzer et al. [*Chem. Phys. Chem.* **2016**, *17*, 24652472] are analysed. The uncertainty of their evaluation due to the presence of different isotopes is discussed. Equilibrium structures and stabilities of multiply

charged cations of CHBrClF are determined with quantum chemical methods. Furthermore, the fragmentation pathways of singly charged CDBrFI are investigated and calculated appearance energies are compared to experimental values.

This work describes methods for the prediction and analysis of three gas phase experiments that involve vibronic transitions. These theoretical approaches integrate different advantages: The methods developed or applied herein are predominantly of quantum mechanical type, which have inherently high accuracy. The algorithms implemented and the approaches used are computationally efficient as they avoid for instance to explicitly count vibronic transitions or to perform optimizations with overly expensive quantum chemical methods. The methods are versatilely applicable to diverse molecules in different gas phase experiments. Furthermore, this dissertation contributes to the further development of the promising COLTRIMS method for the direct determination of absolute configuration.

Contents

1 Introduction **12**

1.1 Motivation and Achievements 12

1.1.1 Neutralisation Reionisation Mass Spectrometry 13

Description of the experiment 13

Summary of my achievements 15

Other theoretical papers 15

1.1.2 Laser cooling 16

Description of the experiment 16

Summary of my achievements 18

Other theoretical papers 18

1.1.3 Cold Target Recoil Ion Momentum Spectroscopy 18

Description of the experiment 18

Summary of my achievements 19

Other theoretical papers 20

1.2 Outline of the Dissertation 21

2 Theoretical Background **22**

2.1 Assumptions 22

2.2 Calculation of Franck-Condon spectra 24

2.2.1 Normal coordinates and Duschinski rotation 24

2.2.2 Coherent states 27

2.2.3 Density of states 31

2.2.4 Franck-Condon approximation 33

2.2.5 Generating function 34

Generating function at 0 K 34

Generating function at finite temperature 36

Time-dependent ansatz 37

2.3 The Statistical Adiabatic Channel Model 39

2.3.1 Detailed Statistical Adiabatic Channel Model 39

2.3.2 Simplified Statistical Adiabatic Channel Model 41

3 Theoretical Developments and Results **43**
3.1 Population distributions for NRMS 44
3.1.1 Assumptions 44
3.1.2 Population distribution after neutralisation 44
3.1.3 Population distribution after reionisation 47
3.1.4 Practical realization 50
3.1.5 Two-dimensional model system 56
3.1.6 Population distributions for HNSi 59
3.2 Population distributions for Laser cooling 65
3.2.1 Assumptions 65
3.2.2 Population distribution as a function of laser frequency . . . 66
3.2.3 Population distribution as a function of laser frequency with an initial non-Boltzmann population distribution 67
3.2.4 Practical realization 68
First excitation with the laser 68
Relaxation from the excited state 69
Extrapolation 69
Second excitation with the laser 70
Further transitions 71
3.2.5 One-dimensional model system 72
3.3 Theoretical aspects of the COLTRIMS experiment 73
3.3.1 Statistical evaluation of COLTRIMS experiments 73
3.3.2 Multiply charged ion fragments of CHBrClF 77
3.3.3 Reaction pathways for Cold Target Ion Momentum Spectroscopy 81

4 Conclusion and Outlook **87**
4.1 Conclusions 87
4.2 Open questions 89

Appendices **91**

Bibliography **103**

Kurzfassung **109**

List of Figures

1.1 Scheme of an experimental setup for NRMS. 13
1.2 Scheme of vibronic transitions of a $^{-}NR^{+}MS$ experiment. 14
1.3 Equilibrium between the ketone and the enol form of neutral and cationic acetone. 15
1.4 Simplified scheme of laser cooling. 17
1.5 Experimental setup of Cold Target Ion Momentum Spectroscopy. . 19

2.1 Equilibrium and distorted structures of water. 24
2.2 Contour line plot of two harmonic oscillator potential energy surfaces. 26
2.3 One-dimensional coherent state function $\phi(y_0; y, t)$ with parameters: $\omega = 20\ \mathrm{s}^{-1}$, $y_0 = 1$. 28
2.4 Example for the construction of the density of states (DOS) of energy levels between $0\,\mathrm{cm}^{-1}$ and $500\,\mathrm{cm}^{-1}$. 32
2.5 Schematic drawing of vibrationally adiabatic potential curves. The channels with barriers below $E_{\max}$ are open and called reactive states. 41
2.6 Exemplary potential curve in the SACM. 42

3.1 Scheme of the model for Neutralization Reionization Mass Spectrometry (NRMS). 45
3.2 Riemann surface of the complex square root function. 51
3.3 Fourier transform of the Boltzmann distribution for different temperatures. 54
3.4 Population distribution calculated with the KDB algorithm (blue) and the time-dependent method using the expansion ansatz from equation (3.29) (red). 56
3.5 Vibrational population distribution for a two-dimensional system (see table 3.2) after the first transition. 58
3.6 Vibrational population distribution for a two-dimensional system (see table 3.2) after the second transition. 58
3.7 Vibrational population distribution of HNSi after the first transition. 60

3.8 Vibrational population distribution of $HNSi^{+\cdot}$ after the second transition. 61
3.9 Dissociation rates of neutral and cationic HNSi as a function of energy. 64
3.10 Vibrational population distribution for a one-dimensional system after one laser cooling cycle. 73
3.11 Determination of the cosine angle from the momentum vectors. . . 74
3.12 Kinetic energy release of detected particles in the events with four detected ions. 76
3.13 Kinetic energy release split into two monomodal distributions. . . . 77
3.14 Total kinetic energy release for the events with four and five detected particles. 77
3.15 Illustration of the formic acid motif in di- and tricationic structures of CHBrClF. 78
3.16 Selected dissociation pathways for the isomers of $CHBrClF^{+\cdot}$. . . . 79
3.17 Selected dissociation pathways for the isomers of $CHBrClF^{2+}$. . . . 80
3.18 Selected dissociation pathways for the isomers of $CHBrClF^{3+\cdot}$. . . . 81
3.19 Fragmentation pathways of $CDBrFI^{+\cdot}$ with cleavage of one bond and cleavage of two bonds, where one of them is between C and D. 82
3.20 Fragmentation pathways of $CDBrFI^{+\cdot}$ with cleavage of two bonds, where none is the C–D bond. Intermediate states were not calculated as they had no relevance for the resulting appearance energies. 82
3.21 Fragmentation pathways of $CDBrF^{+}$ with cleavage of one bond and cleavage of two bonds, where one is between C and D. 83
3.22 Intensity of the DI^{+} ion as a function of the electron-impact energy. 84

List of Tables

2.1 Symbols as used by Tannor and Heller in [1] and in this work. . . . 39

3.1 Integral values over the resulting population distribution according to equation (3.24) for a one-dimensional system with different temperatures for the Boltzmann distribution at the intermediate state. 53
3.2 Parameters for the two-dimensional test system. 57
3.3 Parameters for the calculation of vibrational population distributions for the $^{+}NR^{+}$ experiment on HNSi. 59
3.4 Parameters for the dissociation rate calculation with the simplified SACM. 62
3.5 Vibrational modes of HNSi, $HNSi^{+\cdot}$ and its fragments. 63
3.6 Parameters for the one-dimensional model system used in the calculation of vibrational population distributions for laser cooling. . . 72
3.7 Fraction of events with consistent sign for all triple products for fragmentation pathways with four detected ions. 75
3.8 Isotopic certainty of triple products. 76
3.9 Theoretical and experimental appearance energies for cationic fragments of $CDBrFI^{+\cdot}$. 85
3.10 Ionization energies from outer valence Green's function calculations, experimental ionization energies and assignments to molecular orbitals. 86

Acronyms

CIP Cahn-Ingold-Prelog. 73

COLTRIMS Cold Target Ion Momentum Spectroscopy. 2, 3, 12, 17, 18, 20, 38, 72, 74, 76, 79, 80, 87, 88

DFT density functional theory. 75, 78

DOS density of states. 6, 30–32

FC Franck-Condon. 14–17, 23, 33, 35, 43, 58, 61, 65, 88

FCF Franck-Condon factor. 2, 13, 14, 17, 33, 46

KDB Kemper-van Dijk-Buck. 15, 36, 46, 54–56, 59

KER kinetic energy release. 19, 72, 74–76, 87

NRMS Neutralization Reionization Mass Spectrometry. 2, 6, 12–17, 20, 38, 43, 44, 60, 61, 64, 66, 68, 72, 86–88

PES potential energy surface. 13, 24, 43, 80, 82

PIPICO photoion photoion coincidence. 79

RRKM Rice-Ramsperger-Kassel-Marcus. 19

SACM Statistical Adiabatic Channel Model. 2, 19, 38–40, 59, 60, 86, 99

Notation

This list gives the notation for general mathematical elements. It is not a complete list of all used symbols.

Vector	Vectors are denoted as $\underline{v} = \begin{pmatrix} v_1 \\ v_2 \\ \dots \\ v_N \end{pmatrix}$.
Ground State	Variables belonging to ground state properties are denoted without superscript.
Excited State	Variables belonging to excited state properties are denoted with apostrophe, e.g. v'.
Matrix	Matrices are typeset in bold. $\boldsymbol{I}$ is the identity matrix.
Transposition	The transpose vector of $\underline{v}$ is denoted as $\underline{v}^t$.
Diagonal matrix	The expression diag transforms a vector into a diagonal matrix with the elements of the vector as diagonal elements.
Determinant	The expression det denotes the determinant.
Operator	Operators are marked with a caret symbol. $\hat{H}$ is an operator.
Real part	The expression Re denotes the real part of an imaginary number.
Imaginary part	The expression Im denotes the imaginary part of an imaginary number.

Chapter 1

Introduction

1.1 Motivation and Achievements 12
1.1.1 Neutralisation Reionisation Mass Spectrometry 13
Description of the experiment 13
Summary of my achievements 15
Other theoretical papers 15
1.1.2 Laser cooling 16
Description of the experiment 16
Summary of my achievements 18
Other theoretical papers 18
1.1.3 Cold Target Recoil Ion Momentum Spectroscopy 18
Description of the experiment 18
Summary of my achievements 19
Other theoretical papers 20
1.2 Outline of the Dissertation 21

1.1 Motivation and Achievements

Every chemistry student learns that spectroscopy in all its variants is a very powerful tool which gives insight into molecular properties and mechanisms such as transitions between stationary states, loss of electrons, distribution of internal energy or atomic rearrangements. But experimentalists can have a hard time to interpret spectra as they are often very complex. The central molecular processes of electronic spectroscopic experiments are vibronic transitions, where a chemical system changes its electronic and vibrational state. Theory can describe these basic steps and so theoretical models play a key role in spectroscopic studies either supporting interpretation or by suggesting new experiments. Still for some

experiments a description that is restricted to the calculation of vibronic spectra is not sufficient.

In this work I take a closer look at three experimental methods:
Neutralization Reionization Mass Spectrometry (NRMS), laser cooling of molecules and Cold Target Ion Momentum Spectroscopy (COLTRIMS). These methods go hand in hand in gas phase ion chemistry research. NRMS is a technique which allows to synthesize and verify the existence of unstable molecular species, and experimentalist can do COLTRIMS on small gas phase molecules to, e.g., learn about their equilibrium structures of the nuclei and about their electronic structure. Laser cooling is an important method for preparation of particle beams injected into the other experimental setups. The methods are therefore closely related and theoretical methods are at least partly transferable.

1.1.1 Neutralisation Reionisation Mass Spectrometry

Description of the experiment

In the beginning of the 1980th NRMS became popular. (See Refs. [2, 3] for a review) It provides a way to synthesize unstable molecular species in the gas phase. Those are often critical intermediates of chemical reactions, but can hardly be stabilized long enough in order to perform experiments in another way, but *in situ* and in the gas phase. [4]

In NRMS a mass-selected ion beam is collided with a neutral gas. Electrons migrate and some of the ions become neutral. An electric field deflects the remaining ions so that there prevails a beam of neutral molecules. Those subsequently collide with e.g. molecular oxygen in a collision chamber and become reionised. After mass selection they hit the detector. If the resulting mass spectrum shows the signal of the reionised starting ion it is considered as a proof that the corresponding neutral species existed within the time frame of the experiment without undergoing fragmentation. [5] Figure 1.1 shows a schematic experimental setup. Figure 1.2 illustrates the vibronic transitions that a molecule undergoes in a $^{-}$NR^{+}MS experiment. The nomenclature $^{-}$NR^{+}MS corresponds to a NRMS experiment where the precursor molecule is an anion and the neutralized species is reionised into its monocationic state. There are other possible charge combinations: $^{+}$NR^{+}MS, $^{+}$NR^{-}MS and $^{-}$NR^{-}MS.

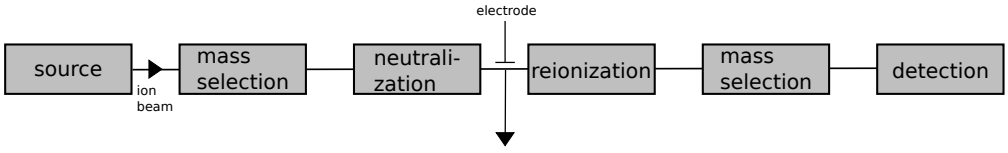

Figure 1.1: Scheme of an experimental setup for NRMS.

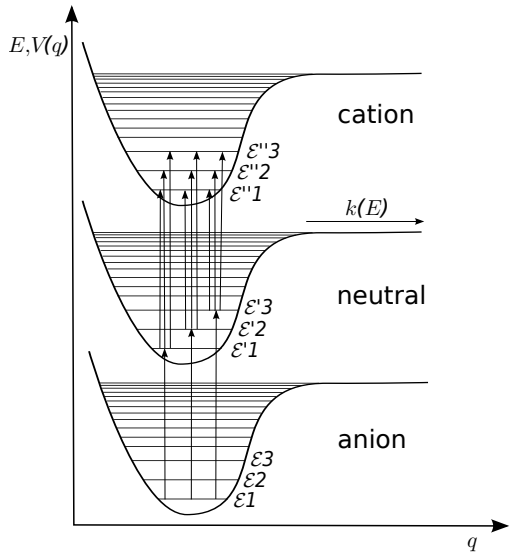

Figure 1.2: Scheme of vibronic transitions of a $^{-}$NR^{+}MS experiment. The molecules initially resides in the lowest vibrational state on the potential energy surface (PES) of the anion. In the first collision with a neutral gas the ions lose electrons and undergo transitions to the PES of the neutral molecule. They do not necessarily end up in the lowest vibrational state, but can also populate vibrationally excited states. Next, the molecules are reionised. In this the cation is generated. Again, the molecules change the PES. Transitions from all populated vibrational states are possible.

One example for a NRMS experiment is the generation of the neutral enol of acetone. [2] Figure 1.3 shows the transformation of the tautomers. Usually the ketone is the more stable tautomer of acetone and when in solution or liquid phase the enol will isomerize to the ketone. However, for the radical cation the enolic form of acetone is preferred. When this species is now neutralized in the gas phase under collision-free conditions, hydrogen backtransfer cannot occur due to a too high barrier for isomerization, such that the molecule stays in its enolic form. Experimentalists can identify the alcohol functionality in the mass spectrum. This proves the stabilisation of the neutral enol.

When a molecule changes its ionic state, e.g. from the neutral molecule to the cation, this can be described as a vibronic transition. A basic quantity is the Franck-Condon factor (FCF) that is approximately proportional to the intensity of a transition between two vibronic states. Details will be given in chapter 2. The FCF is noted as the absolute square of the overlap integral of the corresponding vibrational wave functions.

$$\left|\langle \underline{v}' | \underline{v} \rangle\right|^2 \tag{1.1}$$

where $\underline{v}'$ corresponds to the vector of the vibrational quantum numbers of the final state and $\underline{v}$ to those of the initial state. Especially effective NRMS experi-

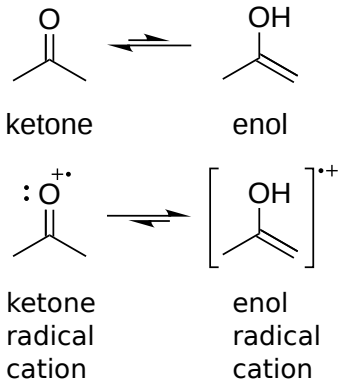

Figure 1.3: Equilibrium between the ketone and the enol form of neutral and cationic acetone.

ments can be performed with molecules that have a highly diagonal Franck-Condon (FC) matrix for the electronic transition. At lower temperatures those molecules preferably undergo the 0–0' transition, which means they change from the lowest vibrational state in the initial electronic state to the lowest vibrational state in the final electronic state. In this case the transition energy is well defined.

Summary of my achievements

I derived equations that allow to calculate vibrational population distributions after neutralization and after reionisation of a molecule. I approximated the vibrations as harmonic vibrations. I extended a time-dependent algorithm and solved severe numerical problems which prevented the calculation of continuous generating functions. I applied the method to a two-dimensional model system for proof of principle and simulated transitions in the NRMS experiment of HNSi which I compared to experimental data. This part of my work resulted in a draft of a manuscript:

S. Marquardt and R. Berger, *Development of a time-dependent generating function ansatz for the description of vibrational population distributions in Neutralization Reionisation Mass Spectrometry*, in preparation.

Other theoretical papers

In the literature one can find different methods for the calculation of FCFs between multi-dimensional harmonic oscillator states: In the year 1964 Sharp and Rosenstock have developed a method using a generating function in which FCFs are calculated for all transitions of polyatomic molecules except for transitions between linear and bend structures. [6] Doktorov et al. have given recursive equations

for the calculation of the overlap integrals in terms of hermite polynomials. [7, 8] Islampour et al. have shown in the year 1999 how to connect the ansätze by Doktorov and Sharp and Rosenstock. [9] They have published explicit and general equations with which one can calculate FC integrals as sums over products of hermite polynomials. Cederbaum et al. have used another ansatz with a one-particle Green's function. [10, 11, 12] Tannor and Heller have described a time-dependent wavepacket method for the calculation of absorption spectra. [1]

I based this work on the developments by Berger, Jankowiak, Huh et al. which are in the tradition of Doktorov's work. [13, 14, 15, 16] Berger and Klessinger have described a modified Kemper-van Dijk-Buck (KDB) energy level counting algorithm [14], which allows assignment of the vibronic transitions to all peaks in the vibronic spectrum. In reference [15] Jankowiak et al. have presented a prescreening method that reduces the calculation time for FC spectra using a generating function ansatz. A time-dependent method has been developed by Huh et al. which included finite temperature, non-Condon effects and anharmonicity. [13, 16]

Published theoretical investigations of the NRMS experiment mainly use quantum chemical methods to provide molecular equilibrium structures, harmonic vibrational frequencies and reaction barriers as for example in references [17, 18, 19]. Grimme has used molecular dynamics trajectories of ensembles of vertically ionized molecules to calculate mass spectra. He has not explicitly calculated vibronic transitions. [20]

Up to now no *ab initio* methods for the calculation of vibrational population distributions after vibronic transitions in a NRMS experiment are described in the literature. Tureček has fitted some preselected functions to experimental data and obtained vibrational population distributions. [21] Wysocki, Kenttämaa and Cooks have approximated the shape of the population distributions of activated ions from ion abundances and appearance energies in a mass spectrometry experiment. [22] Sztáray, Bodi and Baer have developed a model to analyze data from photoelectron photoion coincidence spectroscopy. [23] They have calculated break down curves and time-of-flight distributions under the assumption that the population distributions are unaffected by the ionization.

1.1.2 Laser cooling

Description of the experiment

Laser cooling as an experimental technique is usually used in combination with spectroscopic methods. Laser cooling generates slow particles which leads to highly resolved spectra. The cooled particles show lower Doppler broadening and longer interaction times. [24] High resolution is necessary to investigate weak effects as for example parity violation. [25] Also phenomena as Bose-Einstein condensates

can only be observed for cooled particles. [26]

There are several methods to cool particles with lasers, the most common is the Doppler cooling: A laser with a frequency slightly below an electronic transition energy is used to excite particles which move towards the light source. For these particles the laser frequency might become equal to the transition energy because of the Doppler effect. During the absorption of the photon the particles lose linear momentum in direction of the laser source. When an excited particle relaxes spontaneously it gains linear momentum, but in a random direction. After many excitation and relaxation processes the mean velocity of the particle ensemble is reduced which corresponds to cooling of the particles.

Following the developments for the NRMS experiment I looked at laser cooling of molecules. Figure 1.4 shows a simplified scheme of three vibrational states in the lower electronic state and one vibrational state in the electronically excited state. The aim of the laser cooling experiment is to eventually trap all molecules in a closed cycle of transitions between the electronic states. This would ensure that the molecules can be in principle be cooled for an infinite number of laser cooling cycles. In the idealized system a laser is used to pump vibrationally excited molecules to the higher electronic state. From there they should preferably relax to the vibrational ground state in the lower electronic state from where they can be excited again. This is only efficient, if the FC matrix is highly diagonal. [27] Theoretical methods are therefore useful to predict molecules, which are suitable candidates for laser cooling.

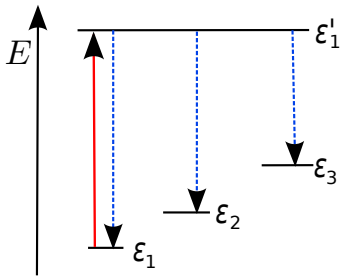

Figure 1.4: Simplified scheme of laser cooling. The system involves three vibrational states in the lower electronic state and one vibrational state in the upper electronic state, marked with the prime symbol. The transition induced by the laser is in red and continuous, relaxations are in blue and dashed. In an ideal system with a highly diagonal FC matrix the molecules will be trapped in a cycle and will only exist in the states ϵ_1 and ϵ'_1.

Laser cooling of molecules is a young experimental technique. The first diatomic molecule was cooled in the year 2010 by Shuman, Barry and DeMille. [28] Other experiments on diatomic molecules followed. [29, 30] Zeppenfeld et al. described an experimental method for cooling of polyatomic molecules with electric field gradients in the year 2012. [31]

Summary of my achievements

The basic principles of transitional laser cooling and NRMS are closely related as both require the calculation of population distributions over vibrational states. For a successful laser cooling experiment it is essential to be able to estimate the population in certain states after thousands of excitation and relaxation cycles. I extended my equations for NRMS to include a specific laser frequency and developed an algorithm that increases the accuracy of the numerical results in comparison to the method I applied to NRMS. I simulated a laser cooling cycle for a one-dimensional harmonic oscillator test system.

Other theoretical papers

In the literature one can find different publications on semiclassical theories that describe sisyphus cooling, another method for translational cooling. [32, 33, 34, 35, 36] Those theories are restricted to laser cooling of atoms or atomic ions. The same is true for the quantum mechanical calculations by Dalibard and Castin as well as Wu et al. [37, 38] Pollack and colleagues have calculated mean vibrational energies and temperatures in excited states. [39, 40, 41] Their work aims on vibrational cooling. The diatomic molecules radium fluoride and ytterbium fluoride have been studied in the context of laser cooling. [25, 42] Isaev, Hoekstra and Berger have calculated FCFs of radium fluoride and identified the molecule as a good candidate for laser cooling. Zhuang et al. have measured the fluorescence spectrum of ytterbium fluoride and have derived the FCFs. Only recently Isaev and Berger have pointed out some polyatomic molecules such as CaNC, CaOH, $CaCH_3$ or $MgCH_3$ as good candidates for laser cooling. [43] Those molecules resemble the diatomic fluorides. Kozyryev et al. [44] have estimated the largest off-diagonal elements of the FC matrices for CaOR and SrOR molecules where R was a methyl, ethyl or isopropyl group.

1.1.3 Cold Target Recoil Ion Momentum Spectroscopy

Description of the experiment

The experimental setup for the COLTRIMS experiment consists of a particle source that provides a molecular beam of cold molecules. The particle beam is crossed with a laser beam, a high energy photon beam or a multiply-charged-ion beam that causes ionisation of single molecules. An electric field guides the ionic products to a detector. At the detector every hit is registered time- and position-sensitive. From this information the linear momenta after ionization can be calculated. A more detailed review on COLTRIMS is given by Dörner et al. [45]

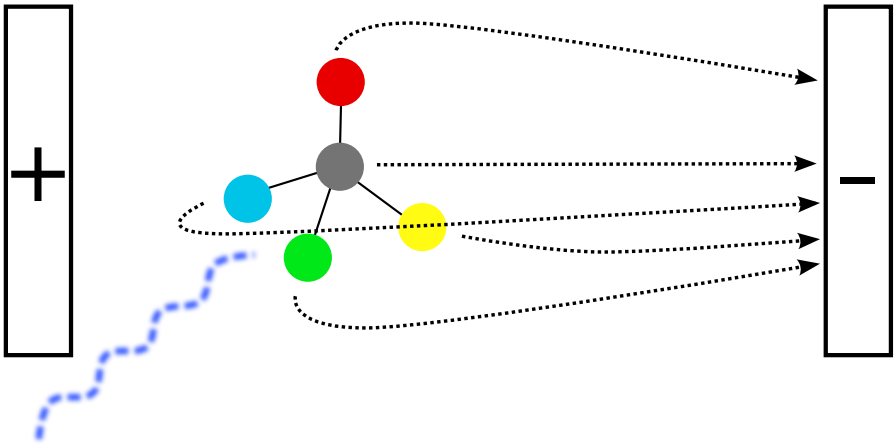

Figure 1.5: Experimental setup of Cold Target Ion Momentum Spectroscopy. The molecule is ionised by the energy beam, for example a laser. The molecule undergoes Coulomb explosion and the charged fragments are accelerated in an electric field towards the detector. The schematic drawing is not to scale.

With an experiment on bromochlorofluoromethane (CHBrClF) Pitzer et al. have shown that COLTRIMS can be used to determine the absolute configuration of single chiral molecules. [46] In the described experiment the molecule is multiply ionized up to the pentacation. It undergoes a Coulomb explosion and the ionic fragments are accelerated towards the detector by the external electric field. From the resulting signal it was possible to reconstruct the initial configuration of momentum vectors of the single molecules.

Polyhalomethanes and their ions are of interest in fundamental research for several aspects: As in the case of CHBrClF they can be chiral, which means that there exist non-identical mirror images of the molecule called enantiomers. Those mirror images cannot be rotated in a way that would bring them in accordance with each other. Enantiomers should show a small energy difference which is due to molecular parity violation. Parity violation is caused by the weak interaction of elementary particles.

During the COLTRIMS experiment a high energy beam, for instance an intense laser beam or a beam of high energy photons, generates multiply charged ions. The high charges cause Coulomb repulsion forces which antagonise the chemical bonding interactions in the molecule. The interplay between the forces is already interesting for small dications. [47, 48]

Summary of my achievements

I investigated different aspects of the COLTRIMS experiment: In the evaluation of experimental data on CHBrClF I contributed a statistical evaluation of the cal-

culated linear momenta considering different isotopic constitutions. The results showed how the selected fragments influence the consistency of the result. Moreover, I searched for an explanation of the bimodal kinetic energy release (KER) distribution for fluorine ions in events with four detected particles. Furthermore, I optimized molecular structures of multiply charged ions and fragment ions of CHBrClF. I investigated their relative stability and their stability towards elimination of atomic or diatomic fragments with quantum chemical calculations. I also addressed the question of metastable achiral structures and their impact on the determination of absolute configuration. I looked at deuterobromofluoroiodomethane (CDBrFI) which was predicted to display a larger parity violation energy splitting than CHBrClF. [49, 50] I calculated fragmentation paths for $CDBrFI^{+\cdot}$ and determined appearance energies for the fragment ions. In order to be able to calculate reaction rates I implemented the Statistical Adiabatic Channel Model (SACM) and applied it to the elimination of atoms and diatomic molecules from the singly charged polyhalomethane. My work on this part resulted in contributions to three manuscripts:

M. Pitzer, G. Kastirke, M. Kunitski et al., *Absolute configuration from different multifragmentation pathways in light-induced Coulomb Explosion Imaging* *ChemPhysChem* **2016**, *17*, 2465.

S. Marquardt, S. Marquardt, M. Pitzer, K. Fehre, H. Schmidt-Böcking, R. Dörner, M. Schöffler, R. Berger, *Theoretical study of gas phase fragmentation of multiply charged bromochlorofluoromethane (CHBrClF)* to be published.

S. Marquardt, A. Schießer, F. Hobi et al., *Ionisation energy of deuterobromofluoroiodomethane (CDBrFI) and appearance energies of its fragment ions* to be published.

Other theoretical papers

During Coulomb explosion the molecules dissociate into multiple fragments. Bondorf et al. describe a statistical model that weights different multifragmentation processes by their entropy. [51] In connection with other statistical methods like the Rice-Ramsperger-Kassel-Marcus (RRKM) method [52, 53, 54] or the SACM [55, 56] and a description of the ionisation process this might allow a complete, statistical description of the experiment up to generation of the fragments. There exist other ansätze which describe multifragmentation. Werner et al. use a quantum chemical multiconfiguration method (MCSCF) and Monte-Carlo generated ionisation. [57] Adachi et al. use Monte-Carlo simulations to describe the

Coulomb explosion of C_3^+ clusters. [58] Psciuk et al. simulate multifragmentations of $C_3H_4{}^{2+}$ with *ab initio* molecular dynamics. [59] The linear momenta are distributed statistically after a method by Bunker and Hase. [60]

Halide derivatives of methane have been studied in various contexts. [61, 62, 63, 64, 65] Some groups looked especially at chiral species. [66, 49, 50, 67]

1.2 Outline of the Dissertation

In the remaining part of this thesis I will turn to three main topics: In chapter 2 I will present the theoretical background of my work in the necessary detail. In chapter 3 I will describe my developments and results. In chapter 4 I will discuss remaining questions. Chapters 3 and 4 will be divided the same way as this introduction in three parts focusing on the contexts of NRMS, laser cooling and COLTRIMS.

Chapter 2

Theoretical Background

2.1 Assumptions 22
2.2 Calculation of Franck-Condon spectra 24
2.2.1 Normal coordinates and Duschinski rotation 24
2.2.2 Coherent states 27
2.2.3 Density of states 31
2.2.4 Franck-Condon approximation 33
2.2.5 Generating function 34
Generating function at 0 K 34
Generating function at finite temperature 36
Time-dependent ansatz 37
2.3 The Statistical Adiabatic Channel Model 39
2.3.1 Detailed Statistical Adiabatic Channel Model 39
2.3.2 Simplified Statistical Adiabatic Channel Model 41

2.1 Assumptions

The vibronic transitions resulting from interactions between molecules and radiation are time-dependent phenomena that are described by the time-dependent Schrödinger equation. However, Fermi's golden rule [68, 69] states that the transition rate from one eigenstate of a quantum system to another eigenstate caused by a perturbation, e.g. a laser beam, is a constant. The rovibronic Schrödinger equation is time-independent and does not account for interactions of the electron spin and the hyperfine structure.

$$\left(-\frac{\hbar^2}{2}\sum_{r=2}^{l}\frac{\nabla_r^2}{m_r}+\frac{\hbar^2}{2M}\sum_{r,s=2}^{l}\nabla_r\nabla_s+\sum_{r<s=1}^{l}\frac{Z_rZ_se^2}{4\pi\epsilon_0 r_{rs}}\right)\psi_{\mathrm{rve}}(\underline{r_e},\underline{r_N})=E_{\mathrm{rve}}\psi_{\mathrm{rve}}(\underline{r_e},\underline{r_N}) \tag{2.1}$$

l is the number of particles, m_r is the mass of particle r, M is the total mass of all particles, $Z_r e$ is charge of particle r, r_{rs} is the interparticle distance between particles r and s, $\underline{r_e}$ are the electron coordinates and $\underline{r_N}$ are the nuclear coordinates. The center of mass motion has been separated out. For more details on how to solve this equation see ref. [70] page 174ff.

I describe the molecules within the adiabatic Born-Oppenheimer approximation which allows separation of the electronic degrees of freedom from the nuclear ones. The resulting error is in the fourth order of the mass ratio of nuclei and electrons $\left(\frac{m_{\mathrm{el}}}{m_{\mathrm{nuc}}}\right)^4$ which is usually negligible. The result is a rovibrational Schrödinger equation. With the Eckart transformation [71] the vibrations and rotations are then approximately separated. I treat the vibrational modes as harmonic oscillators. The resulting vibrational Schrödinger equation for the harmonic oscillator is

$$\left(\frac{1}{2}\hbar \sum_r \omega_r (\hat{p}_r^2 + \hat{q}_r^2)\right) \psi_{\mathrm{vib}} = E_{\mathrm{vib}} \psi_{\mathrm{vib}} \tag{2.2}$$

The momentum and space operators are defined such that we get for the creation and annihilation operators

$$\hat{a}^\dagger = \frac{1}{\sqrt{2}}(\hat{q}_r - \mathrm{i}\hat{p}_r) \tag{2.3}$$

$$\hat{a} = \frac{1}{\sqrt{2}}(\hat{q}_r + \mathrm{i}\hat{p}_r) \tag{2.4}$$

We can therefore also write the Hamiltonian in form of the annihilation and creation operators.

$$\hat{H}_{\mathrm{vib}} = \frac{1}{2} \sum_r \hbar\omega_r (\hat{a_r}^\dagger \hat{a_r} + \hat{a_r} \hat{a_r}^\dagger) \tag{2.5}$$

In the following derivations I use the coherent states description [72] from the framework of quantum electrodynamics. I will describe the states in more detail in section 2.2.2.

I also apply the Franck-Condon approximation whenever calculating integrals of the electronic transition dipole moment. The transition probability is then proportional to the absolute square of the overlap integral between the two vibrational wave functions. Details can be found in section 2.2.4. I do not account for non-Condon effects which could be taken into account by evaluation of the Herzberg-Teller integrals (See e.g. Ref. [13]).

2.2 Calculation of Franck-Condon spectra

I based large parts of my developments on the work by Jankowiak, Huh and Berger on FC spectra. [14, 15, 13, 16] Details and applications of the theory can be found in their publications, but as my developments are strongly connected I will summarize their results and give the basic equations.

2.2.1 Normal coordinates and Duschinski rotation

$\underline{r_{0,1}}, \underline{r_{0,2}}, \underline{r_{0,3}}$ $\underline{r_1}, \underline{r_2}, \underline{r_3}$ $\underline{r'_1}, \underline{r'_2}, \underline{r'_3}$

Figure 2.1: Equilibrium and distorted structures of water. The cartesian coordinates can fully describe all structures.

We usually use normal coordinates for the description of vibrational motion, but in principle this is also possible within a cartesian coordinate system: The coordinates of a molecule in its equilibrium structure are described by their equilibrium coordinates $\underline{r_{0,i}}$. If the molecule is distorted, e.g. by vibrations, the localisation of the atoms is described by displaced coordinates $\underline{r_i}$. Figure 2.1 illustrates this for the water molecule. With the equilibrium and the displaced coordinates one can define cartesian displacement coordinates.

$$\Delta\underline{r_i} = \underline{r_i} - \underline{r_{0,i}} \tag{2.6}$$

With these coordinates it is in principle possible to describe vibrational motions, but normal coordinates have several advantages: For small molecules it can be advantageous that we need a smaller number of coordinates to describe the molecule ($3N-5$ for nonlinear and $3N-6$ for linear molecules instead of $3N$). In the basis of normal modes the Hesse matrix becomes diagonal in the harmonic approximation. The normal modes do not couple. For a symmetric molecule the normal modes will also resemble the molecular symmetry.

When we usually calculate "normal coordinates", e.g. using standard quantum chemistry software, we do not actually get normal coordinates, but the transformation matrix $\boldsymbol{L}$ between mass weighted displacement coordinates and normal

coordinates. $\boldsymbol{L}$ is orthogonal and has the dimension $3N \times 3N$.

$$\begin{pmatrix} \sqrt{m_1}\Delta\underline{r}_1 \\ \sqrt{m_2}\Delta\underline{r}_2 \\ \sqrt{m_3}\Delta\underline{r}_3 \end{pmatrix} = \begin{pmatrix} \sqrt{m_1}\Delta r_{x1} \\ \sqrt{m_1}\Delta r_{y1} \\ \sqrt{m_1}\Delta r_{z1} \\ \sqrt{m_2}\Delta r_{x2} \\ \vdots \\ \sqrt{m_3}\Delta r_{z3} \end{pmatrix} = \boldsymbol{L} \begin{pmatrix} Q_1 \\ Q_2 \\ Q_3 \\ T_x \\ T_y \\ T_z \\ R_x \\ R_y \\ R_z \end{pmatrix} \tag{2.7}$$

T_i are the translational coordinates and R_i are the rotational coordinates. They are eliminated in the following equations and the transformation matrix has the new dimension $3N \times (3N - 6)$.

In the literature different definitions for normal coordinates are used. Therefore, I want to show some basic principles. Coordinates used for example by Jankowiak et al. [15] or in the work of Huh [13] are mass-weighted normal coordinates, while Tannor and Heller [1] use dimensionless normal coordinates for their work on Raman and vibronic spectra.

The mass-weighted normal coordinates are named $\underline{Q}$ and $\underline{Q'}$ for the ground state and excited state PES respectively. The dimensionless coordinates $\underline{y}$ and $\underline{y'}$ are related to $\underline{Q}$ and $\underline{Q'}$ by

$$\underline{y} = \hbar^{-\frac{1}{2}} \boldsymbol{\Omega} \underline{Q} \tag{2.8}$$

$$\underline{y'} = \hbar^{-\frac{1}{2}} \boldsymbol{\Omega'} \underline{Q'} \tag{2.9}$$

where $\boldsymbol{\Omega} = \hbar^{-\frac{1}{2}} \mathrm{diag}(\underline{\epsilon})^{\frac{1}{2}}$ and $\boldsymbol{\Omega'} = \hbar^{-\frac{1}{2}} \mathrm{diag}(\underline{\epsilon'})^{\frac{1}{2}}$. $\underline{\epsilon}$ and $\underline{\epsilon'}$ are the vectors containing the ground state and excited state harmonic oscillator energies ϵ_i and ϵ'_i. $\hbar$ is the reduced Planck constant.

The mass-weighted normal coordinates of the ground and excited state PES are related via the Duschinski transformation [73] as

$$\underline{Q'} = \boldsymbol{S} \underline{Q} + \underline{d} \tag{2.10}$$

where $\boldsymbol{S}$ is called the Duschinski mode mixing matrix and corresponds to a rotation of the normal coordinates. $\underline{d}$ is the displacement vector, that shifts the minimum of the excited harmonic potential to the initial one. Figure 2.2 illustrates the effects of both quantities.

The Duschinski matrix gives the mixing of the different vibrational modes. In the case that $\boldsymbol{S} = \boldsymbol{I}$ the modes are excited independently within a vibronic excitation and the overlap of initial and final state wavefunctions is a product of

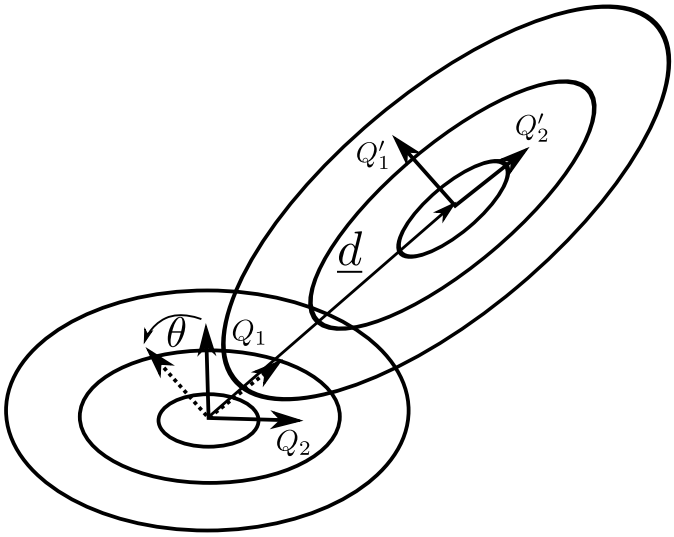

Figure 2.2: Contour line plot of two harmonic oscillator potential energy surfaces. One set of normal coordinates can be obtained from the other by rotation and shifting. The transformation is called Duschinski transformation.

one-dimensional overlaps. In the case that $\boldsymbol{S} \neq \boldsymbol{I}$ modes mix. In general the Duschinski matrix shows a block structure which groups the vibrational normal modes according to their symmetry classes. Only in the subspace of totally symmetric vibrations the displacement can be nonzero. [73]

In order to find an equation for the Duschinski matrix and vector we go back to equation (2.7). The reader may compare the derivations to references [74, 75]. In an Eckart system (see Ref. [71]) the translation and rotation coordinates are 0 and the transformation matrix $\boldsymbol{L}$ becomes a $3N \times (3N-6)$ matrix. We can then rewrite equation (2.7) to describe the cartesian coordinates of nucleus i

$$r_{\alpha i} = r_{0,\alpha i} + m_i^{-\frac{1}{2}} \sum_k L_{\alpha i,k} Q_k, \tag{2.11}$$

where α denotes either x, y or z, or we can find an expression for the kth normal coordinate:

$$Q_k = \sum_{i,\alpha} L_{\alpha i,k} \left[m_i^{\frac{1}{2}} (r_{\alpha i} - r_{0,\alpha i}) \right]. \tag{2.12}$$

The cartesian coordinates of two Eckart systems, e.g. the initial and the final state structure, are related as

$$r'_{\alpha i} = \sum_\beta T_{\alpha\beta} r_{\beta i} \tag{2.13}$$

$\boldsymbol{T}$ is the orthogonal Eckart transformation matrix. We can insert this relation into a dashed version of equation (2.12).

$$Q'_k = \sum_{i,\beta} L'_{\alpha i,k} \left[m_i^{\frac{1}{2}} (T_{\alpha\beta} r_{\beta i} - r'_{0,\alpha i}) \right] \tag{2.14}$$

and then use equation (2.11) to obtain

$$Q'_k = \sum_{i,l,\alpha,\beta} L'_{\alpha i,k} T_{\alpha,\beta} L_{\beta i,l} Q_l + \sum_i L'_{\alpha i,k} m_i^{\frac{1}{2}} (T_{\alpha\beta} r_{0,\beta i} - r'_{0,\alpha i}) \tag{2.15}$$

The same equation in matrix form is

$$\underline{Q'} = \boldsymbol{L'^t M^{\frac{1}{2}} T}(\underline{Q})(\underline{r_0} - \boldsymbol{T}^t(\underline{Q})\underline{r'_0}) + \boldsymbol{L'^t T}(\underline{Q})\boldsymbol{L}\underline{Q} \tag{2.16}$$

where I indicated that the Eckart transformation matrix depends on the normal coordinates. We can then expand $\boldsymbol{T}(\underline{Q})$ in a Taylor series and only use the zeroth order term. If we compare the resulting expression to equation (2.10) we obtain as a linear approximation for the Duschinski matrix and vector

$$\boldsymbol{S} = \boldsymbol{L'^t T_0 L} + \ldots \tag{2.17}$$

$$\underline{d} = \boldsymbol{L'^t M^{\frac{1}{2}} T_0}(\underline{r_0} - \boldsymbol{T_0^t}\underline{r'_0}) \tag{2.18}$$

With the Duschinski matrix and vector one can define

$$\boldsymbol{J} = \boldsymbol{\Omega' S \Omega}^{-1} \tag{2.19}$$

$$\underline{\delta} = \hbar^{-\frac{1}{2}} \boldsymbol{\Omega'} \underline{d} \tag{2.20}$$

and derive the Duschinski relation for dimensionless normal coordinates from equations (2.8) to (2.10) as

$$\begin{aligned} \hbar^{\frac{1}{2}} \boldsymbol{\Omega'}^{-1} \underline{y'} &= \boldsymbol{S} \hbar^{\frac{1}{2}} \boldsymbol{\Omega}^{-1} \underline{y} + \underline{d} \\ \underline{y'} &= \boldsymbol{\Omega' S \Omega}^{-1} \underline{y} + \hbar^{-\frac{1}{2}} \boldsymbol{\Omega'} \underline{d} \\ \underline{y'} &= \boldsymbol{J}(\underline{y} - \Delta) \end{aligned} \tag{2.21}$$

where $\Delta = -\hbar^{-\frac{1}{2}} \boldsymbol{\Omega S}^{-1} \underline{d} = -\boldsymbol{J}^{-1} \underline{\delta}$.

2.2.2 Coherent states

In this section we take a closer look at Gaussian wave packets and coherent states in the harmonic approximation. The vibrational states will be described as coherent

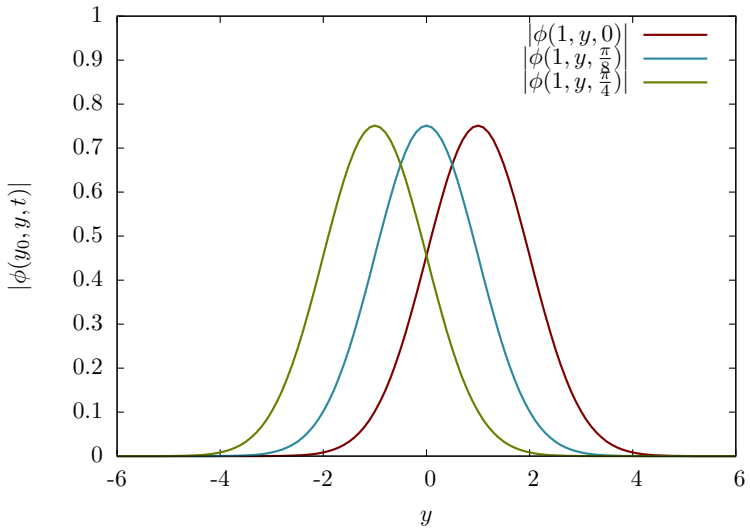

Figure 2.3: One-dimensional coherent state function $\phi(y_0; y, t)$ with parameters: $\omega = 20\ \mathrm{s}^{-1}$, $y_0 = 1$. The wave packet evolves in time without spreading.

states in following sections. Details of the coherent state properties can be found in the publication by Glauber. [72]

A coherent state is a state with minimum uncertainty ($\Delta p \Delta x = \frac{\hbar}{2}$). It corresponds to a wave packet that does not spread while evolving in time. The time-dependent one-dimensional state function is

$$\phi(y_0; y, t) = \sum_{v=0}^{\infty} \frac{1}{\sqrt{v!}} \left(\frac{y_0}{\sqrt{2}}\right)^v \mathrm{e}^{-\frac{1}{4}{y_0}^2} \mathrm{e}^{-\mathrm{i}(v+\frac{1}{2})\omega t} \phi_v(y) \tag{2.22}$$

where

$$\phi_v(y) = \pi^{-\frac{1}{4}} \frac{1}{\sqrt{2^v v!}} \mathrm{e}^{-\frac{1}{2}y^2} H_v(y) \tag{2.23}$$

v is the harmonic oscillator quantum number, ω is the angular harmonic vibrational frequency and y_0 is the shift of the function from the equilibrium geometry at time $t = 0$. y_0 and y are dimensionless,real coordinates which are connected to the cartesian coordinates as $y = \sqrt{\frac{m\omega}{\hbar}} x$. $H_v(y)$ are the Hermite polynomials which can be generated with the recursion:

$$H_v(y) = 2yH_{v-1}(y) - 2(v-1)H_{v-2}(y) \tag{2.24}$$
$$H_0(y) = 1 \tag{2.25}$$
$$H_1(y) = 2y \tag{2.26}$$

The Hermite polynomials can also be defined by the generating function

$$\mathrm{e}^{2ys-s^2} = \sum_{v=0}^{\infty} H_v(y)\frac{s^v}{v!} \tag{2.27}$$

Equation 2.22 can be rewritten using equation 2.23.

$$\phi(y_0;y,t) = \sum_{v=0}^{\infty}\frac{1}{v!}\left(\frac{y_0}{2}\mathrm{e}^{-\mathrm{i}\omega t}\right)^v H_v(y)\mathrm{e}^{-y^2}\pi^{-\frac{1}{4}}\mathrm{e}^{\frac{1}{2}y^2}\mathrm{e}^{-\frac{1}{4}{y_0}^2}\mathrm{e}^{-\frac{1}{2}\mathrm{i}\omega t} \tag{2.28}$$

We can now use equation 2.27 with $s = \frac{y_0}{2}\mathrm{e}^{-\mathrm{i}\omega t}$ and write

$$\begin{aligned}
\phi(y_0;y,t) &= \pi^{-\frac{1}{4}}\mathrm{e}^{-(y-\frac{y_0}{2}\mathrm{e}^{-\mathrm{i}\omega t})^2}\mathrm{e}^{\frac{1}{2}y^2}\mathrm{e}^{-\frac{1}{4}{y_0}^2}\mathrm{e}^{-\frac{1}{2}\mathrm{i}\omega t}\\
&= \pi^{-\frac{1}{4}}\mathrm{e}^{-\frac{1}{2}\mathrm{i}\omega t}\mathrm{e}^{-\frac{1}{2}(y-y_0\mathrm{e}^{-\mathrm{i}\omega t})^2-\frac{1}{4}y_0^2(1-\mathrm{e}^{-2\mathrm{i}\omega t})}\\
&= \pi^{-\frac{1}{4}}\mathrm{e}^{-\frac{1}{2}\mathrm{i}\omega t}\mathrm{e}^{-\frac{1}{2}y^2}\mathrm{e}^{-\frac{1}{4}y_0^2}\mathrm{e}^{yy_0\mathrm{e}^{-\mathrm{i}\omega t}}\mathrm{e}^{-\frac{1}{4}y_0^2\mathrm{e}^{-2\mathrm{i}\omega t}}\\
&= \phi(0;y,t)\mathrm{e}^{-\frac{1}{4}y_0^2}\mathrm{e}^{yy_0\mathrm{e}^{-\mathrm{i}\omega t}}\mathrm{e}^{-\frac{1}{4}y_0^2\mathrm{e}^{-2\mathrm{i}\omega t}} && (2.29)\\
\phi(0;y,t) &= \pi^{-\frac{1}{4}}\mathrm{e}^{-\frac{1}{2}\mathrm{i}\omega t}\mathrm{e}^{-\frac{1}{2}y^2} && (2.30)
\end{aligned}$$

Figure 2.3 shows exemplary plots. In the notation used by Glauber this reads

$$\begin{aligned}
|\alpha;t\rangle &= \sum_{v=0}^{\infty}\frac{\alpha^v}{\sqrt{v!}}\mathrm{e}^{-\frac{1}{2}|\alpha|^2}\mathrm{e}^{-\mathrm{i}(v+\frac{1}{2})\omega t}\,|v\rangle\\
&= |0;t\rangle\,\mathrm{e}^{-\frac{1}{2}|\alpha|^2}\mathrm{e}^{\sqrt{2}y\alpha\mathrm{e}^{-\mathrm{i}\omega t}}\mathrm{e}^{-\frac{1}{2}\alpha^2\mathrm{e}^{-2\mathrm{i}\omega t}} && (2.31)\\
\langle\alpha;t|\alpha;t\rangle &= 1 && (2.32)
\end{aligned}$$

This notation is more general in the sense that α is a complex number. The relation to the first notation is

$$\frac{y_0}{\sqrt{2}} = \mathrm{Re}(\alpha) \tag{2.33}$$

The time-dependence of the coherent states may be incorporated in a factor which is here denoted as $z(t) = \mathrm{e}^{-\mathrm{i}\omega t}$.

$$\begin{aligned}
|\alpha;t\rangle &= \sum_{v=0}^{\infty}\frac{(\alpha\mathrm{e}^{-\mathrm{i}\omega t})^v}{\sqrt{v!}}\mathrm{e}^{-\frac{1}{2}|\mathrm{e}^{-\mathrm{i}\omega t}\alpha|^2}\mathrm{e}^{-\frac{1}{2}\mathrm{i}\omega t}\,|v\rangle && (2.34)\\
&= |z(t)\alpha\rangle\,\mathrm{e}^{-\frac{1}{2}\mathrm{i}\omega t} && (2.35)
\end{aligned}$$

The remaining time-dependent factor corresponds to the zero point energy.

Next we will calculate the overlap integral of two coherent states in order to be able to calculate transition intensities between vibronic states later on. Therefore, a second coherent state β' is defined.

$$\langle\beta';t'| = \langle 0';t'|\,\mathrm{e}^{-\frac{1}{2}|\beta'|^2}\mathrm{e}^{\sqrt{2}y'\beta'^*\mathrm{e}^{\mathrm{i}\omega' t'}}\mathrm{e}^{-\frac{1}{2}(\beta'^*)^2\mathrm{e}^{2\mathrm{i}\omega' t'}} \tag{2.36}$$

In the further sections I will use coherent states in mass-weighted coordinates. So I substitute y by $\hbar^{-\frac{1}{2}}\omega^{\frac{1}{2}}Q$ and renormalise.

$$|\alpha;t\rangle = |0;t\rangle\,\mathrm{e}^{-\frac{1}{2}|\alpha|^2}\mathrm{e}^{\sqrt{2}\sqrt{\frac{\omega}{\hbar}}Q\alpha\mathrm{e}^{-\mathrm{i}\omega t}}\mathrm{e}^{-\frac{1}{2}\alpha^2\mathrm{e}^{-2\mathrm{i}\omega t}} \tag{2.37}$$

$$|0;t\rangle = \left(\frac{\omega}{\hbar}\right)^{\frac{1}{4}}\pi^{-\frac{1}{4}}\mathrm{e}^{-\frac{1}{2}\mathrm{i}\omega t}\mathrm{e}^{-\frac{1}{2}\frac{\omega}{\hbar}Q^2} \tag{2.38}$$

The resulting overlap integral is

$$\begin{aligned}\langle\beta';t'|\alpha;t\rangle = \int_{-\infty}^{\infty} &\hbar^{-\frac{1}{2}}\omega^{\frac{1}{4}}\omega'^{\frac{1}{4}}\pi^{-\frac{1}{2}}\mathrm{e}^{\frac{1}{2}\mathrm{i}(\omega' t'-\omega t)}\mathrm{e}^{-\frac{1}{2\hbar}(\omega' Q'^2+\omega Q^2)}\mathrm{e}^{-\frac{1}{2}(|\alpha|^2+|\beta'|^2)}\\ &\mathrm{e}^{\sqrt{\frac{2}{\hbar}}(\sqrt{\omega'}Q'\beta'^*\mathrm{e}^{\mathrm{i}\omega' t'}+\sqrt{\omega}Q\alpha\mathrm{e}^{-\mathrm{i}\omega t})}\mathrm{e}^{-\frac{1}{2}((\beta'^*)^2\mathrm{e}^{2\mathrm{i}\omega' t'}+\alpha^2\mathrm{e}^{-2\mathrm{i}\omega t})}\,\mathrm{d}Q\end{aligned} \tag{2.39}$$

With the Duschinski relation we can rewrite Q' as $SQ + d$ and then perform the integration step (for more details see appendix A). The result is

$$\langle\beta';t'|\alpha;t\rangle = \frac{1}{\sqrt{S}}\frac{\sqrt{2}\sqrt{J}}{\sqrt{1+J^2}}\mathrm{e}^{-\frac{1}{2}\delta(1-\boldsymbol{P})\delta}\mathrm{e}^{\frac{1}{2}\mathrm{i}(\omega' t'-\omega t)}\mathrm{e}^{-\frac{1}{2}\xi^\dagger\xi}\mathrm{e}^{-\frac{1}{2}\xi^t\boldsymbol{Z}\boldsymbol{W}\boldsymbol{Z}\xi+r^t\boldsymbol{Z}\xi} \tag{2.40}$$

with one-dimensional forms of

$$\boldsymbol{J} = \boldsymbol{\Omega}'\boldsymbol{S}\boldsymbol{\Omega}^{-1} \tag{2.41}$$

$$\underline{\xi} = \begin{pmatrix}\underline{\alpha}\\ \underline{\beta'^*}\end{pmatrix} \tag{2.42}$$

$$\boldsymbol{W} = \begin{pmatrix}\boldsymbol{I}-2\boldsymbol{Q} & -2\boldsymbol{R}\\ -2\boldsymbol{R}^t & \boldsymbol{I}-2\boldsymbol{P}\end{pmatrix} \tag{2.43}$$

$$\underline{r} = \sqrt{2}\begin{pmatrix}-\boldsymbol{R}\underline{\delta}\\ (\boldsymbol{I}-\boldsymbol{P})\underline{\delta}\end{pmatrix} \tag{2.44}$$

$$\boldsymbol{Q} = (\boldsymbol{I}+\boldsymbol{J}^t\boldsymbol{J})^{-1} \tag{2.45}$$

$$\boldsymbol{P} = \boldsymbol{J}\boldsymbol{Q}\boldsymbol{J}^t \tag{2.46}$$

$$\boldsymbol{R} = \boldsymbol{Q}\boldsymbol{J}^t \tag{2.47}$$

$$\boldsymbol{Z} = \mathrm{diag}(z_1, z_2, \ldots, z'_1, z'_2, \ldots) \tag{2.48}$$

$$z_k = \mathrm{e}^{-\mathrm{i}\omega_k t} \tag{2.49}$$

$$z'_k = \mathrm{e}^{\mathrm{i}\omega'_k t'} \tag{2.50}$$

The first part of equation (2.40) ($\frac{1}{\sqrt{S}}\frac{\sqrt{2}\sqrt{J}}{\sqrt{1+J^2}}\mathrm{e}^{-\frac{1}{2}\delta(1-\boldsymbol{P})\delta}\mathrm{e}^{\frac{1}{2}\mathrm{i}(\omega' t'-\omega t)}$) can be identified with the 0'-0 integral, which can be additionally normalized by multiplication with $|\det(\boldsymbol{S})|^{1/2}$.

$$\langle\beta';t'|\alpha;t\rangle = \langle 0';t'|0;t\rangle\,\mathrm{e}^{-\frac{1}{2}\xi^\dagger\xi}\mathrm{e}^{-\frac{1}{2}\xi^t\boldsymbol{Z}\boldsymbol{W}\boldsymbol{Z}\xi+r^t\boldsymbol{Z}\xi} \tag{2.51}$$

$$\langle 0';t'|0;t\rangle = \frac{\sqrt{2}\sqrt{J}}{\sqrt{1+J^2}}\mathrm{e}^{-\frac{1}{2}\delta(1-\boldsymbol{P})\delta}\mathrm{e}^{\frac{1}{2}\mathrm{i}(\omega' t'-\omega t)} \tag{2.52}$$

This corresponds exactly to the equation given in reference [15]. An N-dimensional version of the overlap integral can be obtained with N-dimensional coherent states.

$$|\underline{\alpha};t\rangle = |\underline{0};t\rangle\,\mathrm{e}^{-\frac{1}{2}\underline{\alpha}^\dagger\underline{\alpha}}\prod_{k=1}^{N}\mathrm{e}^{\sqrt{2}y_k\alpha_k\mathrm{e}^{-\mathrm{i}\omega_k t}-\frac{1}{2}\alpha_k^2\mathrm{e}^{-2\mathrm{i}\omega_k t}} \tag{2.53}$$

$$\langle\underline{\beta'};t'|\underline{\alpha};t\rangle = \frac{2^{\frac{N}{2}}\sqrt{|\det(\boldsymbol{R})|}}{\sqrt{|\det(\boldsymbol{S})|}}\mathrm{e}^{-\frac{1}{2}\underline{\delta}(1-\boldsymbol{P})\underline{\delta}}\mathrm{e}^{\frac{1}{2}\mathrm{i}(\omega' t'-\omega t)}\mathrm{e}^{-\frac{1}{2}\underline{\xi}^\dagger\underline{\xi}}\mathrm{e}^{-\frac{1}{2}\underline{\xi}^t\boldsymbol{Z}\boldsymbol{W}\boldsymbol{Z}\underline{\xi}+\underline{r}^t\boldsymbol{Z}\underline{\xi}} \tag{2.54}$$

2.2.3 Density of states

The vibronic spectra or population distributions are not quantities of a single molecule, but describe a statistical ensemble of molecules. Therefore, we need some properties that describe the state of such an ensemble. Here, I introduce the concepts of the density of states (DOS) and the Boltzmann distribution function.

The DOS, denoted as $\rho(E)$ gives the number of states per unit of energy. Figure 2.4 shows an example for a coarse-grained determination of the DOS. It is a function of the energy that, when integrated over an energy range, gives the total number of states in that range. The resulting quantity is also called sum of states if the lower border of the interval is equal to 0.

$$W(E) = \int_0^E \rho(\epsilon)\,\mathrm{d}\epsilon \tag{2.55}$$

The sum of states is an increasing function. For an harmonic oscillator with angular frequency ω it looks like a staircase and is a superposition of Heaviside step functions $\theta(E - i\hbar\omega)$.

$$W(E) = \sum_i \theta(E - i\hbar\omega) \tag{2.56}$$

The DOS is the derivative with respect to the energy. The derivative of the Heaviside step function is the Dirac delta function.

$$\rho(E) = \sum_i \delta(E - i\hbar\omega) \tag{2.57}$$

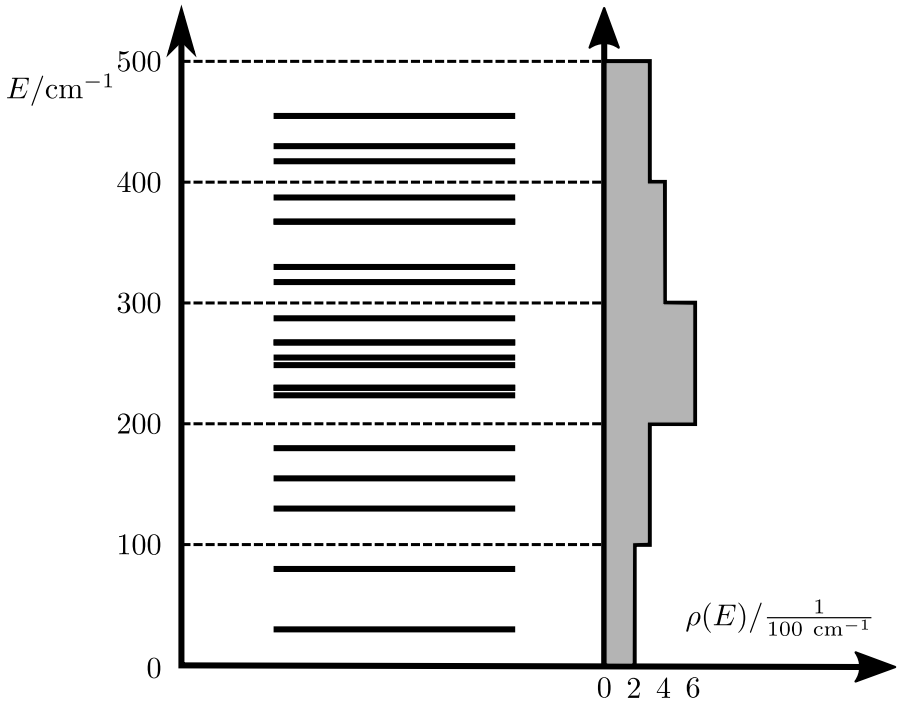

Figure 2.4: Example for the construction of the DOS of energy levels between $0\,\mathrm{cm}^{-1}$ and $500\,\mathrm{cm}^{-1}$.

Both, the DOS and the sum of states, are used to calculate reaction rates $k(E)$ of unimolecular reactions. In transition state theory for example the sum of states at the transition state (indicated by †) is divided by the DOS of the reactant.

$$k(E) = \frac{W^{\dagger}(E)}{h\rho(E)} \tag{2.58}$$

The DOS itself can be calculated for a system of harmonic oscillators by direct counting. I used the Beyer-Swinehart algorithm [76] which needs the number of harmonic oscillators n, the vibrational angular frequencies ω_i, the maximum energy E_{max} and the energy graining ΔE as input. I want to illustrate the algorithm in pseudo code form:

Beyer-Swinehart algorithm:

Initialize $\rho(0) = 1$, $\rho(i) = 0$ for $i > 0$.

For $j = 1$ to n

For $i = \frac{\hbar\omega}{\Delta E}$ to $E_{\max}/\Delta E$

$\rho(i) = \rho(i) + \rho(i - \hbar\omega_j)$

Increase $i = i + 1$.

Increase $j = j + 1$.

End.

The DOS can also be calculated with classical approximations. For more details on those I refer to appendix E. The DOS gives information about the distribution of the states of a system, but those may either be occupied or unoccupied. If we want to know the number of molecules with an inner energy in a specific interval, we need to apply a distribution function such as the Boltzmann distribution function. The resulting Boltzmann population is

$$P_{\text{Boltzmann}}(E) = \frac{g(E)\exp\left(-\frac{E}{k_B T}\right)}{Q} \tag{2.59}$$

$$Q = \int_0^\infty \rho(E)\exp\left(-\frac{E}{k_B T}\right)\,\mathrm{d}E \tag{2.60}$$

$$g(E) = \rho(E)\,\mathrm{d}E \tag{2.61}$$

Q is the canonical partition function and $g(E)$ is the degeneracy.

2.2.4 Franck-Condon approximation

Observables in quantum mechanics are calculated as matrix elements of specific operators. For the description of electric dipole transitions we use the electronic transition dipole moment operator $\hat{\mu}_{\text{elec}}$. A vibronic transition is described with the vibronic matrix element

$$\left|\langle \underline{v'}|\hat{\mu}_{\text{elec}}|\underline{v}\rangle\right|^2 \tag{2.62}$$

$\underline{v'}$ and $\underline{v}$ are the vibrational wave functions of the final and initial electronic states. The electronic transition dipole moment can be expanded in a Taylor expansion

with respect to the normal coordinates.

$$\hat{\mu}_{\text{elec}}(\underline{Q}) = \mu_0 + \sum_{i=1}^{N} \mu_i' \hat{Q}_i + \dots \tag{2.63}$$

In the FC approximation this expression is truncated after the constant term μ_0 and we can rewrite equation (2.62).

$$|\langle \underline{v'}|\hat{\mu}_{\text{elec}}|\underline{v}\rangle|^2 = |\mu_0|^2 \, |\langle \underline{v'}|\underline{v}\rangle|^2 \tag{2.64}$$

The square of the overlap integral of the vibrational wave functions is called the FCF and is proportional to the intensity of the vibronic transition.

2.2.5 Generating function

In this part I summarize results from Jankowiak et al. [15] about the calculation of vibronic spectra at 0 K. The method will be extended to describe transitions at finite temperature and reformulated in a time-dependent ansatz according to the derivations by Huh et al. [13, 16]

Generating function at 0 K

The FC weighted spectral density function is formally given by

$$\rho_{\text{FC}}(\hbar\omega) = \sum_{\underline{v},\underline{v'}=\underline{0}}^{\infty} |\langle \underline{v'}|\underline{v}\rangle|^2 \, \delta(\hbar(\omega - \overline{\omega})) \tag{2.65}$$

where

$$|\underline{v}\rangle = |v_1 v_2 ... v_N\rangle \tag{2.66}$$

is the occupation number vector for the vibrational levels of the initial state. At 0 K we can set $\underline{v} = \underline{0}$ because only the lowest vibrational state is populated. With this or other restrictions of the population distribution of the initial state we also avoid infinities in the summation. $\underline{v'}$ refers to the final state. The transition angular frequency is defined as

$$\overline{\omega} = \omega_0 + \omega_{\underline{v'},\underline{v}} = \omega_0 - \omega_{\underline{v}} + \omega_{\underline{v'}} \tag{2.67}$$

where ω_0 corresponds to the $\underline{0}$-$\underline{0'}$ transition angular frequency. $\omega_{\underline{v}}$ and $\omega_{\underline{v'}}$ are the angular frequencies at the vibrational states $\underline{v}$ and $\underline{v'}$ with respect to the corresponding potential minimum.

We define a generating function

$$G(\boldsymbol{Z}) = \pi^{-2N} \left|\langle \underline{0}'|\underline{0}\rangle\right|^{-2} \int \mathrm{d}^2\underline{\alpha}\, \mathrm{d}^2\underline{\gamma}' \left\langle \boldsymbol{z}'^{*}\underline{\gamma}'|\boldsymbol{z}\underline{\alpha}\right\rangle \left\langle \boldsymbol{z}'\underline{\gamma}'|\boldsymbol{z}^{*}\underline{\alpha}\right\rangle^{*} \tag{2.68}$$

with parameters

$$\boldsymbol{Z} = \begin{pmatrix} \boldsymbol{z} & \boldsymbol{0} \\ \boldsymbol{0} & \boldsymbol{z}' \end{pmatrix} \tag{2.69}$$

$$\boldsymbol{z} = \mathrm{diag}(z_1, z_2, \ldots, z_N) \tag{2.70}$$

$$\boldsymbol{z}' = \mathrm{diag}(z'_1, z'_2, \ldots, z'_N) \tag{2.71}$$

$\underline{\alpha}$ and $\underline{\gamma}'$ are coherent states. The z_i are to be defined. Overlap integrals of the coherent states can be written (see references [72, 77][1]) as

$$\left\langle \underline{\gamma}'|\underline{\alpha}\right\rangle = \exp\left(-\frac{1}{2}\underline{\alpha}^{\dagger}\underline{\alpha} - \frac{1}{2}\underline{\gamma}^{\dagger}\underline{\gamma}\right) \sum_{\underline{v},\underline{v}'=\underline{0}}^{\infty} \langle \underline{v}'|\underline{v}\rangle \left[\prod_{k=1}^{N} \frac{(\gamma'^{*}_k)^{v'_k}\alpha_k^{v_k}}{\sqrt{(v'_k)!v_k!}}\right] \tag{2.72}$$

$$\left\langle \underline{\gamma}'|\underline{\alpha}\right\rangle = \langle \underline{0}'|\underline{0}\rangle \exp\left(-\frac{1}{2}\underline{\xi}^{\dagger}\underline{\xi}\right) \exp\left(-\frac{1}{2}\underline{\xi}^{t}\boldsymbol{W}\underline{\xi} + \underline{r}^{t}\underline{\xi}\right) \tag{2.73}$$

Equation (2.72) is referred to as the *occupancy representation*, whereas (2.73) is the *spatial representation*. $\underline{\xi}$ is the vector

$$\underline{\xi} = \begin{pmatrix} \underline{\alpha} \\ \underline{\gamma}'^{*} \end{pmatrix}, \tag{2.74}$$

$\boldsymbol{W}$ and $\underline{r}$ are defined as in section 2.2.2. Both expressions for the overlap integrals are equivalent and so we use both to obtain two equations for the generating function (see appendices B and C for details):

$$G(\boldsymbol{Z}) = \sum_{\underline{v},\underline{v}'=\underline{0}}^{\infty} q(\underline{v}';\underline{v}) \prod_{k=1}^{N} \left[(z'_k)^{2v'_k} z_k^{2v_k}\right] \tag{2.75}$$

$$q(\underline{v}';\underline{v}) = \frac{\left|\langle \underline{v}'|\underline{v}\rangle\right|^2}{\left|\langle \underline{0}'|\underline{0}\rangle\right|^2} \tag{2.76}$$

$$G(\boldsymbol{Z}) = \det(\boldsymbol{I} - \boldsymbol{Z}\boldsymbol{W}\boldsymbol{Z})^{-\frac{1}{2}} \det(\boldsymbol{I} + \boldsymbol{Z}\boldsymbol{W}\boldsymbol{Z})^{-\frac{1}{2}} \exp(\underline{r}^{t}\boldsymbol{Z}(\boldsymbol{I} + \boldsymbol{Z}\boldsymbol{W}\boldsymbol{Z})^{-1}\boldsymbol{Z}\underline{r}) \tag{2.77}$$

Equation (2.77) allows a straightforward and numerically feasible calculation of the generating function. Equation (2.75) leads to:

$$\left|\langle \underline{0}'|\underline{0}\rangle\right|^2 G(\boldsymbol{Z}) = \sum_{\underline{v},\underline{v}'=\underline{0}}^{\infty} \left|\langle \underline{v}'|\underline{v}\rangle\right|^2 \prod_{k=1}^{N} \left[(z'_k)^{2v'_k} z_k^{2v_k}\right] \tag{2.78}$$

[1] In reference [77] equation (3.2) should have $\langle \underline{0}'|\underline{0}\rangle$ instead of $\langle \underline{0}|\underline{0}\rangle$.

Comparing equation (2.78) to (2.65) shows that they are identical if $z_k = 1$ and $z'_k = 1$. The spectral density function can then be written in terms of the generating function.

$$\rho_{\mathrm{FC}}(\hbar\omega) = \left|\langle \underline{0}'|\underline{0}\rangle\right|^2 G(\boldsymbol{I})\delta(\hbar(\omega - \overline{\omega})) \tag{2.79}$$

Generating function at finite temperature

The generating function may be modified in order to include a Boltzmann distribution of the vibrational population in the initial state. This allows for the calculation of vibronic spectra at other temperatures than 0 K. The subscript FCW indicates that we use the FC approximation and weight the generating function with the Boltzmann distribution.

$$\rho_{\mathrm{FCW}}(\hbar\omega; T) = \mathcal{N} \sum_{\underline{v},\underline{v}'=\underline{0}}^{\infty} \left|\langle \underline{v}'|\underline{v}\rangle\right|^2 \delta(\hbar(\omega - \overline{\omega}))\mathrm{e}^{-(\underline{v}'^t \boldsymbol{B}'\underline{\epsilon}' + \underline{v}^t \boldsymbol{B}\underline{\epsilon})} \tag{2.80}$$

where $\boldsymbol{B}' = \mathrm{diag}(\beta'_1, \beta'_2, \ldots, \beta'_N)$ and $\boldsymbol{B} = \mathrm{diag}(\beta_1, \beta_2, \ldots, \beta_N)$ with $\beta_k = \frac{1}{k_B T_k}$. Therefore, a thermal integral kernel is included into the generating function:

$$G(\boldsymbol{Z}; \boldsymbol{\Lambda}) = \pi^{-2N} \left|\langle \underline{0}'|\underline{0}\rangle\right|^{-2} \int d^2\underline{\alpha}\, d^2\underline{\gamma}' K(\boldsymbol{\Lambda}, \underline{\xi}) \left\langle \boldsymbol{z}'^* \underline{\gamma}'|\boldsymbol{z}\underline{\alpha}\right\rangle \left\langle \boldsymbol{z}'\underline{\gamma}'|\boldsymbol{z}^*\underline{\alpha}\right\rangle^* \tag{2.81}$$

$$K(\boldsymbol{\Lambda}, \underline{\xi}) = \mathcal{N}\det(\boldsymbol{I} + \boldsymbol{\Lambda}) \exp\left(-\underline{\xi}^\dagger \boldsymbol{\Lambda}\underline{\xi}\right) \tag{2.82}$$

$$\boldsymbol{\Lambda} = \mathrm{diag}(\lambda_1, \lambda_2 \ldots \lambda'_1, \lambda'_2 \ldots) \tag{2.83}$$

The relation between β_k and λ_k is $(1 + \lambda_k)^{-1} = \exp(-\beta_k \epsilon_k)$. $\mathcal{N}$ is a normalization constant. It is given as the reciprocal vibrational partition function.

$$\mathcal{N} = \prod_{k=1}^{N} (1 - \exp(-v'_k \beta'_k \epsilon'_k))(1 - \exp(-v_k \beta_k \epsilon_k)) \tag{2.84}$$

Analogue to equations (2.72) and (2.73) one obtains now for the generating function (see appendix D for details):

$$G(\boldsymbol{Z}; \boldsymbol{\Lambda}) = \sum_{\underline{v},\underline{v}'=\underline{0}}^{\infty} q(\underline{v}'; \underline{v}) \prod_{k=1}^{N} \left[(z'_k)^{2v'_k} z_k^{2v_k}\right] \mathrm{e}^{-(\underline{v}'^t \boldsymbol{B}'\underline{\epsilon}' + \underline{v}^t \boldsymbol{B}\underline{\epsilon})} \tag{2.85}$$

$$G(\boldsymbol{Z}; \boldsymbol{\Lambda}) = \det(\boldsymbol{I} - \boldsymbol{Z}\boldsymbol{W}_T\boldsymbol{Z})^{-\frac{1}{2}} \det(\boldsymbol{I} + \boldsymbol{Z}\boldsymbol{W}_T\boldsymbol{Z})^{-\frac{1}{2}} \exp(\underline{r}_T{}^t \boldsymbol{Z}(\boldsymbol{I} + \boldsymbol{Z}\boldsymbol{W}_T\boldsymbol{Z})^{-1}\boldsymbol{Z}\underline{r}_T) \tag{2.86}$$

$$\boldsymbol{W}_T = (\boldsymbol{I} + \boldsymbol{\Lambda})^{-\frac{1}{2}} \boldsymbol{W} (\boldsymbol{I} + \boldsymbol{\Lambda})^{-\frac{1}{2}} \tag{2.87}$$

$$\underline{r}_T = (\boldsymbol{I} + \boldsymbol{\Lambda})^{-\frac{1}{2}} \underline{r} \tag{2.88}$$

For z_k and z'_k equal 1, the expression for the generating function can be inserted into (2.80).

$$\rho_{\mathrm{FCW}}(\hbar\omega;T) = \mathcal{N}\left|\langle\underline{0}'|\underline{0}\rangle\right|^2 G(\boldsymbol{I};\boldsymbol{\Lambda})\delta(\hbar(\omega-\overline{\omega})) \tag{2.89}$$

Time-dependent ansatz

With a time-dependent method the vibronic spectrum can often be calculated much faster than with a time-independent algorithm such as the KDB algorithm [14]. In the time-dependent picture it becomes feasible to calculate vibronic spectra for large molecules, but at the expense of loosing information about single peaks. Information about single peaks in the analysis of vibrational population distributions is in principle not necessary, so I chose this ansatz for my later derivations.

We change from the time-independent picture to the time-dependent picture via a Fourier transformation. The Dirac delta distribution can be written as the Fourier transform of a complex exponential function.

$$\delta(\hbar(\omega-\overline{\omega})) = \frac{1}{\hbar}\delta(\omega-\overline{\omega}) = \frac{1}{\hbar}\int\limits_{-\infty}^{\infty}\mathrm{d}t\,\mathrm{e}^{\mathrm{i}(\omega-\overline{\omega})t} \tag{2.90}$$

We introduce this into equation (2.65)

$$\rho_{\mathrm{FC}}(\hbar\omega) = \mathcal{N}\frac{1}{\hbar}\int\limits_{-\infty}^{\infty}\mathrm{d}t\sum_{\underline{v},\underline{v}'=\underline{0}}^{\infty}\left|\langle\underline{v}'|\underline{v}\rangle\right|^2\mathrm{e}^{\mathrm{i}(\omega-\overline{\omega})t} \tag{2.91}$$

The exponential expression can be rewritten

$$\begin{aligned}\mathrm{e}^{\mathrm{i}(\omega-\overline{\omega})t} &= \mathrm{e}^{\mathrm{i}(\omega-(\omega_0+\omega_{\underline{v}',\underline{v}}))t}\\ &= \mathrm{e}^{\mathrm{i}(\omega-\omega_0)t}\mathrm{e}^{-\mathrm{i}\omega_{\underline{v}'}t}\mathrm{e}^{\mathrm{i}\omega_{\underline{v}}t}\\ &= \mathrm{e}^{\mathrm{i}(\omega-\omega_0)t}\mathrm{e}^{-\mathrm{i}\frac{\underline{\epsilon}'\cdot\underline{v}'}{\hbar}t}\mathrm{e}^{\mathrm{i}\frac{\underline{\epsilon}\cdot\underline{v}}{\hbar}t}\end{aligned} \tag{2.92}$$

Equation (2.91) then gives

$$\rho_{\mathrm{FC}}(\hbar\omega) = \mathcal{N}\frac{1}{\hbar}\int\limits_{-\infty}^{\infty}\mathrm{d}t\sum_{\underline{v},\underline{v}'=\underline{0}}^{\infty}\left|\langle\underline{v}'|\underline{v}\rangle\right|^2\exp\left(-\mathrm{i}\frac{\underline{\epsilon}'\cdot\underline{v}'}{\hbar}t\right)\exp\left(\mathrm{i}\frac{\underline{\epsilon}\cdot\underline{v}}{\hbar}t\right)\mathrm{e}^{\mathrm{i}(\omega-\omega_0)t} \tag{2.93}$$

This introduces additional factors into the expressions for the generating function

(Compare to equation (2.75).):

$$G(\tilde{\boldsymbol{Z}},t) = \sum_{\underline{v},\underline{v}'=\underline{0}}^{\infty} q(\underline{v}';\underline{v}) \prod_{k=1}^{N} \left[(\tilde{z}_k')^{2v_k'} \exp\left(-\mathrm{i}\frac{\epsilon_k' v_k'}{\hbar} t\right) \tilde{z}_k^{2v_k} \exp\left(\mathrm{i}\frac{\epsilon_k v_k}{\hbar} t\right) \right]$$
$$= \sum_{\underline{v},\underline{v}'=\underline{0}}^{\infty} q(\underline{v}';\underline{v}) \prod_{k=1}^{N} \left[\left(\tilde{z}_k' \exp\left(-\mathrm{i}\frac{\epsilon_k'}{2\hbar} t\right)\right)^{2v_k'} \left(\tilde{z}_k \exp\left(\mathrm{i}\frac{\epsilon_k}{2\hbar} t\right)\right)^{2v_k} \right] \tag{2.94}$$

Equation (2.75) is regained for

$$z_k(t) = \exp\left(\mathrm{i}\frac{\epsilon_k}{2\hbar} t\right) \tilde{z}_k \tag{2.95}$$

$$z_k'(t) = \exp\left(-\mathrm{i}\frac{\epsilon_k'}{2\hbar} t\right) \tilde{z}_k' \tag{2.96}$$

We insert into (2.91) with $\tilde{z}_k = 1$ and $\tilde{z}_k' = 1$

$$\rho_{\mathrm{FC}}(\hbar\omega) = \mathcal{N}\frac{1}{\hbar} \left|\langle \underline{0}' | \underline{0} \rangle\right|^2 \int_{-\infty}^{\infty} \mathrm{d}t\, G(\boldsymbol{Z}(t)) \mathrm{e}^{\mathrm{i}(\omega-\omega_0)t} \tag{2.97}$$

Including the thermal dependence this is

$$\rho_{\mathrm{FCW}}(\hbar\omega;T) = \mathcal{N}\frac{1}{\hbar} \left|\langle \underline{0}' | \underline{0} \rangle\right|^2 \int_{-\infty}^{\infty} \mathrm{d}t\, G(\boldsymbol{Z}(t);\boldsymbol{\Lambda}) \mathrm{e}^{\mathrm{i}(\omega-\omega_0)t} \tag{2.98}$$

The $\underline{0}$-$\underline{0}'$-transition integral can be moved out of the integral since the time-dependence is lost when forming the square of the absolute value.

The result can be compared to the ansatz given by Tannor and Heller. [1] They derive a time-dependent expression for the absorption cross section that should be proportional to the spectral density function for a temperature of 0 K.

$$\sigma_A = \sum_n |\, \langle \chi_n | \phi_i \rangle \,|^2 \delta(\omega' - \omega_n)$$
$$= \int_{-\infty}^{\infty} \langle \phi_i | \phi_i(t) \rangle \exp(\mathrm{i}\omega' t)\, \mathrm{d}t$$
$$= \int_{-\infty}^{\infty} I_0 \exp(\mathrm{i}\omega' t)\, \mathrm{d}t \tag{2.99}$$

$|\chi_n\rangle$ is a vibronic state. $|\phi_i\rangle$ is defined as $\mu\,|\chi_n\rangle$ where μ is the transition dipole moment. $|\phi_i(t)\rangle$ is a wave packet and I_0 is its autocorrelation function. A comparison of symbols used by Tannor and Heller and their equivalents in this work is given in table 2.1. By actual comparison of the expressions for the above given generating function multiplied with the square of the $0 - 0'$-transition integral and the expression for I_0 for the one-dimensional case, one is left with a factor of $\exp(\frac{1}{2}\mathrm{i}\omega' t)$ that needs to be multiplied on I_0 to achieve equality. Otherwise the spectrum calculated with the method of Tannor and Heller is shifted by half the wavelength of the final state oscillator to higher wavelengths.

Table 2.1: Symbols as used by Tannor and Heller in [1] and in this work.

Reference [1]	This work
q	y
q_{ex}	y'
ω_g	ω
ω_{ex}	$\omega' + \omega_0$
$\boldsymbol{J}$	$\boldsymbol{J}^{-1}$
Δ	$\Delta = -\hbar^{-\frac{1}{2}}\boldsymbol{\Omega}\boldsymbol{S}^{-1}\underline{d}$
$\lvert\chi_i\rangle$	$\lvert\underline{v}\rangle$
$\lvert\chi_n\rangle$	$\lvert\underline{v'}\rangle$

2.3 The Statistical Adiabatic Channel Model

A comprehensive description of the NRMS and COLTRIMS includes fragmentation of molecules in addition to the vibronic transitions. In order to describe such fragmentations I implemented and applied the SACM which has been described in its detailed version by Quack and Troe in the year 1974. [55] For my applications I found the Simplified SACM more practical which has been described by Troe in the year 1983. [56] I will give an overview of both models in the following sections.

2.3.1 Detailed Statistical Adiabatic Channel Model

The SACM is used to calculate reaction rate coefficients. It is built on three assumptions:

1. Ergodicity: The coupling between the vibrational degrees of freedom is strong enough, so that the excitation energy is rapidly randomized among them.

2. Adiabatic potentials: Reactant and product states are connected via adiabatic potential curves. The reaction coordinate is not coupled to other coordinates. Potential curves do not cross.

3. Reactive States: Only those states are reactive that hold enough energy to overcome the energy barrier. There is no tunneling effect.

The reactive states are determined with (ro)vibrationally adiabatic potential curves. Those are found by holding the reaction coordinate q fixed and solving the vibrational Schrödinger equation for the other coordinates $\underline{u}$.

$$\left(\sum_i -\frac{\hbar^2}{2m}\frac{\partial^2}{\partial u_i^2} + V'(\underline{u};q)\right)\Psi_a(\underline{u};q) = E_a(q)\Psi_a(\underline{u};q) \tag{2.100}$$

$\sum_i -\frac{\hbar^2}{2m}\frac{\partial^2}{\partial u_i^2}$ is the kinetic energy operator for the free degrees of freedom. $V'(\underline{u};q)$ is the potential energy operator for a fixed coordinate q. Further terms, e.g. the spin-orbit coupling, are not considered. The resulting eigenvalues $E_a(q)$ are added to the potential $V(q)$ in the direction of the reaction coordinate. A problem with the assumption of adiabatic curves is that the error for the separation of motions is in the fourth order of the mass ratio of the involved particles. In the case that these particles are nuclei and electrons as in the Born-Oppenheimer approximation $\left(\frac{m_{\mathrm{el}}}{m_{\mathrm{nuc}}}\right)^4$ is a small number. In the SACM case motions of nuclei are separated and the error might not be negligible. Figure 2.5 shows potential curves. Only the channels for which the barrier is below $E_{\max}$ are called reactive states at energy $E_{\max}$.

However, the calculation of the required points on the adiabatic potential curves for all product states is very tedious. We can simplify this with two more assumptions: We assume that there is a one-to-one correspondence between reactant and product states which can be adiabatically correlated. For some modes this is reasonable as they are unchanged between reactant and products. They are the conserved modes. Other modes change from vibrations in the reactant to rotations in the product. They are called transitional modes. Secondly, we assume that the adiabatic potential curves can be defined as

$$V_a(q) = V(q) + E_n(q)\mathrm{e}^{-\alpha(q-q_e)} + E_p(q)\left(1-\mathrm{e}^{-\alpha(q-q_e)}\right) + V_{\mathrm{cent}}(q) \tag{2.101}$$

The potential $V(q)$ can be, e.g., a Morse oscillator potential or an ion-dipole potential. The exponential functions are switching functions. They switch between the reactant states with eigenvalues E_n of the (ro)vibrational Schrödinger equation and the product states with eigenvalues E_p while following the reaction coordinate.

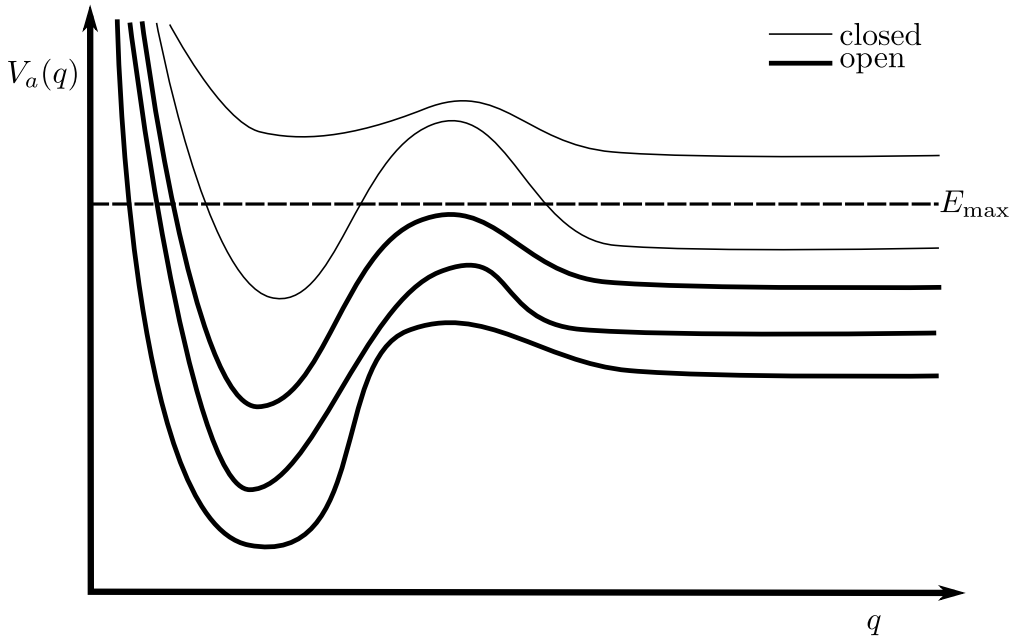

Figure 2.5: Schematic drawing of vibrationally adiabatic potential curves. The channels with barriers below $E_{\max}$ are open and called reactive states.

The steepness of the potential curve is determined by the parameter α. $V_{\text{cent}}(q)$ is a centrifugal potential with an effective rotational constant $B_{\text{cent}}(q)$.

$$V_{\text{cent}}(q) = B_{\text{cent}}(q)J(J+1) \tag{2.102}$$

J is the rotational quantum number. Figure 2.6 shows an exemplary potential curve with its parameters.

The microcanonical reaction rate is calculated as

$$k(E,J) = \frac{W(E,J)}{h \cdot \rho(E,J)} \tag{2.103}$$

where $W(E,J)$ is the number of open channels and $\rho(E,J)$ is the rovibrational density of states. In the Detailed SACM scheme the number of open channels is evaluated explicitly through correlation of reactant and product states. The states are generated by incrementing the vibrational and rotational quantum numbers and sorting by increasing energy. This leads to a large number of reaction channels that need to be generated and makes this method unsuitable for larger systems.

2.3.2 Simplified Statistical Adiabatic Channel Model

The Simplified SACM scheme avoids the problem of explicit correlation of individual states. We assume that the maxima of the channels do not depend on the

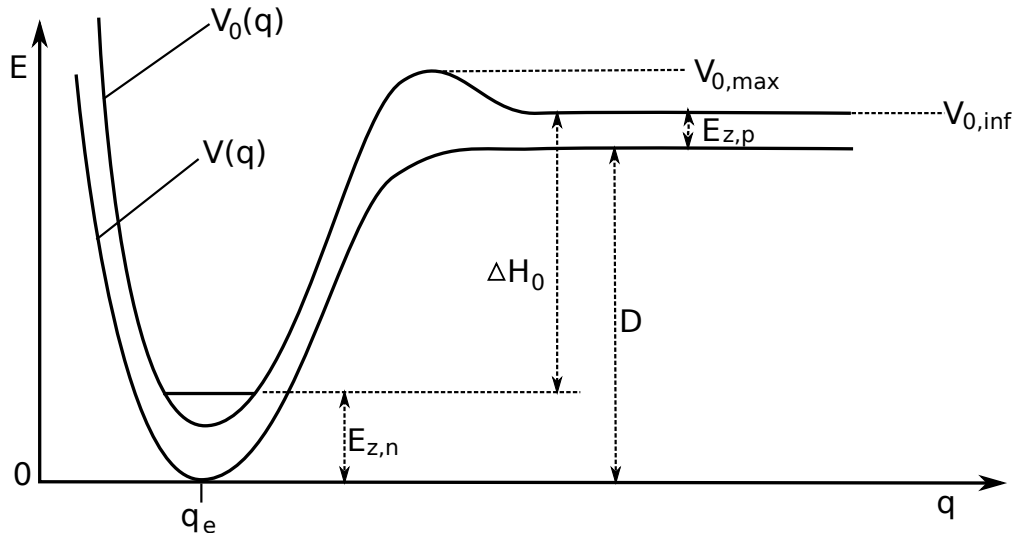

Figure 2.6: Exemplary drawing of a potential curve in the SACM. $V(q)$ is the potential with the equilibrium coordinate q_e and the well depth D. $V_0(q)$ is the lowest adiabatic channel curve with the local maximum $V_{0,max}$. $V_{0,inf}$ is the potential energy of the lowest channel at infinite separation. $E_{z,n}$ and $E_{z,p}$ are the zero point energies of the reactant and product. ΔH_0 is the bond dissociation energy.

conserved modes which reduces the computational effort. The sum of states of the conserved modes is taken into account by convolving their density of states with the number of open channels of the transitional modes. We can use the Beyer-Swinehart algorithm for that task.

Troe has introduced a semiclassical expression for the number of open channels for the transitional modes (see appendix E for details for the derivation).

$$W_l(E) = \frac{\left[\Gamma\left(\frac{1}{2}\right)\right]^r \prod_{j=1}^{l} \Gamma(1+x_j)}{\Gamma\left(\frac{r}{2}+1+\sum_{j=1}^{l} x_j\right)} \cdot \prod_{i=1}^{r}\left(\frac{E}{B_i}\right)^{1/2} \cdot \prod_{j=1}^{l}\left(\frac{E}{\epsilon_j}\right)^{x_j} \tag{2.104}$$

r denotes the number of one-dimensional rotors with rotational constants B_i. l are the number of one-dimensional oscillators with a fitted energy ϵ_j. The parameters x_j and also the eigenvalues for the anharmonic oscillators are calculated with equations that contain empirically fitted parameters. The energy E^* is the energy in excess of the energy at the barrier of the lowest open channel.

Chapter 3

Theoretical Developments and Results

3.1 Population distributions for NRMS 44
3.1.1 Assumptions 44
3.1.2 Population distribution after neutralisation 44
3.1.3 Population distribution after reionisation 47
3.1.4 Practical realization 50
3.1.5 Two-dimensional model system 56
3.1.6 Population distributions for HNSi 59
3.2 Population distributions for Laser cooling 65
3.2.1 Assumptions 65
3.2.2 Population distribution as a function of laser frequency . . . 66
3.2.3 Population distribution as a function of laser frequency with an initial non-Boltzmann population distribution 67
3.2.4 Practical realization 68
First excitation with the laser 68
Relaxation from the excited state 69
Extrapolation 69
Second excitation with the laser 70
Further transitions 71
3.2.5 One-dimensional model system 72
3.3 Theoretical aspects of the COLTRIMS experiment 73
3.3.1 Statistical evaluation of COLTRIMS experiments 73
3.3.2 Multiply charged ion fragments of CHBrClF 77
3.3.3 Reaction pathways for Cold Target Ion Momentum Spectroscopy 81

3.1 Population distributions for NRMS

In NRMS a neutral, stable or metastable species forms when the ionic precursor is neutralized. The neutralization corresponds to a vibronic transition. The neutral molecule flies into another collision chamber and is reionised. Again a vibronic transition occurs. What the experimentalist observes at the detector after the two steps depends on the fragmentations that either the highly reactive neutral intermediate or the reionised molecule undergo. The fragmentation reactions themselves depend on whether reactive channels are populated or not.

In this subsection I will present the derivation of equations and methods for the calculation of vibrational population distributions after the two vibronic transitions that occur during the NRMS experiment.

3.1.1 Assumptions

I want to describe the vibrational population distributions in the NRMS experiment in the framework of FC transitions. Therefore, I assumed that the molecule is neutralised and reionised in a way that is equivalent to a short laser pulse which prevents vibrational dynamics to influence the transition. This assumption seems justified as the collision energies are tipically high (10 keV) and interaction times are short (femtoseconds), so that transitions are vertical. [78]

Further, I assume instantaneous redistribution of the internal energy among all degenerate modes after the neutralization of the molecule and that all neutralized molecules are reionised without undergoing any reactions in between.

3.1.2 Population distribution after neutralisation

The model for the molecule in the NRMS experiment includes two electronic states with harmonic oscillator potentials. The initial system is in its vibrational ground state or has a Boltzmann distributed population of vibrational states. The intermediate state may have a different vibrational frequency and a shifted minimum on the PES. Reionisation leads back to the initial state which is also the final state. Figure 3.1 shows an illustration.

To calculate the population distribution of the intermediate vibrational states the expression for the line spectra given in equation (2.65) may be reused. The argument $E-(E_0+E_{\underline{v'}}-E_{\underline{v}})$ of the Dirac delta distribution is replaced by $E'-E_{\underline{v'}}$. The resulting expression is formally correct, but lacks a weight for the initial state, which will be discussed in more detail in section 3.1.4. We average over possible

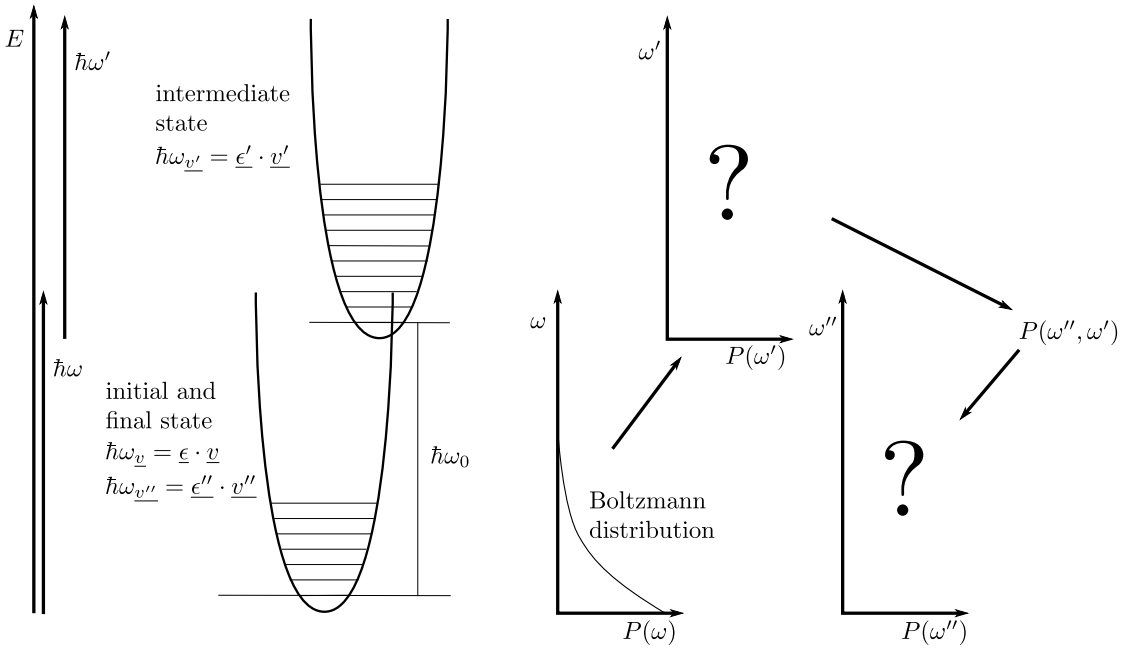

Figure 3.1: Scheme of the model for NRMS. The model includes two electronic states. Both have a harmonic potential. The minimum of the intermediate state is shifted by $\hbar\omega_0$ compared to the minimum of the initial state. The population distribution for the initial state is known and used for the calculation of the distribution in the intermediate state. The population distribution in the final state is calculated from a twodimensional distribution where one parameter is the angular frequency of the intermediate state. This is done for computational reasons (see text).

initial states while we sum over final states.

$$P_{\mathrm{FC}}(E') = \sum_{\underline{v},\underline{v}'=\underline{0}}^{\infty} \left|\langle \underline{v}'|\underline{v}\rangle\right|^2 \delta(E' - E_{\underline{v}'}) \tag{3.1}$$

Since $E = \hbar\omega$, we can also write:

$$P_{\mathrm{FC}}(\hbar\omega') = \sum_{\underline{v},\underline{v}'=\underline{0}}^{\infty} \left|\langle \underline{v}'|\underline{v}\rangle\right|^2 \delta(\hbar(\omega' - (\omega_0 + \omega_{\underline{v}'}))) \tag{3.2}$$

This modified delta distribution selects all transitions that lead to a state with internal energy $\omega_{\underline{v}'}$ in the intermediate electronic state. I obtain analogue results for the generating function ansatz as described in chapter 2 (see equations (2.79),

(2.89), (2.98)).

$$P_{\mathrm{FC}}(E') = |\langle \underline{0}'|\underline{0}\rangle|^2 \, G(\boldsymbol{I})\delta(E' - E_{\underline{v}'}) \tag{3.3}$$

$$P_{\mathrm{FCW}}(E';T) = \mathcal{N}\,|\langle \underline{0}'|\underline{0}\rangle|^2 \, G(\boldsymbol{I};\boldsymbol{\Lambda})\delta(E' - E_{\underline{v}'}) \tag{3.4}$$

$$P_{\mathrm{FCW}}(\hbar\omega';T) = \mathcal{N}\frac{1}{\hbar}\,|\langle \underline{0}'|\underline{0}\rangle|^2 \int\limits_{-\infty}^{\infty} dt\, G(\boldsymbol{Z}(t);\boldsymbol{\Lambda})\mathrm{e}^{\mathrm{i}(\omega'-\omega_0)t} \tag{3.5}$$

The expressions are correct with a newly defined $\boldsymbol{Z}$. The Fourier transformation of the delta distribution leads to a slightly different generating function compared to equation (2.75) from which we can infer $\boldsymbol{Z}$.

$$\delta(E' - E_{\underline{v}'}) = \frac{1}{\hbar}\int\limits_{-\infty}^{\infty} \mathrm{d}t\, \mathrm{e}^{\mathrm{i}(\omega'-\omega_0)t}\mathrm{e}^{-\mathrm{i}\frac{\epsilon' v'}{\hbar}t} \tag{3.6}$$

$$G(\tilde{\boldsymbol{Z}},t) = \sum_{\underline{v},\underline{v}'=\underline{0}}^{\infty} q(\underline{v}';\underline{v}) \prod_{k=1}^{N}\left[\left(\tilde{z}'_k \exp\left(-\mathrm{i}\frac{\epsilon'_k}{2\hbar}t\right)\right)^{2v'_k}(\tilde{z}_k)^{2v_k}\right] \tag{3.7}$$

$$G(\boldsymbol{Z}(t)) = \sum_{\underline{v},\underline{v}'=\underline{0}}^{\infty} q(\underline{v}';\underline{v}) \prod_{k=1}^{N}\left[(z'_k(t))^{2v'_k}(z_k(t))^{2v_k}\right] \tag{3.8}$$

I then need to choose the elements of the matrix $\boldsymbol{Z}(t)$ as

$$z_k = \tilde{z}_k \tag{3.9}$$

$$z'_k = \exp\left(-\mathrm{i}\frac{\epsilon'_k}{2\hbar}t\right)\tilde{z}'_k \tag{3.10}$$

with $\tilde{z}_k = 1$ and $\tilde{z}'_k = 1$.

3.1.3 Population distribution after reionisation

The vibrational population distribution after reionisation cannot be calculated in the same way as the distribution after the neutralisation. In this case the initial population distribution is specifically known, but does not necessarily correspond to a Boltzmann distribution. In a first attempt to solve this problem I could show that simple serial computation of the distributions imposes another problem: The vibrational population distribution as calculated with equation 3.5 provides population intensities as a function of internal energy, but it does not include information on the degeneracy of the intermediate states. We do not know if all the population is on one single state or if it is distributed over several degenerate states, but we assume that it is immediately distributed over all levels with the same energy.

Therefore, the degeneracy factor is necessary to avoid overcounting of population when summing over the intermediate states. We assume that the population is distributed statistically over the degenerated states. The population in one of the states is then

$$g(\omega_{\underline{v}'})P(\omega_{\underline{v}'}) \tag{3.11}$$

where g is the degeneracy factor. The time-independent KDB algorithm offers the possibility to determine the degeneracy factor, but in the more efficient time-dependent picture it is unavailable in an analytical way.

I propose an ansatz for a two-dimensional population distribution:

$$P(\omega'', \omega') = \mathcal{N} \sum_{\underline{v}', \underline{v}''=\underline{0}}^{\infty} \frac{1}{\rho(\omega_{\underline{v}'})} P(\omega_{\underline{v}'}) \left|\langle \underline{v}'' | \underline{v}' \rangle\right|^2 \delta(\hbar(\omega' - (\omega_0 + \omega_{\underline{v}'})))\delta(\hbar(\omega'' - (\omega_0' + \omega_{\underline{v}''}))). \tag{3.12}$$

ω' and $\underline{v}'$ would be the energy and occupation number vector in the intermediate state (neutral molecule) and ω'' and $\underline{v}''$ the energy and occupation number vector in the final state. ω_0 is the zero point energy difference between the initial and the intermediate state. ω_0' is the zero point energy difference between the initial and the final state. In the case the molecule is reionised to its initial ionic form ω_0' is 0 (as assumed here). $\rho(\omega)$ is the density of states in the intermediate state at the energy corresponding to ω. $\frac{1}{\rho(\omega)}$ therefore denotes the degeneracy factor. The population distribution in the intermediate state with the corresponding degeneracy factor is used to weight the FCF for the transition from the intermediate to the final state. If we now use the property of the degeneracy factor of being equal for all states of the same energy, which is of course trivial, we can move the product $\frac{1}{\rho(\omega')}P(\omega')$ before the sum whenever $\omega_{\underline{v}'} = \omega'$. All other summands are zero so that we can

write

$$P(\omega'',\omega') = \mathcal{N}\frac{1}{\rho(\omega')}P(\omega')\sum_{\underline{v'},\underline{v''}=\underline{0}}^{\infty}\left|\langle\underline{v''}|\underline{v'}\rangle\right|^2\delta(\hbar(\omega'-(\omega_0+\omega_{\underline{v'}})))\delta(\hbar(\omega''-(\omega_0'+\omega_{\underline{v''}}))). \tag{3.13}$$

We then use equation (3.2) with an adapted nomenclature to replace the population of the intermediate state:

$$\begin{aligned}P(\omega'',\omega') =&\frac{\mathcal{N}\mathcal{N}'}{\rho(\omega')}\sum_{\underline{v'},\underline{v}=\underline{0}}^{\infty}\left|\langle\underline{v'}|\underline{v}\rangle\right|^2\delta(\hbar(\omega'-(\omega_0+\omega_{\underline{v'}})))\\ &\sum_{\underline{v'},\underline{v''}=\underline{0}}^{\infty}\left|\langle\underline{v''}|\underline{v'}\rangle\right|^2\delta(\hbar(\omega'-(\omega_0+\omega_{\underline{v'}})))\delta(\hbar(\omega''-(\omega_0'+\omega_{\underline{v''}}))).\end{aligned} \tag{3.14}$$

Now we use the time-dependent form of the Dirac delta distribution to obtain

$$\begin{aligned}P(\omega'',\omega') =&\frac{\mathcal{N}\mathcal{N}'}{\rho(\omega')}\frac{1}{\hbar^3}\int_{-\infty}^{\infty}\mathrm{d}t\sum_{\underline{v'},\underline{v}=\underline{0}}^{\infty}\left|\langle\underline{v'}|\underline{v}\rangle\right|^2\exp(\mathrm{i}(\omega'-\omega_0-\omega_{\underline{v'}})t)\\ &\int_{-\infty}^{\infty}\mathrm{d}t\int_{-\infty}^{\infty}\mathrm{d}t'\sum_{\underline{v'},\underline{v''}=\underline{0}}^{\infty}\left|\langle\underline{v''}|\underline{v'}\rangle\right|^2\exp(\mathrm{i}(\omega'-\omega_0-\omega_{\underline{v'}})t)\exp(\mathrm{i}(\omega''-\omega_0'-\omega_{\underline{v''}})t')\\ =&\frac{\mathcal{N}\mathcal{N}'}{\rho(\omega')}\frac{1}{\hbar^3}\int_{-\infty}^{\infty}\mathrm{d}t\sum_{\underline{v'},\underline{v}=\underline{0}}^{\infty}\left|\langle\underline{v'}|\underline{v}\rangle\right|^2\exp\left(-\mathrm{i}\frac{\underline{\epsilon'}\cdot\underline{v'}}{\hbar}t\right)\exp(\mathrm{i}(\omega'-\omega_0)t)\\ &\int_{-\infty}^{\infty}\mathrm{d}t\int_{-\infty}^{\infty}\mathrm{d}t'\sum_{\underline{v'},\underline{v''}=\underline{0}}^{\infty}\left|\langle\underline{v''}|\underline{v'}\rangle\right|^2\exp\left(-\mathrm{i}\frac{\underline{\epsilon''}\cdot\underline{v''}}{\hbar}t'\right)\exp(\mathrm{i}(\omega''-\omega_0')t')\\ &\exp\left(-\mathrm{i}\frac{\underline{\epsilon'}\cdot\underline{v'}}{\hbar}t\right)\exp(\mathrm{i}(\omega'-\omega_0)t).\end{aligned} \tag{3.15}$$

We set up a one-dimensional generating function and a two-dimensional generating function. The one-dimensional generating function is equivalent to the one obtained in the last section:

$$G(\boldsymbol{Z}(t)) = \sum_{\underline{v'},\underline{v}=\underline{0}}^{\infty}\frac{\left|\langle\underline{v'}|\underline{v}\rangle\right|^2}{\left|\langle\underline{0'}|\underline{0}\rangle\right|^2}\prod_{k=1}^{N}\left[\left(z_k'(t)\right)^{2v_k'}\left(z_k(t)\right)^{2v_k}\right] \tag{3.16}$$

$$G'(\boldsymbol{Z}(t,t')) = \sum_{\underline{v'},\underline{v''}=\underline{0}}^{\infty}\frac{\left|\langle\underline{v'}|\underline{v''}\rangle\right|^2}{\left|\langle\underline{0'}|\underline{0}\rangle\right|^2}\prod_{k=1}^{N}\left[\left(z_k''(t')\right)^{2v_k''}\left(z_k'(t)\right)^{2v_k'}\right] \tag{3.17}$$

with

$$z_k = 1 \tag{3.18}$$

$$z'_k = \exp\left(-\mathrm{i}\frac{\epsilon'_k}{2\hbar}t\right) \tag{3.19}$$

$$z''_k = \exp\left(-\mathrm{i}\frac{\epsilon''_k}{2\hbar}t'\right). \tag{3.20}$$

For the two-dimensional population distribution including the thermal dependence we end up with

$$\begin{aligned} P_{\mathrm{FCW}}(\omega'', \omega'; T) =& \frac{\mathcal{N}\mathcal{N}'}{\rho(\omega')} \frac{1}{\hbar^3} \left|\langle \underline{0}'|\underline{0}\rangle\right|^4 \int_{-\infty}^{\infty} \mathrm{d}t\, G(\boldsymbol{Z}(t); \boldsymbol{\Lambda}) \exp(\mathrm{i}(\omega' - \omega_0)t) \\ & \int_{-\infty}^{\infty} \mathrm{d}t \int_{-\infty}^{\infty} \mathrm{d}t'\, G'(\boldsymbol{Z}(t, t')) \exp(\mathrm{i}(\omega'' - \omega'_0)t') \exp(\mathrm{i}(\omega' - \omega_0)t). \end{aligned} \tag{3.21}$$

3.1.4 Practical realization

I want to give an overview of the algorithm and discuss some specific issues of the numerical implementation. In practice the solution can be obtained in six steps:

1. Generate $G(\boldsymbol{Z}(t))$. (Fourier transform of $G(\boldsymbol{Z}(t))$ produces the population distribution after the neutralisation, but is not necessary here.)

2. Generate $G'(\boldsymbol{Z}(t,t'))$ with $\boldsymbol{Z} = \mathrm{diag}(\mathrm{e}^{-\mathrm{i}\frac{\epsilon'}{2\hbar}t}, \mathrm{e}^{-\mathrm{i}\frac{\epsilon}{2}t'})$.

3. Fourier transform $G'(\boldsymbol{Z}(t,t'))$ over t' to obtain $\mathcal{F}\{G'(Z(t,t'))\}$.

4. Convolve $G(\boldsymbol{Z}(t))$ and $\mathcal{F}\{G'(\boldsymbol{Z}(t,t'))\}$. The numerical convolution formula is $\{A * B\}_s = \sum_r A_r B_{s-r}$ where A and B are lists with n_A and n_B number of elements. The limits of r are chosen such that $s - r$ is never negative, but each sum has n_A summands and $A * B$ has the length n_B.

5. Fourier transform the convoluted result over t. Here the *Convolution theorem* is used in order to rewrite equation (3.21):

$$\mathcal{F}\{f * g\} = \mathcal{F}\{f\} \cdot \mathcal{F}\{g\}$$

$$\begin{aligned} P(\omega'', \omega') = & \frac{\mathcal{N}\mathcal{N}'}{\rho(\omega')} \frac{1}{\hbar^3} \left|\langle \underline{0}' | \underline{0} \rangle\right|^4 \\ & \int_{-\infty}^{\infty} \mathrm{d}t \left[G(\boldsymbol{Z}(t)) * \left(\int_{-\infty}^{\infty} \mathrm{d}t'\, G'(\boldsymbol{Z}(t,t')) \exp(\mathrm{i}(\omega'' - \omega_0')t') \right) \right] \\ & \exp(\mathrm{i}(\omega' - \omega_0)t) \end{aligned} \tag{3.22}$$

6. In order to obtain $P(\omega'')$ from $P(\omega'', \omega')$ sum over ω' weighted with the degeneracy factor. I used the Beyer-Swinehart algorithm to calculate the density of states. [76]

An alternative way of getting the same result is with fewer Fourier transformations:

1. Generate $G(\boldsymbol{Z}(t))$.
2. Generate $G'(\boldsymbol{Z}(t,t'))$.
3. Convolve $G(\boldsymbol{Z}(t))$ and $G'(\boldsymbol{Z}(t,t'))$.
4. Fourier transform the convoluted result over t.
5. Weight with the degeneracy factor and sum over ω'.
6. Fourier transform the sum over t'. The exchange of summation and Fourier transform is possible since the Fourier transform is a linear operation.

$$\mathcal{F}\{f+g\} = \mathcal{F}\{f\} + \mathcal{F}\{g\}$$

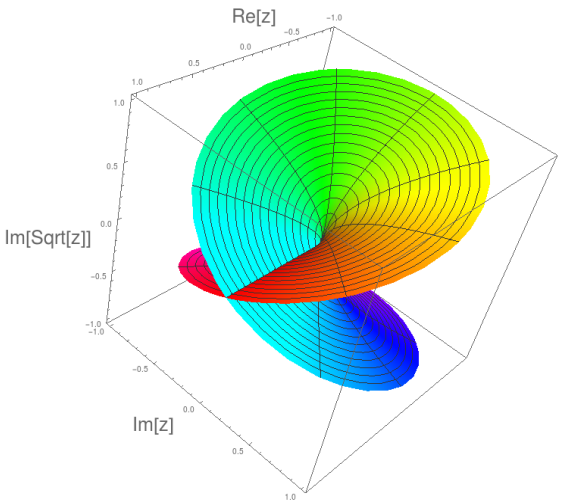

Figure 3.2: Riemann surface of the complex square root function. The function is only unambiguously defined for positive real numbers. Otherwise the surface shows two branches.

In the course of my work on this topic I encountered two numerical issues of the described method: The first one resulted from the calculation of the square root in the equation for the generating function in the spatial representation (See,

e.g., equation (2.77)). The elements of the matrix $\boldsymbol{Z}$ can be complex numbers and so the resulting determinant can be a complex number as well. The square root of a complex number is not unique. This is illustrated by the Riemann surface of the complex square root function in figure 3.2. The two branches only cross at the positive real axis, where the root is unambiguously defined. Common implementations of the complex square root function return the so called *principal square root*. For the application in the time-dependent method we calculate values for the generating function not independently, but in form of a continuous trajectory. The reader might imagine to travel along one of the branches until he reaches the crossing, the branch cut, where he, for continuity, changes the branch and so on. If the principal square root is used he would be hindered to change the branch, which leads to a discontinuity in the trajectory.

I solved this problem by tracking the so called Maslov index. [79] It counts the transitions through the branch cut and allows to change signs of the square root manually. A simple implementation might look as follows [80]. The symbols are *rad* for the radicant and *num* for the result.

```
if ((Real(rad[i])<0.0) && (Imag(rad[i])*Imag(rad[i-1])<0.0))
{
   maslov_index = maslov_index + 1;
}
maslov = (-1)^maslov_index;
num[i] = maslov * sqrt(rad[i]);
```

The second numerical issue results from the infinite summation over occupation number vectors as, e.g., in equations (3.16) and (3.17). This prevents the numerical solution of equation (3.21). In all former calculations this issue was solved by confining the initial state population distribution to the Boltzmann distribution (see subsection 2.2.5). In the reionisation step I have explicitly not used a Boltzmann distribution, but the population distribution of the neutralisation step (first integral in equation (3.21)). However, the convolution with the generating function of the first transition is performed *after* we calculated the generating function for the second transition which does not converge. Therefore, equation (3.21) is not exactly solvable.

I introduced a Boltzmann distribution also for the second transition in equation 3.21 and in that way solved the problem.

$$P_{\mathrm{FCW}}(\omega'', \omega'; T, T') = \frac{\mathcal{N}\mathcal{N}'}{\rho(\omega')} \frac{1}{\hbar^3} \left|\langle \underline{0}'|\underline{0}\rangle\right|^4 \int_{-\infty}^{\infty} \mathrm{d}t\, G(\boldsymbol{Z}(t); \boldsymbol{\Lambda}) \exp(\mathrm{i}(\omega' - \omega_0)t) \int_{-\infty}^{\infty} \mathrm{d}t \int_{-\infty}^{\infty} \mathrm{d}t'\, G'(\boldsymbol{Z}(t, t'); \boldsymbol{\Lambda}') \exp(\mathrm{i}(\omega'' - \omega_0')t') \exp(\mathrm{i}(\omega' - \omega_0)t). \tag{3.23}$$

The error introduced by the Boltzmann distribution decreases with higher temperatures, as the value of the Fourier transformation of the Boltzmann distribution decreases slower in those cases. Figure 3.3 depicts the function for different temperatures. Table 3.1 lists values for the integral (in practice calculated as a discrete sum) over the resulting population distribution with an upper limit of $3000\,\mathrm{cm}^{-1}$ and different temperatures for the Boltzmann distribution in the intermediate state. One needs to make sure that the Boltzmann distribution is well decayed within the energy range by choosing a high enough temperature.

$$\int_{2\pi c \cdot 0\,\mathrm{cm}^{-1}}^{2\pi c \cdot 3000\,\mathrm{cm}^{-1}} P(\omega')\, \mathrm{d}\omega' \tag{3.24}$$

Table 3.1: Integral values over the resulting population distribution according to equation (3.24) for a one-dimensional system with different temperatures for the Boltzmann distribution at the intermediate state. The correct total integral is 1. Parameters are $\epsilon = 20\ hc \cdot \mathrm{cm}^{-1}$, $\epsilon' = 60\ hc \cdot \mathrm{cm}^{-1}$, $\delta = 1$, Upper Limit $= 3000\ hc \cdot \mathrm{cm}^{-1}$ and graining $\Delta = 10\ hc \cdot \mathrm{cm}^{-1}$.

Temperature	Integral eq. (3.24)
50 K	0.69
200 K	0.80
500 K	0.89
800 K	0.93
1000 K	0.94
2000 K	0.97

To avoid the problem due to infinite summation in the generating function, one may not only introduce a Boltzmann distribution, but can also use any other

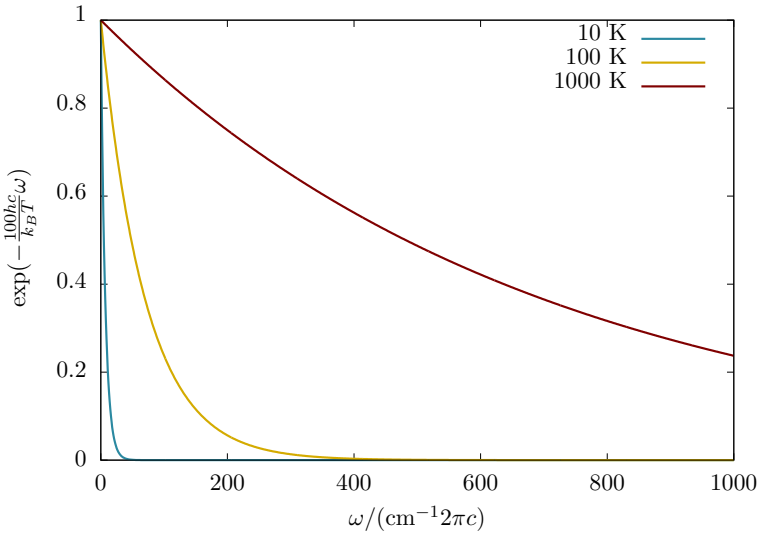

Figure 3.3: Fourier transform of the Boltzmann distribution for different temperatures. The *ideal* function would be 1 over the whole range. In practice we can only choose a high enough temperature to have the relevant frequency range preserved.

function with an exponential dependence in the energy, that decays to zero within an energy range that is still computable. One example of such a function is

$$D_i = b^{\omega'} \exp\left(-\mathrm{i}a_i\omega'\right) \tag{3.25}$$

The coefficient b needs to be chosen specifically for the problem and depends on the width of the population distribution after the first transition. In the specific case that is shown in figure 3.4 I chose $b = 0.99$. The advantage of this function is that it is also suitable to use it as a basis function to represent the population distribution in the intermediate state. The exponential coefficients were gerenerated as

$$a_1 = 1 \tag{3.26}$$
$$a_i = 1.5 \cdot a_{i-1}, i \in \{2, 3, ..., N\} \tag{3.27}$$

Therefore, we may use the ansatz

$$P'(\omega') = \sum_i c_i D_i \tag{3.28}$$

We insert this into equation 3.12. This leads to the following generation function

$$
\begin{aligned}
G'(\boldsymbol{Z}(t,t')) = & \sum_{\underline{\tilde{v}'},\underline{v_f}=\underline{0}}^{\infty} \frac{\left|\left\langle \underline{\tilde{v}'}|\underline{v_f}\right\rangle\right|^2}{\left|\langle \underline{0'}|\underline{0}\rangle\right|^2} \prod_{k=1}^{N} \left[\left(\tilde{z}_k \exp\left(-\mathrm{i}\frac{\tilde{\epsilon}'_k}{2\hbar}t\right)\right)^{2\tilde{v}_k} \left(z_{fk} \exp\left(-\mathrm{i}\frac{\epsilon_{fk}}{2\hbar}t'\right)\right)^{2v_{fk}} \right] \\
& \sum_i c_i \exp\left(-\mathrm{i}a_i \underline{\tilde{\epsilon}'\tilde{v}'}\right) \\
= & \sum_i c_i \sum_{\underline{\tilde{v}'},\underline{v_f}=\underline{0}}^{\infty} \frac{\left|\left\langle \underline{\tilde{v}'}|\underline{v_f}\right\rangle\right|^2}{\left|\langle \underline{0'}|\underline{0}\rangle\right|^2} \\
& \prod_{k=1}^{N} \left[\left(\tilde{z}_k \exp\left(-\mathrm{i}\frac{\tilde{\epsilon}'_k}{2\hbar}t\right) \exp\left(-\mathrm{i}\frac{a_i\tilde{\epsilon}'_k}{2}\right)\right)^{2\tilde{v}_k} \left(z_{fk} \exp\left(-\mathrm{i}\frac{\epsilon_{fk}}{2\hbar}t'\right)\right)^{2v_{fk}} \right] \\
= & \sum_i c_i G'_i(\boldsymbol{Z}(t,t')) \qquad (3.29)
\end{aligned}
$$

In practice the extra exponential can be incorporated into $\boldsymbol{W}$ and $\boldsymbol{r}$ in the same way as it is done with the Boltzmann distribution. This avoids the calculation of a time-independent factor for every time step.

This ansatz works well and gives an acceptable population distribution, but one needs to include at least one basis function D_i for every time step. For every basis function one needs to calculate a new generating function G'_i. The calculation time should therefore increase linearly with the number of basis functions. An example result is shown in figure 3.4 in comparison with the exact result from the time-independent method that uses the KDB algorithm. Even though the total integral is with 0.986 quite close to unity, at some energies the population is overestimated while others are underestimated. Overall, I evaluate the ansatz with a second Boltzmann distribution to be more practical than the expansion ansatz.

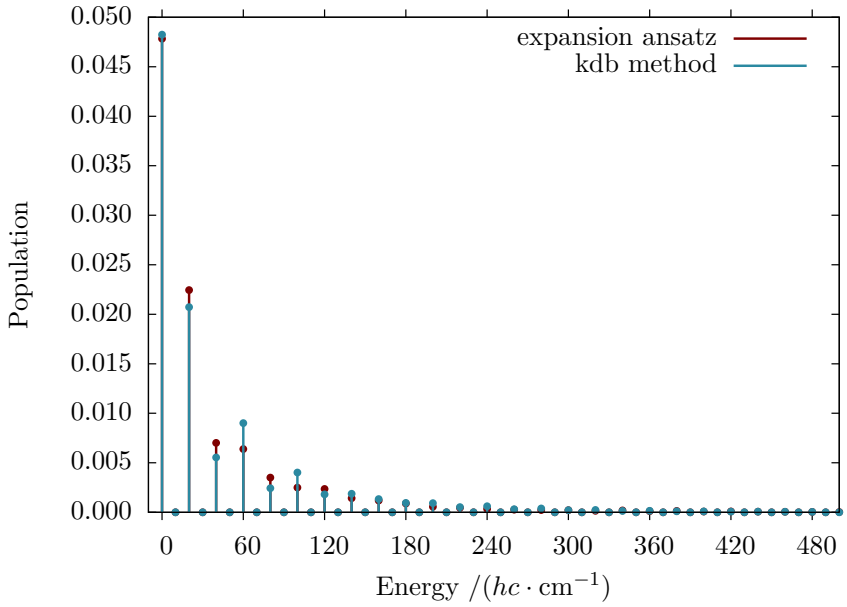

Figure 3.4: Population distribution calculated with the KDB algorithm (blue) and the time-dependent method using the expansion ansatz from equation (3.29) (red). The test system has one vibrational degree of freedom with with wave numbers $20\,\mathrm{cm}^{-1}$ in the initial state and $60\,\mathrm{cm}^{-1}$ in the intermediate state. The Duschinski δ was chosen to be 1.0.

3.1.5 Two-dimensional model system

I tested my developments for the calculation of vibrational population distributions on a two-dimensional system. I chose this system because it represents the simplest test case which allows to test all features of the equations. From this system a transfer to larger systems should impose no obstacles. The initial and final state are chosen to be identical as in the previously described model. I evaluated the generating function at specific points in time such that I obtained the resulting Fourier transform with a graining Δ and up to the energy which is here called Upper Limit. The parameters for the two-dimensional system are listed in table 3.2.

For comparison I additionally calculated the vibrational population distributions with the time-independent KDB algorithm. Figure 3.5 shows the population after neutralisation, figure 3.6 shows the population after reionisation.

I was able to calculate the identical population distribution with the time-dependent method as with the time-independent method for the intermediate state. The population correctly adds up to one. The total population after the second transition is 0.913 in case of the time-dependent method. This is due to the additional Boltzmann distribution, for which I chose 1000 K. The energies

Table 3.2: Parameters for the two-dimensional test system.

Parameter	Value
$\underline{\epsilon}/(hc \cdot \mathrm{cm}^{-1})$	$(20, 50)^t$
$\underline{\epsilon'}/(hc \cdot \mathrm{cm}^{-1})$	$(60, 70)^t$
$\boldsymbol{S}$	$\begin{pmatrix} 0.25 & 0.94 \\ -0.94 & 0.5 \end{pmatrix}$
$\underline{\delta}$	$(1.0, 0.5)^t$
$\omega_0/(2\pi c \cdot \mathrm{cm}^{-1})$	0[1]
Temperature/K	0
Upper Limit/$(hc \cdot \mathrm{cm}^{-1})$	3000
Graining/$(hc \cdot \mathrm{cm}^{-1})$ Δ	10
Number of sample points N	1024
Time steps	$(c \cdot 10^{-10}\Delta \cdot 2N)^{-1}$

[1]arbitrary value which only influences the shift of the energy axis

at which the peaks appear agree with the result from the KDB algorithm. The discrepancy could be decreased with a flatter Boltzmann distribution, but at the cost of more calculation points.

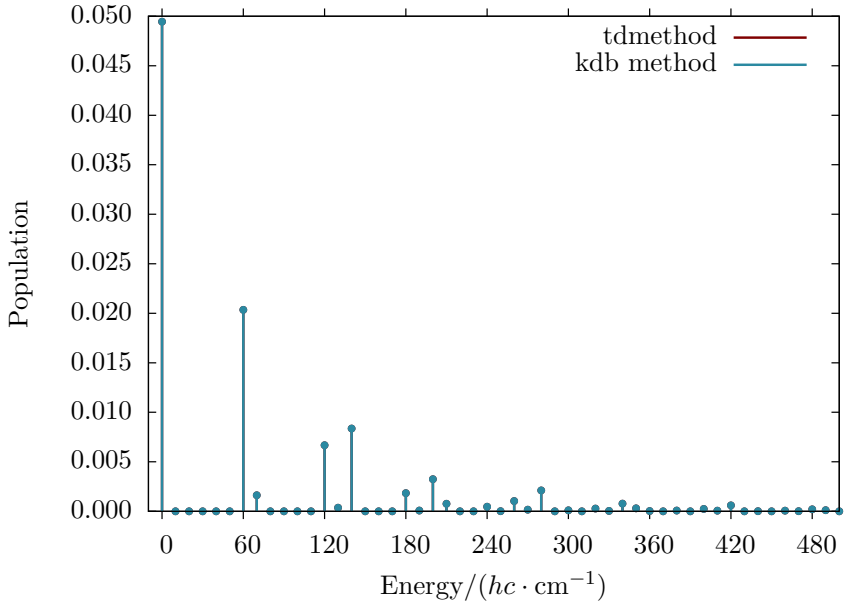

Figure 3.5: Vibrational population distribution for a two-dimensional system (see table 3.2) after the first transition. The peaks from the time-dependent method and the time-independent algorithm lie on top of each other.

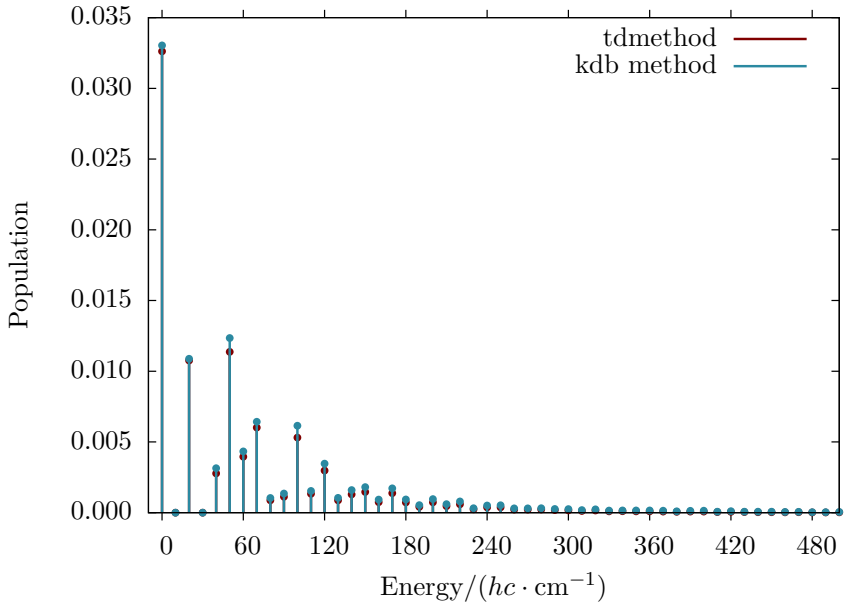

Figure 3.6: Vibrational population distribution for a two-dimensional system (see table 3.2) after the second transition. The time-dependent method shows deviations from the accurate time-independent algorithm.

3.1.6 Population distributions for HNSi

I applied the developed and tested theory to the linear molecule HNSi. I chose this system, because it has a modest size and undergoes small geometry changes during transition from the cation to the neutral molecule. In this case the FC matrix has a high diagonality and the population distribution will not shift too strongly to higher energies. Thus, I can choose a lower temperature for the Boltzmann distribution and a smaller calculation interval. Furthermore, Goldberg et al. have done calculations on HNSi without encountering multi-reference problems. [81] The parameters for my calculation are listed in table 3.3.

Table 3.3: Parameters for the calculation of vibrational population distributions for the $^{+}NR^{+}$ experiment on HNSi. I took the equilibrium structures of HNSi and $HNSi^{+\cdot}$ from Goldberg et al. [81] and reoptimized them with $MP2/6-311G^{**}$ using the quantum chemistry program Turbomole [82]. The calculation for HNSi was of closed-shell type, the calculation for $HNSi^{+\cdot}$ was of unrestricted open-shell type. I calculated the harmonic vibrational frequencies with analytic gradients. Then I used them together with the equilibrium structures as an input for hotFCHT [83, 84, 16, 15] and obtained the Duschinski matrix and vector. I rounded the harmonic vibrational wave numbers to the nearest $10\,\mathrm{cm}^{-1}$ for the calculation of the population distribution.

Parameter	Value
$\underline{\epsilon}/(hc\cdot\mathrm{cm}^{-1})$	$(1060, 1060, 1620, 3760)^t$
$\underline{\epsilon'}/(hc\cdot\mathrm{cm}^{-1})$	$(560, 560, 1190, 3770)^t$
$\boldsymbol{S}$	$\begin{pmatrix} 9.99815561\cdot10^{-1} & -1.92052994\cdot10^{-2} & 0.00000000 & 0.00000000 \\ 1.92052994\cdot10^{-2} & 9.99815561\cdot10^{-1} & 0.00000000 & 0.00000000 \\ 0.00000000 & 0.00000000 & 9.99926580\cdot10^{-1} & 0.00000000 \\ 0.00000000 & 0.00000000 & 0.00000000 & -9.99926580\cdot10^{-1} \end{pmatrix}$
$\underline{\delta}$	$(1.21554198\cdot10^{-1}, 1.83444710, 0.00000000, 0.00000000)^t$
$\omega_0/(2\pi c\cdot\mathrm{cm}^{-1})$	0[1]
Temperature/K	0
Upper Limit$/(hc\cdot\mathrm{cm}^{-1})$	200000
Graining $\Delta/(hc\cdot\mathrm{cm}^{-1})$	10
Number of sample points N	65536
Temperature for relaxation/K	10000
Time steps	$(c\cdot10^{-10}\Delta\cdot2N)^{-1}$

[1] arbitrary value which only influences the shift of the energy axis

Figures 3.7 and 3.8 show the vibrational population distributions after the neutralisation and reionisation steps. I convoluted the result for the second transition with a Lorentzian line shape function. After the first transition the peaks are well resolved and the population is not yet shifted to high energies. After the second

transition the distribution is shifted to higher energies. It needs to be emphasized that the results could in principle be obtained by the time-independent KDB algorithm, but because of the four vibrational degrees of freedom of neutral and cationic HNSi this would require a much longer computation time.

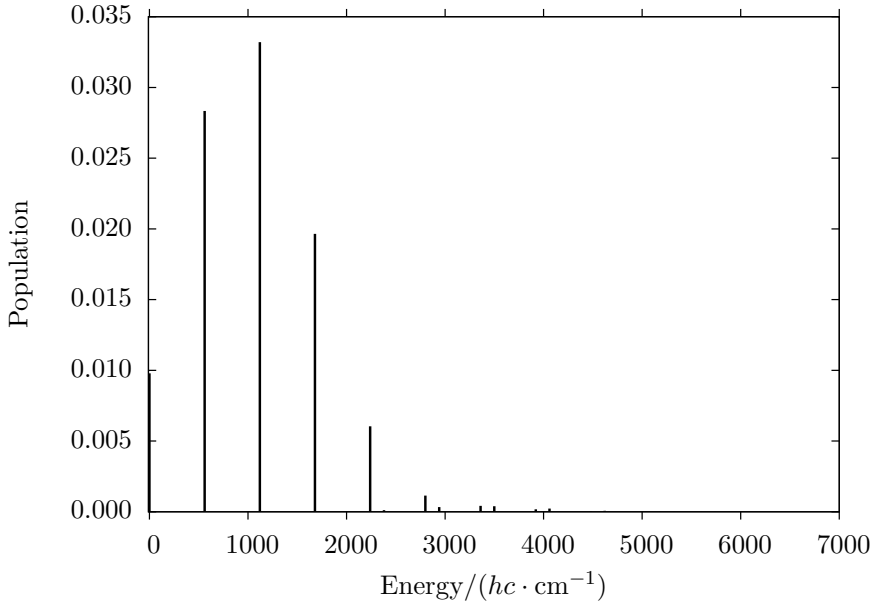

Figure 3.7: Vibrational population distribution of HNSi after the first transition.

In order to compare my results with experimental data I calculated dissociation rates with the Simplified SACM assuming Morse potentials which is defined as

$$V(q) = D_e \left[1 - \mathrm{e}^{-\beta(q-r_0)}\right]^2 . \tag{3.30}$$

The parameters are listed in tables 3.4 and 3.5. The calculations were done for the dissociation channels

$$\mathrm{HNSi(singlet)} \rightarrow \mathrm{NH(triplet)} + \mathrm{Si(triplet)} \tag{3.31}$$
$$\mathrm{HNSi^{+\cdot}(doublet)} \rightarrow \mathrm{NH(triplet)} + \mathrm{Si^{+\cdot}(doublet)} \tag{3.32}$$
$$\mathrm{HNSi^{+\cdot}(doublet)} \rightarrow \mathrm{NH^{+\cdot}(doublet)} + \mathrm{Si(triplet)} \tag{3.33}$$
$$\mathrm{HNSi(singlet)} \rightarrow \mathrm{NSi^{\cdot}(doublet)} + \mathrm{H^{\cdot}(doublet)} \tag{3.34}$$
$$\mathrm{HNSi^{+\cdot}(doublet)} \rightarrow \mathrm{NSi^{\cdot}(doublet)} + \mathrm{H^{+}} \tag{3.35}$$
$$\mathrm{HNSi^{+\cdot}(doublet)} \rightarrow \mathrm{NSi^{+}(singlet)} + \mathrm{H^{\cdot}(doublet)}. \tag{3.36}$$

Figure 3.9 shows the dissociation rate constants as a function of energy. I assumed that a dissociation can only occur when the vibrational states above a certain

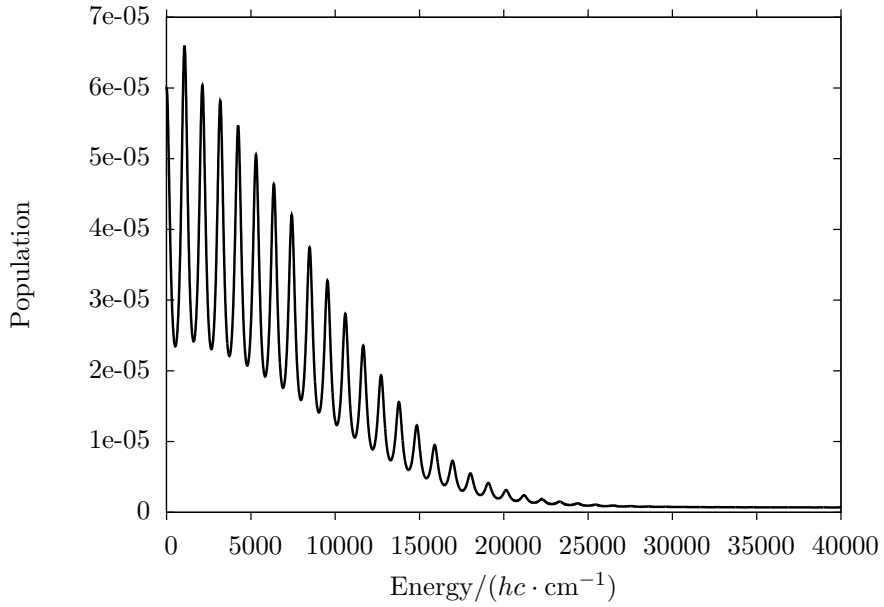

Figure 3.8: Vibrational population distribution of $HNSi^{+\cdot}$ after the second transition. The signals were convoluted with a Lorentzian line shape function.

threshold are populated. The threshold is defined by the energy barriers of the dissociation channels. When the threshold energy of a reaction is overcome the dissociation rate increases rapidly and then flattens. The curvature of the channel potential is connected to the slope of the reaction rate coefficient. A steep potential usually corresponds to a lower density of states, which according to

$$k(E) = \frac{W(E)}{h \cdot \rho(E)} \tag{3.37}$$

leads to a higher rate coefficient that levels off slower. I deduce from comparison of the SACM results with the population distribution in figure 3.7 that the neutral HNSi molecule is stable in the gas phase experiment. This agrees with the high intensity of the recovery signal in the NRMS experiment. [81]

After reionisation the barrier for the dissociation of HNSi into NH and $Si^{+\cdot}$ is in the energy range where the population distribution is nonzero, but intensities are very small. The population at higher energies might increase, in case the simulation temperature is not chosen as 0 K but, e.g., as room temperature. This would broaden the initial population distribution. The experimental spectrum shows a small signal of $Si^{+\cdot}$ and also of NSi^{+}. The latter one could not be predicted with the calculation results as this channel opens up only at higher energies.

A source of error is the description of all oscillators as harmonic oscillators. As harmonic potentials do not allow for dissociation, their use in this context is clearly

a crude approximation. Furthermore, the transitions in the NRMS experiment might not be strictly FC-like. Both limitations can, however, be removed, such that this study provides a starting point for further theoretical developments.

Table 3.4: Parameters for the dissociation rate calculation with the Simplified SACM. I chose the Morse potential parameter β and the parameter α as 1.0. The graining for the direct count algorithm was $100\,\mathrm{cm}^{-1}$. The orbital occupation for the fragments was obtained with an Extended Hückel guess, except for NSi^+ where I chose the more stable triplet state. NH and Si were in the lowest triplet state, NH^+, NSi and Si^+ in the doublet state. I did not account for spin couplings or degeneracies.

Reaction[1]	J	D_e [2]	r_0[3]	Angular momentum coupling factors [4]
(3.31)	0	52625.09	1.56590	atom + linear
(3.32)	0	24606.87	1.46706	atom + linear
(3.33)	0	69389.41	1.46706	atom + linear
(3.34)	0	49603.04	1.00455	atom + linear
(3.35)	0	68389.01	1.00614	atom + linear
(3.36)	0	37591.31	1.00614	atom + linear

[1]Refers to the equation number in the text.
[2]In units of cm^{-1}.
[3]In units of angstrom.
[4]As in table I in reference [56].

Table 3.5: Vibrational modes of HNSi, $HNSi^{+\cdot}$ and its fragments. t = transitional mode, rc = reaction coordinate, c = conserved mode.

Species	Wavenumbers [1]	Description	Used as for 3.31 - 3.33	Used as for 3.34 - 3.36	Rotational constants[1]
HNSi	555.52	bend	t	t	0.6231828505
	555.52	bend	t	t	0.6231828505
	1191.11	stretch	rc	c	0.0000000000
	3765.48	stretch	c	rc	
$HNSi^{+\cdot}$	1056.44	bend	t	t	0.7025924074
	1056.44	bend	t	t	0.7025924074
	1622.98	stretch	rc	c	0.0000000000
	3763.01	stretch	c	rc	
NH	3393.14	stretch	c		16.7558707472
					16.7558707472
					0.0000000000
NH^+	3172.63	stretch	c		15.8267003757
					15.8267003757
					0.0000000000
NSi	1492.20	stretch		c	0.7695107581
					0.7695107581
					0.0000000000
NSi^+	1242.74	stretch		c	0.6593778300
					0.6593778300
					0.0000000000

[1] In units of cm^{-1}.

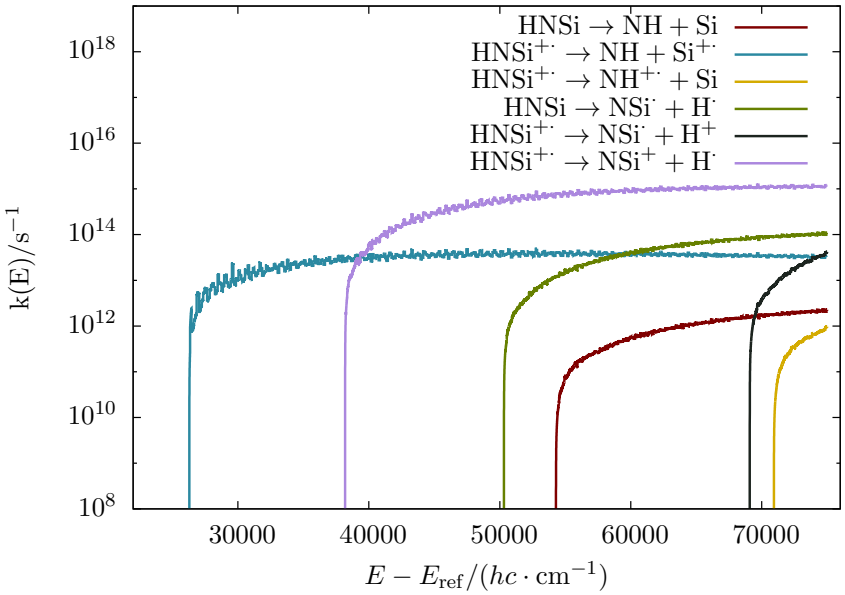

Figure 3.9: Dissociation rates of neutral and cationic HNSi as a function of energy. The reference energy corresponds to the vibrationless states of HNSi or $HNSi^{+\cdot}$ respectively. The dissociation channels open at $54287\,cm^{-1}$ for reaction 3.31, $26288\,cm^{-1}$ for reaction 3.32, $70930\,cm^{-1}$ for reaction 3.33, $50316\,cm^{-1}$ for reaction 3.34, $69090\,cm^{-1}$ for reaction 3.35 and $38188\,cm^{-1}$ for reaction 3.36.

3.2 Population distributions for Laser cooling

The processes during laser cooling are similar to those in NRMS. A molecule is vibronically excited and subsequently changes back into the initial electronic state. Unlike in NRMS the vibronic transition is not initiated by collisions, but by excitation with a laser with a specific frequency or by spontaneous emission. As a consequence not all theoretically possible transitions occur during laser cooling, but only those that have the right transition energy which equals the laser frequency. Furthermore, the cooling effect is only achieved after many transition cycles. A descriptive method needs to be very accurate to avoid a large accumulated error.

I extended my derivations for vibrational population distributions in NRMS in order to include specific laser frequencies and developed a method to increase the accuracy of the resulting populations.

There are three different kinds of transition situations involved, when simulating a laser cooling experiment:

1. Excitation with laser from a Boltzmann distributed population
2. Spontaneous relaxation
3. Excitation with laser from the population distribution calculated in the preceding steps.

The first transition is performed only once at the beginning of the laser cooling experiment. The second and third type are then alternately repeated. The spontaneous relaxation can be calculated in the same way as it was derived for the second transition step of the NRMS. The theory for the other two transition steps will be developed in the following sections.

3.2.1 Assumptions

As for the NRMS I assume for the laser cooling that in between the transitions the energy is redistributed among the degenerate states. Typical intramolecular vibrational redistribution time-scales are in the sub-picosecond ($10^{-13} - 10^{-12}$ s) region for molecules like benzene or larger. [85] Spontaneous emission as the competing process occurs on longer time-scales: Fluorescence time-scales are in the order of $10^{-9} - 10^{-7}$ s, phosphorescence is even slower with time-scales of $10^{-6} - 10^{-3}$ s. In the case of small molecules the occurrence of intramolecular vibrational redistribution is questionable. As Kim et al. showed in Ref. [86] only molecules with a rovibrational density of states larger than 70 $\frac{1}{\mathrm{cm}^{-1}}$ randomized their internal energy in an infrared fluorescence study.

The rate of the spontaneous emission is proportional to the third power of the emission frequency. This leads to a shift of the population distribution which

becomes more important the larger the width of the distribution in the excited state is. I do not account for such effects.

In case the density matrix has off-diagonal elements that are nonzero, this implies coherence effects between different states. I assume a density matrix with all off-diagonal elements being zero, because otherwise I would have to consider the phases between states.

Further, I assume FC transitions and a sharp frequency for the laser. In reality a laser has a certain bandwidth which can be quite large for ultra short laser pulses. He and Pollak for example use an average laser frequency and a frequency width in Ref. [87].

3.2.2 Population distribution as a function of laser frequency

The ansatz for the calculation of the vibrational population distribution in the excited state as a function of the laser frequency is

$$P'_{\mathrm{FCW}}(\hbar\omega', \hbar\omega_L) = \mathcal{N} \sum_{\underline{v},\underline{v}'=\underline{0}}^{\infty} \left|\langle \underline{v}'|\underline{v}\rangle\right|^2 \delta(\hbar(\omega' - (\omega_0 + \omega_{\underline{v}'})))\delta(\hbar(\omega_L - \overline{\omega}))\mathrm{e}^{-(\underline{v}'^t \boldsymbol{B}' \underline{\epsilon}' + \underline{v}^t \boldsymbol{B} \underline{\epsilon})} \tag{3.38}$$

where the variables are defined as in the former sections. The additional delta distribution $\delta(\hbar(\omega_L - \overline{\omega}))$ selects all transitions where the transition angular frequency $\overline{\omega}$ as defined in equation (2.67) corresponds to the angular frequency of the laser ω_L. In the time-dependent formulation the Dirac delta distributions are replaced by their Fourier transforms.

$$\begin{aligned} P'_{\mathrm{FC}}(\hbar\omega', \hbar\omega_L) =& \mathcal{N} \frac{1}{\hbar^2} \int_{-\infty}^{\infty} \mathrm{d}t' \int_{-\infty}^{\infty} \mathrm{d}t_L \sum_{\underline{v},\underline{v}'=\underline{0}}^{\infty} \left|\langle \underline{v}'|\underline{v}\rangle\right|^2 \mathrm{e}^{\mathrm{i}(\omega' - \omega_0 - \frac{\underline{\epsilon}'\cdot\underline{v}'}{\hbar})t'} \mathrm{e}^{\mathrm{i}(\omega_L - \omega_0 + \frac{\underline{\epsilon}\cdot\underline{v}}{\hbar} - \frac{\underline{\epsilon}'\cdot\underline{v}'}{\hbar})t_L} \\ =& \mathcal{N} \frac{1}{\hbar^2} \int_{-\infty}^{\infty} \mathrm{d}t' \int_{-\infty}^{\infty} \mathrm{d}t_L \sum_{\underline{v},\underline{v}'=\underline{0}}^{\infty} \left|\langle \underline{v}'|\underline{v}\rangle\right|^2 \mathrm{e}^{-\mathrm{i}\frac{\underline{\epsilon}'\cdot\underline{v}'}{\hbar}t'} \mathrm{e}^{\mathrm{i}\frac{\underline{\epsilon}\cdot\underline{v}}{\hbar}t_L} \mathrm{e}^{-\mathrm{i}\frac{\underline{\epsilon}'\cdot\underline{v}'}{\hbar}t_L} \\ & \mathrm{e}^{\mathrm{i}(\omega - \omega_0)t'} \mathrm{e}^{\mathrm{i}(\omega_L - \omega_0)t_L} \mathrm{e}^{-(\underline{v}'^t \boldsymbol{B}' \underline{\epsilon}' + \underline{v}^t \boldsymbol{B} \underline{\epsilon})} \end{aligned} \tag{3.39}$$

This leads to the generating function in the same way as described before. In the occupancy representation form of the coherent states this is

$$G'(\boldsymbol{Z}(t',t_L);\boldsymbol{\Lambda}) = \sum_{\underline{v},\underline{v'}=\underline{0}}^{\underline{\infty}} q(\underline{v'};\underline{v}) \prod_{k=1}^{N}\left[\left(z'_k(t',t_L)\right)^{2v'_k}\left(z_k(t_L)\right)^{2v_k}\right] \mathrm{e}^{-(\underline{v'}^t\boldsymbol{B'}\underline{\epsilon'}+\underline{v}^t\boldsymbol{B}\underline{\epsilon})} \tag{3.40}$$

and in the spatial representation form

$$G'(\boldsymbol{Z}(t',t_L);\boldsymbol{\Lambda}) = \det(\boldsymbol{I}-\boldsymbol{Z}\boldsymbol{W}_T\boldsymbol{Z})^{-\frac{1}{2}}\det(\boldsymbol{I}+\boldsymbol{Z}\boldsymbol{W}_T\boldsymbol{Z})^{-\frac{1}{2}}\exp(\underline{r}_T{}^t\boldsymbol{Z}(\boldsymbol{I}+\boldsymbol{Z}\boldsymbol{W}_T\boldsymbol{Z})^{-1}\boldsymbol{Z}\underline{r}_T) \tag{3.41}$$

with $\boldsymbol{Z}$ being defined as

$$\boldsymbol{Z} = \mathrm{diag}(z_1, z_2, \ldots, z_N, z'_1, z'_2, \ldots, z'_N) \tag{3.42}$$

$$z_k = \exp\left(\mathrm{i}\frac{\epsilon_k}{2\hbar}t_L\right) \tag{3.43}$$

$$z'_k = \exp\left(-\mathrm{i}\frac{\epsilon'_k}{2\hbar}t'\right)\exp\left(-\mathrm{i}\frac{\epsilon'_k}{2\hbar}t_L\right) \tag{3.44}$$

The selection by the laser requires the generating function to evolve through a second time dimension. We can then write the population distribution as

$$P'_{\mathrm{FC}}(\hbar\omega',\hbar\omega_L) = \mathcal{N}\frac{1}{\hbar^2}\left|\langle\underline{0'}|\underline{0}\rangle\right|^2\int_{-\infty}^{\infty}\mathrm{d}t'\int_{-\infty}^{\infty}\mathrm{d}t_L\, G'(\boldsymbol{Z}(t',t_L);\boldsymbol{\Lambda})\exp(\mathrm{i}(\omega_L-\omega_0)t_L)\exp(\mathrm{i}(\omega'-\omega_0)t') \tag{3.45}$$

3.2.3 Population distribution as a function of laser frequency with an initial non-Boltzmann population distribution

For the excitation with the laser from a calculated population distribution, as it is the case for the first excitation in the second and all following transition cycles, one can make an ansatz similar to the ansatz for the transition to the final state in NRMS. Here, we need to include an additional delta distribution for the laser frequency and we resign from using different symbols for the initial and final state

of a transition cycle as they are always identical.

$$P(\omega,\omega',\omega_L) = \mathcal{N}\sum_{\underline{v'},\underline{v}=\underline{0}}^{\infty}\frac{1}{\rho(\omega_{\underline{v'}})}P'(\omega_{\underline{v'}})\,|\langle\underline{v}|\underline{v'}\rangle|^2 \\ \delta(\hbar(\omega-(\omega_0'+\omega_{\underline{v}})))\delta(\hbar(\omega'-(\omega_0+\omega'_{\underline{v'}})))\delta(\hbar(\omega_L-\overline{\omega})) \tag{3.46}$$

$P'(\omega')$ is the population, that was calculated in the last step. We define some generating function $G'(\boldsymbol{Z}(t))$ for this population. The population $P(\omega,\omega',\omega_L)$ is then calculated as

$$P(\omega,\omega',\omega_L) = \frac{\mathcal{N}\mathcal{N}'}{\rho(\omega')}\frac{1}{\hbar^3}\,|\langle\underline{0'}|\underline{0}\rangle|^4\int_{-\infty}^{\infty}\mathrm{d}t\,G'(\boldsymbol{Z}(t))\exp(\mathrm{i}(\omega'-\omega_0)t) \\ \int_{-\infty}^{\infty}\mathrm{d}t\int_{-\infty}^{\infty}\mathrm{d}t'\int_{-\infty}^{\infty}\mathrm{d}t_L\,G(\boldsymbol{Z}(t,t',t_L)) \\ \exp(\mathrm{i}(\omega_L-\omega_0)t_L)\exp(\mathrm{i}(\omega-\omega_0')t')\exp(\mathrm{i}(\omega'-\omega_0)t) \tag{3.47}$$

with

$$G(\boldsymbol{Z}(t,t',t_L)) = \sum_{\underline{v'},\underline{v}=\underline{0}}^{\infty}\frac{|\langle\underline{v'}|\underline{v}\rangle|^2}{|\langle\underline{0'}|\underline{0}\rangle|^2} \\ \prod_{k=1}^{N}\left[(z_k'\exp(-\mathrm{i}\frac{\epsilon_k'}{2\hbar}t)\exp(\mathrm{i}\frac{\epsilon_k'}{2\hbar}t_L))^{2v_k'}(z_k\exp(-\mathrm{i}\frac{\epsilon_k}{2\hbar}t')\exp(-\mathrm{i}\frac{\epsilon_k}{2\hbar}t_L))^{2v_k}\right] \tag{3.48}$$

or the corresponding spatial representation. In this derivation I did not include the Boltzmann distribution as the initial state population distribution is calculated from the previous step. In practice the inclusion of a Boltzmann distribution with high temperature is necessary. The chosen temperature has no physical meaning, but is determined by the width of the population distribution. For more details I refer the reader to the section 3.1.4.

3.2.4 Practical realization

The following steps are to be performed, when calculating laser cooling cycles in practice.

First excitation with the laser

- As a first step the generating function $G'(\boldsymbol{Z}(t',t_L))$ has to be calculated as written in equation 3.41. The dimension of the generating function is $N\times N$ where N is the number of time steps calculated for one time dimension.

- Then the N Fourier transformations over t_L are performed.

$$G'(t', \omega_L) = \int_{-\infty}^{\infty} \mathrm{d}t_L \, G'(\boldsymbol{Z}(t', t_L)) \exp(\mathrm{i}(\omega_L - \omega_0)t_L) \tag{3.49}$$

- The trajectory $T1(t')$ for the specific laser frequency is selected from $G'(t', \omega_L)$. Therefore, the trajectory has got the dimension $N \times 1$. The index 1 is not written as a subscript to distinguish the trajectory from a temperature given as T_1. At this point it should be possible to introduce a line shape for the laser, if that is wanted.

Relaxation from the excited state

- The generating function $G(\boldsymbol{Z}(t, t'))$ from equation (3.17) is calculated. Its dimension is $N \times N$.

- Now G is convolved with $T1$.

$$\tilde{G}(\boldsymbol{Z}(t, t')) = G(\boldsymbol{Z}(t, t')) * T1(t') \tag{3.50}$$

  The convolution is performed as described in section 3.1.4

- The N Fourier transformations over t' are performed.

$$G(t, \omega') = \int_{-\infty}^{\infty} \mathrm{d}t' \, \tilde{G}(\boldsymbol{Z}(t, t')) \exp(\mathrm{i}(\omega' - \omega_0)t') \tag{3.51}$$

- The different trajectories are weighted with the degeneracy factor of the vibrational states in the excited state and then summed up.

$$T2(t)_{T_i} = \sum_{\omega'} \rho(\omega') G(t, \omega') \tag{3.52}$$

Extrapolation

When I calculated population distributions for different test systems it became obvious, that the approximation of an additional Boltzmann distribution with high temperature in the generating function (Compare to section 3.1.4.) would work for the single cycle of the NRMS experiment, but the results would still accumulate an error after multiple transition cycles.

I developed a simple routine in order to extrapolate the population distribution from calculations with two different temperatures in the Boltzmann distribution.

The method is as follows: Two numerical calculations of the population distribution are performed, for example at 500 K and at 2000 K. All values are obtained on an equally spaced grid. The extrapolated population distribution is then calculated as

$$D_i = \frac{B_i - A_i}{\sum\limits_j B_j - A_j} \left(\sum_j C_j - \sum_j B_j \right) + B_i \tag{3.53}$$

where the discrete population distribution calculated at 500 K is the sequence $(A_1, A_2, \ldots)$, the population calculated at 2000 K is the sequence $(B_1, B_2, \ldots)$ and the extrapolated population is the sequence $(D_1, D_2, \ldots)$. The points C_i are part of the sequence of the population in the intermediate state, i.e. the sum over all C_i is the total population before this transition. The population is not renormalized after selection of the laser frequency and the total population can differ from 1. Ideally the term in brackets should be zero, as we do not loose population in the relaxation step. In practice the Boltzmann distribution for 2000 K introduces an error, that we need to correct.

In equation (3.53) the value B_i in the sequence B is corrected by the ratio the population at point i is changed, when changing the temperature ($\frac{B_i - A_i}{\sum_j B_j - A_j}$), times the total population error of the sequence B ($\sum_j C_j - \sum_j B_j$). The next steps are therefore

- The trajectory $T1(t')$ is Fourier transformed and all populations are add up. This gives the total transferred population $P1_{\text{tot}}$ corresponding to $\sum\limits_j C_j$.
- The trajectory $T2(t)_{T_1}$ is Fourier transformed and one gets $P2(\omega)_{T_1}$ corresponding to A.
- The last transition is again calculated at another temperature and the resulting $T2(t)_{T_2}$ is Fourier transformed to get $P2(\omega)_{T_2}$ corresponding to B.
- The extrapolated population $P2(\omega)$ corresponding to D is calculated as in equation 3.53.
- $P2(\omega)$ is Fourier transformed to get $T2(t)$.

Second excitation with the laser

- The last generating function is calculated as in equation 3.48. $G'(\boldsymbol{Z}(t, t', t_L))$ has the dimension $N \times N \times N$.

- Next the $4N^2$ Fourier transformations over t_L are performed.

$$G'(t,t',\omega_L) = \int_{-\infty}^{\infty} \mathrm{d}t_L \, G'(\boldsymbol{Z}(t,t',t_L)) \exp(\mathrm{i}(\omega_L - \omega_0)t_L) \tag{3.54}$$

- Again only the part needed for the specific laser frequency is picked out. The resulting generating function $G'(t,t')$ has the dimensions $N \times N$.

- The generating function is convoluted with $T2(t)$.

$$\tilde{G}'(t,t') = G'(t,t') * T2(t) \tag{3.55}$$

- The N Fourier transformations over t are performed.

$$G'(\omega,t') = \int_{-\infty}^{\infty} \mathrm{d}t \, \tilde{G}'(t,t') \exp(\mathrm{i}(\omega - \omega_0)t) \tag{3.56}$$

- The different trajectories are weighted with the degeneracy factor of the vibrational states in the ground state and then summed up.

$$T3(t') = \sum_{\omega} \rho(\omega) G'(\omega,t') \tag{3.57}$$

This excitation step suffers from the same accuracy problem as the relaxation step. Unfortunately, the extrapolation method described above is not directly applicable. The reason is that the correct total population after this step is not known a priory. For now it remains an open question now to alleviate this problem.

Further transitions

The next transitions are repetitions of the relaxation and the second excitation. The steps with gray background color do not need to be performed again. The final population distribution in the ground state is then obtained by Fourier transform of Ti, where i is an even number.

3.2.5 One-dimensional model system

I performed one cycle in the laser cooling for a one dimensional system in order to illustrate the principle eventhough for auch a small system the time-independent approach is more efficient. The input parameters are listed in table 3.6. I used the computer algebra system Mathematica. [88]

Table 3.6: Parameters for the one-dimensional model system used in the calculation of vibrational population distributions for laser cooling. The laser was tuned to the $0 - 0'$-transition.

Parameter	Value
$\epsilon/(hc \cdot \mathrm{cm}^{-1})$	20
$\epsilon'/(hc \cdot \mathrm{cm}^{-1})$	60
S	1.0
δ	1.0
$\omega_0/(2\pi c \cdot \mathrm{cm}^{-1})$	0[1]
Temperature/K	0
Upper Limit/$(hc \cdot \mathrm{cm}^{-1})$	3000
Graining $\Delta/(hc \cdot \mathrm{cm}^{-1})$	10
Number of sample points N	1024
Time steps	$(c \cdot 10^{-10}\Delta \cdot 2N)^{-1}$

[1]arbitrary value which only influences the shift of the energy axis

Figure 3.10 shows the vibrational population of the one dimensional test system after one laser cooling cycle, which corresponds to excitation with the laser and relaxation. The population after the second transition was extrapolated from calculations at pseudo temperatures of 500 K and 2000 K. The extrapolated result is in good numerical agreement with the result from the direct counting algorithm by Berger and Klessinger for the calculation of vibronic spectra [14]. The main fraction of the population was shifted from the lowest vibrational state to the third excited vibrational state. This shows that the test system is not suited for laser cooling as the population would leak out during sequential laser cooling cycles, but it illustrates the working principle very well.

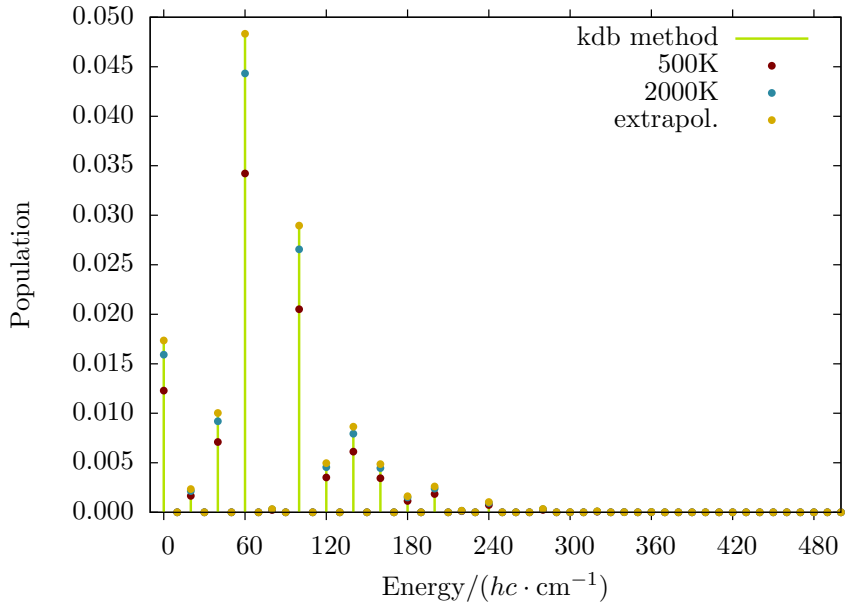

Figure 3.10: Vibrational population distribution for a one-dimensional system after one laser cooling cycle. I show the result from the KDB algorithm as reference, the intensities for the calculations at 500 K, 2000 K and the extrapolated result are indicated as points.

3.3 Theoretical aspects of the COLTRIMS experiment

In the COLTRIMS experiment a cooled molecular beam is crossed with a photon beam which induces vibronic transitions. In COLTRIMS as in NRMS the vibronic transitions occur with the ionisation of the molecule. The induced dissociation reactions can be described with the help of statistical theories. Even though the experiments are closely connected, my work has lead me away from vibrational population distributions in this part. I investigated very different aspects of the experiment and the molecular systems: isotopic effects, kinetic energy release (KER) distributions, multiply charged ions and fragmentation pathways. I will describe my results in the next sections.

3.3.1 Statistical evaluation of COLTRIMS experiments

The detector in COLTRIMS is time- and position-sensitive. From this information and the distance of the ionisation zone from the detector one can calculate the momenta of all ionic fragments after a Coulomb explosion. Under the assumption that the linear momenta resemble the geometrical structure of the initial molecule one can from the momenta determine the absolute configuration of the molecule.

In this section I refer to specific data that were obtained in an experiment on CHBrClF by Pitzer et al. at the Soleil synchrotron in France. [89]

The absolute configuration of the molecule is deduced from the triple product of three linear momentum vectors. This corresponds to the cosine of the angle between one of the vectors and the cross product of the other two vectors, when weighted by the norms as given here:

$$\cos(\theta) = \frac{\underline{p}_1 \cdot (\underline{p}_2 \times \underline{p}_3)}{|\underline{p}_1||\underline{p}_2 \times \underline{p}_3|} \tag{3.58}$$

The value of the cosine ranges from -1 to 1 and a value close to -1 would be assigned to one enantiomer and a value close to 1 to the other. If -1 indicates the R or S enantiomer has to be decided case by case for every new compound since no mathematical rule exists in order to link the linear momenta to their Cahn-Ingold-Prelog (CIP) priority. Figure 3.11 illustrates the situation for the two enantiomers.

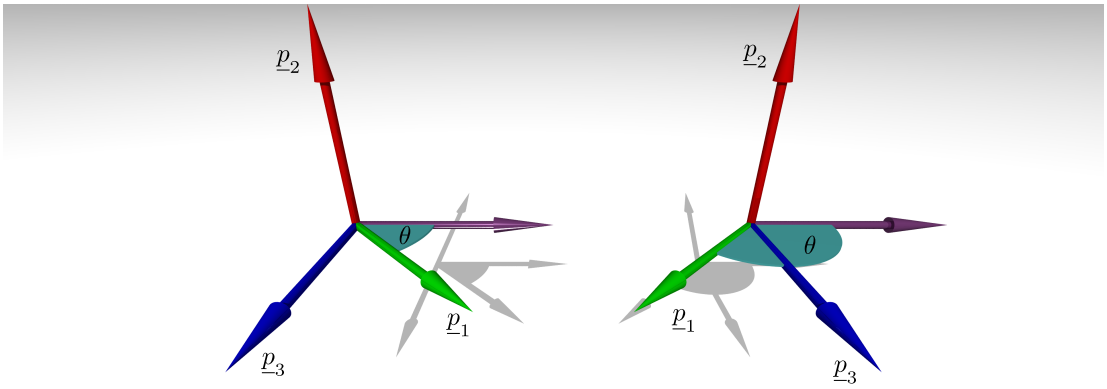

Figure 3.11: Determination of the cosine angle from the momentum vectors. The three vectors in green, red and blue correspond to $\underline{p}_1$, $\underline{p}_2$ and $\underline{p}_3$. The purple vector is the cross product $\underline{p}_2 \times \underline{p}_3$. In case the Cahn-Ingold-Prelog priority is decreasing from $\underline{p}_1$ to $\underline{p}_3$ the left arrangement corresponds to the S enantiomer and the right arrangement to the R enantiomer.

For the determination of linear momenta of detected particles the fragments have to be assigned charges and masses. As the natural isotope composition of CHBrClF contains H, D, ^{35}Cl, ^{37}Cl, ^{79}Br, ^{81}Br, ^{12}C and ^{13}C the momenta have to be calculated for different isotopic combinations. In case of five detected fragments we can assume that the resulting linear momenta should obey linear momentum conservation and therefore add up to zero as linear momenta of electrons and photons are negligible. In the case of only four detected fragments the linear momentum sum cannot be used to check the assignments of charges and masses. I

addressed the question how sure we could be that our final assignment of absolute configuration is correct.

The evaluation of the experimental data can lead to values of $\cos(\theta)$ close to 0 that might even change sign for different isotopic assignments. Furthermore, the cosine is determined from only three vectors, while the experiments provide up to five momentum vectors per event. The vectors used for the calculation of the cosine can be arbitrarily chosen, but might not all have the same accuracy. The ionisation can occur in a moment when the molecule is vibrationally distorted.

I investigated fragmentation pathways with four detected ions for their consistency in sign of the cosine and for the criterion $|\cos(\theta)| > 0.5$ when permuting the linear momentum vectors in the cosine calculation. I did not consider triple products with the momenta of both the hydrogen and carbon cation, since experiments showed that they are highly correlated and thus contain similar information. Table 3.7 lists the percentage of consistent events.

Table 3.7: Fraction of events with consistent sign for all triple products for fragmentation pathways with four detected ions. The total evaluated number of events are from top to bottom: 10846, 6057, 6183.

Fragments	consistent sign	consistent $\lvert\cos(\theta)\rvert > 0.5$
H^+ C^+ F^+ Cl^+	78,0%	38,2%
H^+ C^+ Cl^+ Br^+	76,6%	24,2%
H^+ F^+ Cl^+ Br^+	17,7%	11,4%

Furthermore, I looked at the consistency in sign when assuming different isotopic combinations. First, I calculated the cosine value with the most common isotopes (^{35}Cl,^{79} Br) and then tested if the sign changed when assigning the isotopic masses of ^{37}Cl and ^{81}Br respectively. Table 3.8 shows the percentage of consistent events when taking into account all measured events and with preselection of events that have a consistent sign for all seven possible triple products with the most common isotopic masses assigned.

The statistics show that the assignment of isotopes is not critical in over 90% of the cases where the most common isotopes provide consistent results. Also detection of only four instead of five fragments is usually not problematic. If the carbon cation is not detected though, the assignment of absolute configuration is more critical. The reason might be that dissociation pathways with neutral carbon have a higher ratio of sequential dissociation which causes the loss of information on the absolute configuration.

The data from the COLTRIMS experiment show another interesting feature. In the events with five detected particles all of these show a monomodal histogram of the KER distribution. In the events with four detected particles this is also

Table 3.8: Isotopic certainty of triple products.

Isotopes	consistent	consistent (with preselection)
H C F ^{35}Cl → H C F ^{37}Cl	89,2%	97,8%
H C ^{35}Cl ^{79}Br → H C ^{37}Cl ^{79}Br	84,9%	95,3%
H C ^{35}Cl ^{79}Br → H C ^{35}Cl ^{81}Br	88,6%	96,3%
H C ^{35}Cl ^{79}Br → H C ^{37}Cl ^{81}Br	78,0%	90,9%
H F ^{35}Cl ^{79}Br → H F ^{37}Cl ^{79}Br	87,4%	96,4%
H F ^{35}Cl ^{79}Br → H F ^{35}Cl ^{81}Br	90,7%	97,1%
H F ^{35}Cl ^{79}Br → H F ^{37}Cl ^{81}Br	83,1%	95,1%

true for all particles except for fluorine. Figure 3.12 shows the KERs for the four-particle events. I further inspected the momentum data and found that I could decompose the bimodal distribution into two monomodal distributions. To do so I counted all events for one distribution if the fluorine KER was smaller or equal to 500 $\frac{\hbar^2}{\mathrm{a_0^2 u}}$ and for the other if it was larger. I included only those events where fluorine was not detected, but its linear momentum was calculated by momentum conservation. Figure 3.13 shows the result.

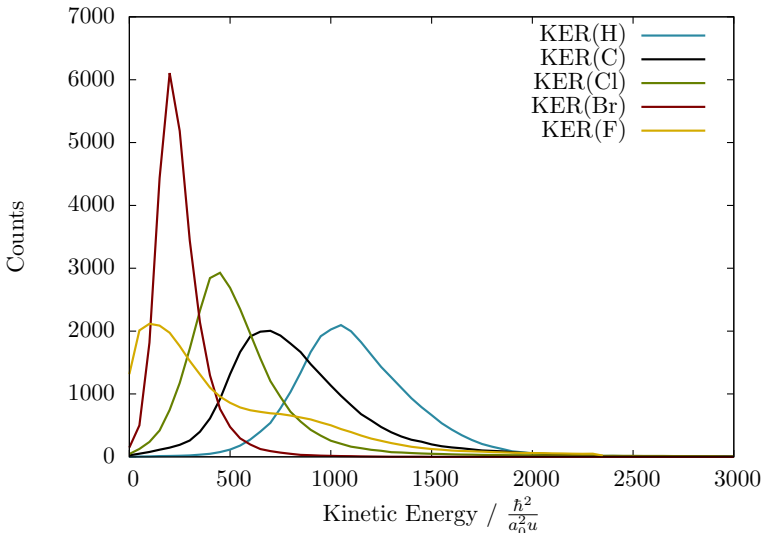

Figure 3.12: Kinetic energy release of detected particles in the events with four detected ions.

A possible explanation for the bimodal distribution was a retarded break up of the C–F bond. This diatomic fragment is relatively stable (Calculated dissociation barriers[1] for the elimination of the neutral atom from CHBrClF are 0.48 eV (Br),

[1]Geometry optimization with density functional theory (DFT) B3LYP/cc-pVTZ-F12, single

0.95 eV (Cl), 1.42 eV (H) and 1.96 eV (F).). I searched for other explanations and showed that the maximum at higher KER might indicate that some of the four-particle events are events with five charged fragments where one of the ions is simply not detected. Figure 3.14 shows the total KER of the events with four and five detected particles. The momenta of the missing particles in the four-particle events were deduced by momentum conservation. The maximum at higher KER appears at the same energy in both cases.

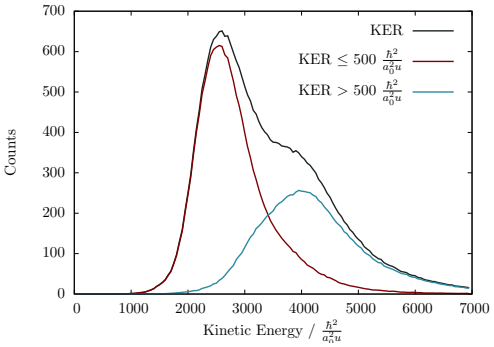

Figure 3.13: Kinetic energy release split into two monomodal distributions.

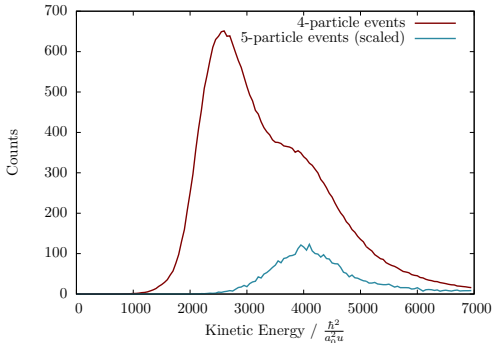

Figure 3.14: Total kinetic energy release for the events with four and five detected particles.

3.3.2 Multiply charged ion fragments of CHBrClF

The molecules in COLTRIMS are multiply ionized by a high energy photon beam. As discussed in reference [89] the beam excites an inner shell electron into the continuum. The system may undergo an Auger decay, knock-off, shake-off or direct photo emission. Then, the resulting ion explodes due to Coulombic repulsion. Intermediates which might be formed in between ionization and Coulomb explosion have a certain life time.

I investigated the structures of multiply charged CHBrClF for their stability and structure motifs. I will here present a summary of my results and refer the reader to the publication [91] for further information.

I optimized equilibrium structures for the singly charged up to the five-fold ionized molecule at the density functional level of theory using the B3LYP functional and the basis set cc-pVTZ-F12 for the C, H, Cl and F atoms. For bromine I used cc-pVTZ-PP-F12 [90] with a small-core Stuttgart-Cologne pseudopotential [92]. Afterwards, I calculated single point energies employing explicitly correlated coupled cluster (CCSD(T)-F12b) with the basis set described by Hill and Peterson [90].

I have found stable minima for $CHBrClF^{+\cdot}$, $CHBrClF^{2+}$ and $CHBrClF^{3+\cdot}$.

points with CCSD(T)-F12b/cc-pVTZ-F12 according to [90]

While the structure of the most stable isomer of the monocation is tetrahedral, the energetically lowest minimum found on the Born-Oppenheimer surfaces of the di- and trication correspond to C_S symmetric structures. Besides those minima I have found other planar structures for all three cationic specimen.

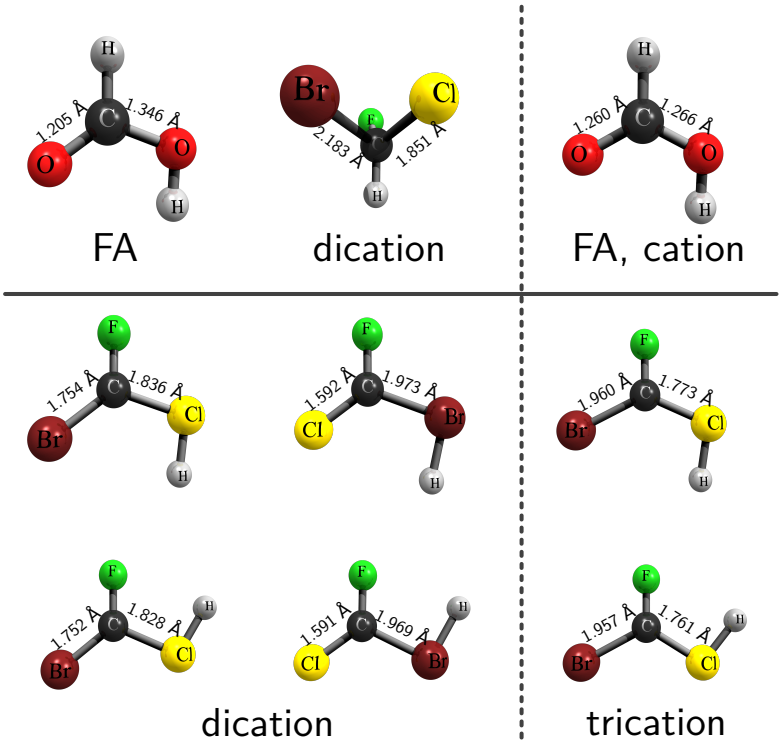

Figure 3.15: Illustration of the formic acid motif in di- and tricationic structures of CHBrClF.

Some of the dicationic structures resemble the structure of formic acid, whereas some of the structures of the trications are similar to the one of the monocation of the formic acid. Figure 3.15 shows the specific structures. Whereas the bond in the dications which mimicks the C–O double bond in formic acid is shortened compared to the corresponding bond in the tetrahedral structure, the bond mimicking the C–OH bond is approximately unchanged. The C–O double bond of the formic acid cation is elongated compared to the neutral molecule, the C–OH bond is shortened. A similar pattern can be observed for the threefold ionized structures of CHBrClF in comparison to the corresponding twofold ionized structures.

Planar structures might lead to loss of information about the absolute configuration of the precursor molecule. Therefore, I determined dissociation energies for the local minimum structures of $CHBrClF^{+\cdot}$, $CHBrClF^{2+}$ and $CHBrClF^{3+\cdot}$. I took three dissociation pathways into account: elimination of a single atom, elimination of an atomic ion and elimination of a diatomic fragment. I found that most

of the structures have small dissociation barriers or even negative dissociation energies. In those cases where the structures correspond to ion-dipole complexes the negative dissociation energies are an artifact of the method, namely the use of single point calculations on the CCSD(T)-F12b level instead of full structure energy minimizations. The minima at the DFT level need not correspond to minima at the coupled cluster level. Figures 3.16 to 3.18 show the relative energies without correction with vibrational zero point energies.

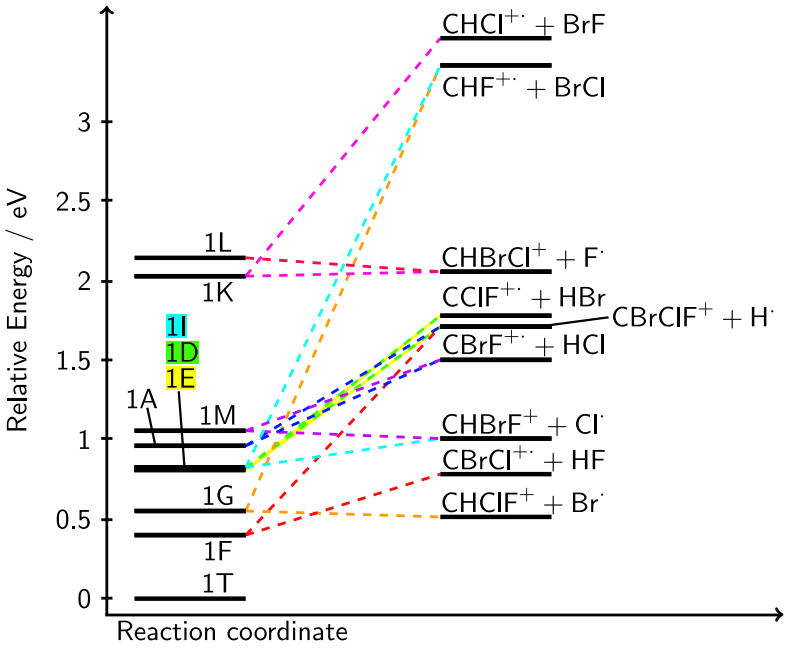

Figure 3.16: Selected dissociation pathways for the isomers of $CHBrClF^{+\cdot}$. Only the energies of the initial and the final structures are shown. The dashed lines serve as guidance for the eye.

The dissociation energies together with excess energies from vertical ionization suggest that the dissociation of $CHBrClF^{2+}$ follows rapidly after the ionization. I defined the excess energy as the energy difference between the vertically ionized structure and the relaxed structure. In the case of $CHBrClF^{+\cdot}$ the tetrahedral structure is the only isomer with an energy being below the energy of the vertically ionized structure. So planar species are very unlikely formed. The CCSD(T)-F12b calculation on the ground state of the trication of the vertically ionized structure did not converge so I checked for close lying electronic states. The trication in the doublet spin state has a low first electronic excitation energy of 0.23 eV which I calculated with time-dependent DFT. This indicates a multi-reference character of the wave function. I could thus not obtain the energy with the single reference method that I applied in the other cases. Energies from far more involved multi-reference methods would not be comparable. Therefore, I did not obtain an excess

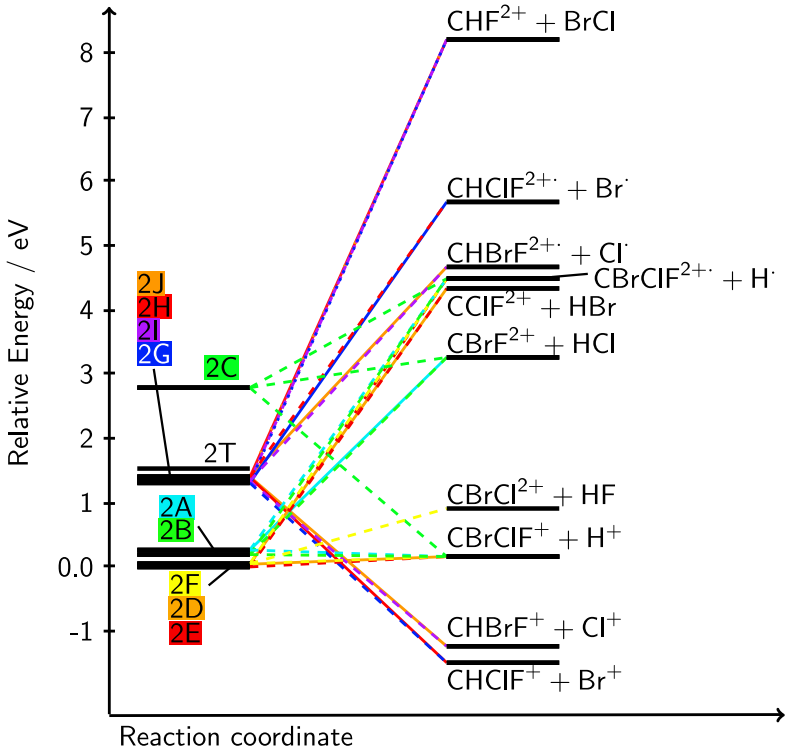

Figure 3.17: Selected dissociation pathways for the isomers of $CHBrClF^{2+}$. Only the energies of the initial and the final structures are shown. The dashed lines serve as guidance for the eye.

energy for $CHBrClF^{3+\cdot}$.

Furthermore, I searched for transition structures in order to understand the rearrangement of the tetrahedral structure to a planar isomer. I was able to find a transition structure between two planar isomers (2G and 2H), but not the desired transition structure.

The study was complemented by Born-Oppenheimer and classical molecular dynamics simulations of the COLTRIMS experiment by Sebastian Marquardt from the Philipps-Universität Marburg. Furthermore, we analyzed photoion photoion coincidence (PIPICO) spectra from laser and synchrotron experiments which where provided by Martin Pitzer from the Universität Kassel and Kilian Fehre from the Johann Wolfgang Goethe-Universität Frankfurt. We compared the experimental spectra to predicted signals and discussed the branching ratios of different dissociation channels with statistical rate theory.

In conclusion we could show that there are a lot of polycations of CHBrClF with achiral and chiral structures. Energy calculations and Born-Oppenheimer dynamics simulations showed that the inversion of the absolute configuration of the precursor molecule is unlikely which is of importance for the COLTRIMS

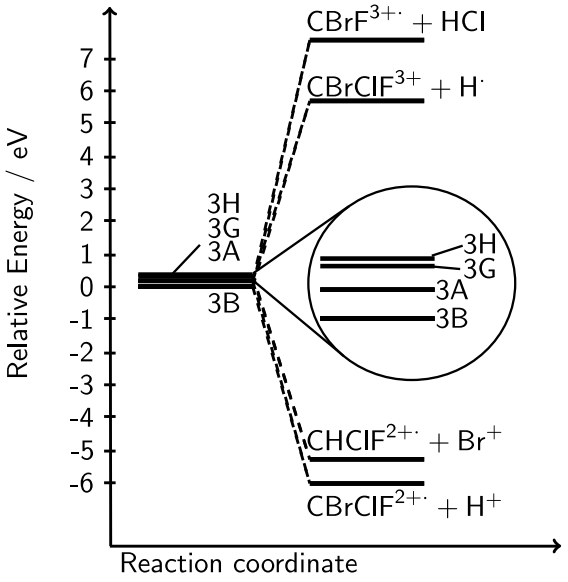

Figure 3.18: Selected dissociation pathways for the isomers of $CHBrClF^{3+\cdot}$. Only the energies of the initial and the final structures are shown. The dashed lines serve as guidance for the eye.

experiment. We established a theoretical tool box for the prediction of Coulomb explosion imaging signals, dominant fragmentation channels and branching ratios.

3.3.3 Reaction pathways for Cold Target Ion Momentum Spectroscopy

The molecule CHBrClF is a good candidate in order to determine the absolute configuration with COLTRIMS. Its small size with only one stereogenic center ensures that bond dissociations provide maximum information about the structure. Furthermore, polyhalo methane derivatives are expected to be suitable for experiments on parity violation. [49, 50] They have an intense infrared-active C–F stretching fundamental and can also be synthesized in necessary amounts. Compounds that contain heavy elements, like CDBrFI, show an even larger vibrational frequency splitting for the C–F stretching mode caused by parity violation than CHBrClF. Therefore, we investigated the fragmentations of the CDBrFI monocation.

I searched the Born-Oppenheimer PESs for stable structures of the neutral atom, cation and its fragments and calculated their appearance energies. For the structure energy minimizations and single point energies I used the same methods as described in the previous section. I treated iodine in the same way as the bromine. Additionally, I determined dissociation pathways including the transition states. Figures 3.19 to 3.21 show the energies of the key structures for different reaction pathways. Figure 3.21 is exemplary for the fragmentation of the other

tetra-atomic intermediates.

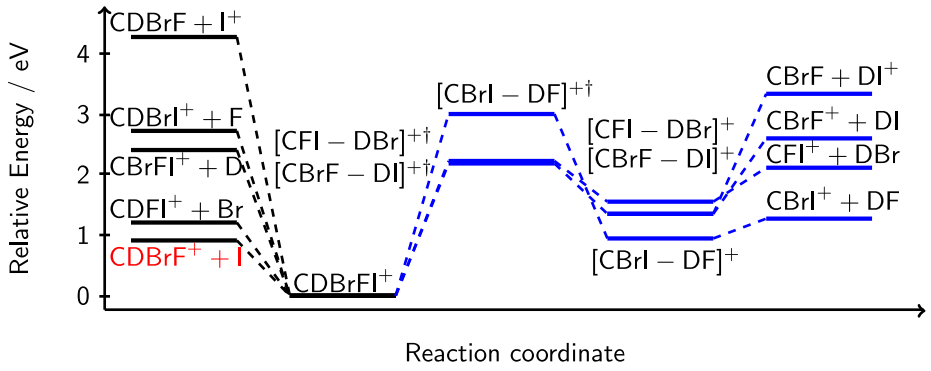

Figure 3.19: Fragmentation pathways of $CDBrFI^{+\cdot}$ with cleavage of one bond and cleavage of two bonds, where one of them is between C and D.

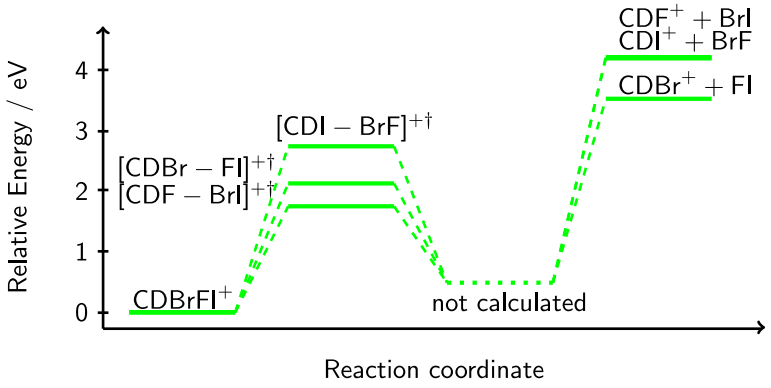

Figure 3.20: Fragmentation pathways of $CDBrFI^{+\cdot}$ with cleavage of two bonds, where none is the C–D bond. Intermediate states were not calculated as they had no relevance for the resulting appearance energies.

The eliminations of single atoms on the left side of figure 3.19 show the expected order, when the dissociation energy is correlated with the appearance energy of the CHX_2^+ compound in the gas phase ionization of CHX_3 where $X \in \{H, I, Br, F\}$ (CHI_2^+ 9.77 eV, $CHBr_2^+$ 10.53 eV, CH_3^+ 14.3 eV and CHF_2^+ 16.8 eV). [93, 94, 95] The fragmentation pathways for eliminations of DX fragments with $X \in \{I, Br, F\}$ are shown on the right side of figure 3.19. The order of experimental appearance energies $CBrF^{+\cdot} < CFI^{+\cdot} < CBrI^{+\cdot}$ is also found in the theoretical results as the appearance energy is determined by the highest barrier. The coupled cluster calculations showed that the elimination of DX is favorable over sequential elimination

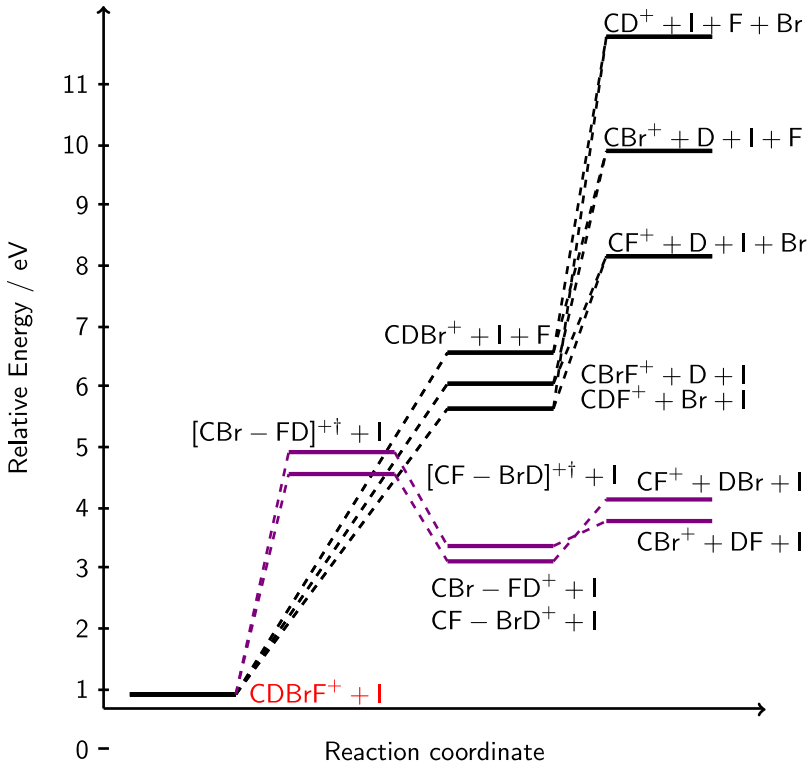

Figure 3.21: Fragmentation pathways of $CDBrF^+$ with cleavage of one bond and cleavage of two bonds, where one is between C and D.

of atomic fragments. The order of appearance energies resulting from elimination of XY species with $X \neq Y \wedge X, Y \in \{I, Br, F\}$ calculated on CCSD(T)-F12(b) level is shown in figure 3.20 and is not in agreement with the experiment. In the experiment the appearance energy of CDF^+ is the lowest. In figure 3.21 CF^+ shows the lowest barrier, which is in agreement with the experimental finding.

Table 3.9 lists the calculated appearance energies for the ionic species together with the experimental appearance energies. The mass spectrometry experiments were done by Alexander Schießer from the Technische Universität Darmstadt.

The theoretical and experimental values are in good agreement. The calculated appearance energies are expected to be a lower bound to the experimental values, which include kinetic shifts. This rule is not fulfilled for the generation of the $DI^{+\cdot}$ ion. Explanations can be that formation of $DI^{+\cdot}$ needs to be described on an excited PES, or neutral DI was existent in the probe. Table 3.10 lists ionization potentials of CDBrFI calculated with the outer valence Green's function method. Ionization from different orbitals is possible within an energy range of 4 eV. This

indicates that generation of fragments might be possible from higher electronic states. The ionization energy of neutral DI is 10.387 eV which is below the experimental appearance energy of 11.6 eV. [97] Taking into account the kinetic shift it is very possible that this process causes the low experimental appearance energy. The relative intensity of the ion as a function of the electron-impact energy shows two intervals with linear, but different slopes (see figure 3.22). I deduced that two competing processes form $DI^{+\cdot}$ ions. The first channel opens at about 12 eV and could correspond to the reaction $DI \rightarrow e^- + DI^{+\cdot}$. At about 16 eV the second channel opens and could be the result of the $CDBrFI^{+\cdot}$ decomposition. For $DBr^{+\cdot}$ the theoretical appearance energy is also above the experimental value, but lies within the error bars of the experiment.

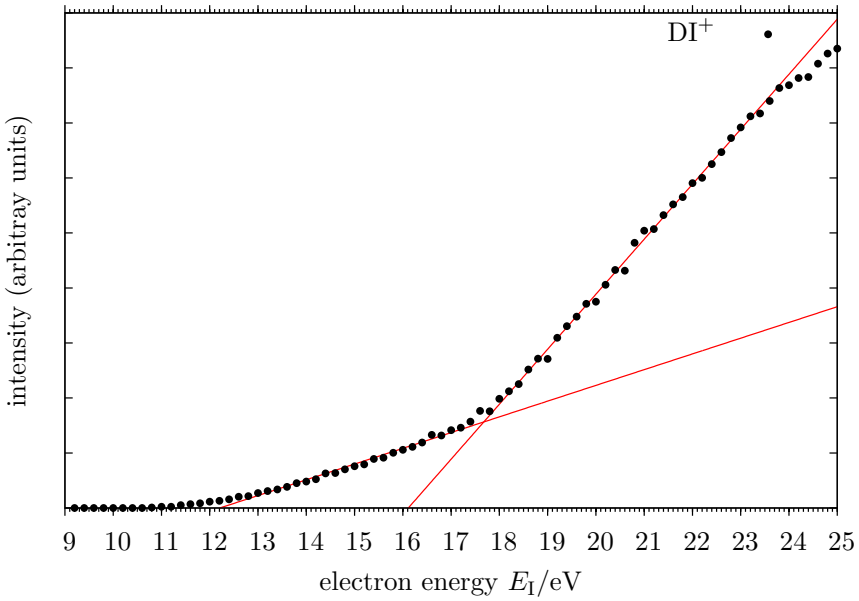

Figure 3.22: Intensity of the DI^+ ion as a function of the electron-impact energy. The red lines illustrate the sections with different slope.

The smaller differences between theoretical and experimental values can be explained by missing spin orbit coupling and higher level corrections. The spin orbit corrected appearance energies for $CDBrF^+$, $CDFI^+$ and $CDBrI^+$ show that the corrections improve the agreement between theory and experiment.

Table 3.9: Theoretical and experimental appearance energies for cationic fragments of $CDBrFI^{+\cdot}$. The errors for the experimental values are the statistical error (two standard deviations) and the estimated systematic error based on the method of analysis (slope of the ionization efficiency curves). The calculated appearance energies include zero point vibrational energy corrections. The harmonic vibrational frequencies were calculated on the hybrid density functional theory level. Values in parentheses include empirical spin orbit coupling corrections [96]. The second column indicates the investigated pathways.

obs. ion	stoichiometric equation	theoret. AE\IE /eV	exp. AE\IE /eV
$CDBrFI^{+\cdot}$	$CDBrFI = e^- + CDBrFI^+$	9.82	$9.8 \pm 0.02 \pm 0.06$ [1]
$CDBrF^+$	$CDBrFI = e^- + I^\cdot + CDBrF^+$	10.71 (10.39)	$10.6 \pm 0.03 \pm 0.12$ [1]
$CDFI^+$	$CDBrFI = e^- + Br^\cdot + CDFI^+$	10.99 (10.83)	$11.4 \pm 0.05 \pm 0.11$ [1]
$CDBrI^+$	$CDBrFI = e^- + F^\cdot + CDBrI^+$	12.44 (12.42)	$12.7 \pm 0.49 \pm 2.06$ [2]
$CBrFI^+$	$CDBrFI = e^- + D^\cdot + CBrFI^+$	12.01	$14.1 \pm 0.93 \pm 0.49$ [3]
I^+	$CDBrFI = e^- + CDBrF^\cdot + I^+$	14.03 (13.64)	$15.0 \pm 0.35 \pm 0.91$ [1]
Br^+	$CDBrFI = e^- + CDFI^\cdot + Br^+$	16.06 (15.87)	$19.4 \pm 0.57 \pm 1.38$ [1]
$CBrF^{+\cdot}$	$CDBrFI = e^- + DI + CBrF^{+\cdot}$	12.24	$13.8 \pm 0.32 \pm 0.86$ [3]
	$CDBrFI = e^- + D + I + CBrF^{+\cdot}$	15.59	
$CFI^{+\cdot}$	$CDBrFI = e^- + DBr + CFI^{+\cdot}$	11.88	$14.2 \pm 0.43 \pm 0.59$ [2]
	$CDBrFI = e^- + D^\cdot + Br^\cdot + CFI^{+\cdot}$	15.78	
$CBrI^{+\cdot}$	$CDBrFI = e^- + DF + CBrI^{+\cdot}$	12.66	$17.0 \pm 1.01 \pm 2.43$ [3]
	$CDBrFI = e^- + D^\cdot + F^\cdot + CBrI^{+\cdot}$	16.87	
$DI^{+\cdot}$	$CDBrFI = e^- + DI^{+\cdot} + CBrF$	12.95	$11.6 \pm 0.18 \pm 0.67$ [1]
$DBr^{+\cdot}$	$CDBrFI = e^- + DBr^{+\cdot} + CFI$	14.16	$13.6 \pm 0.37 \pm 1.31$ [3]
$CDF^{+\cdot}$	$CDBrFI = e^- + BrI + CDF^{+\cdot}$	13.90	$15.8 \pm 0.16 \pm 0.27$ [1]
	$CDBrFI = e^- + Br^\cdot + I^\cdot + CDF^{+\cdot}$	15.30	
$CDBr^{+\cdot}$	$CDBrFI = e^- + FI + CDBr^{+\cdot}$	13.18	$16.7 \pm 0.66 \pm 1.77$ [2]
	$CDBrFI = e^- + F^\cdot + I^\cdot + CDBr^{+\cdot}$	16.18	
$CDI^{+\cdot}$	$CDBrFI = e^- + BrF + CDI^{+\cdot}$	13.85	$18.0 \pm 0.51 \pm 0.81$ [1]
	$CDBrFI = e^- + F^\cdot + Br^\cdot + CDI^{+\cdot}$	16.54	
$BrI^{+\cdot}$	$CDBrFI = e^- + BrI^{+\cdot} + CDF$	14.00	$15.6 \pm 0.48 \pm 1.38$ [1]
$FI^{+\cdot}$	$CDBrFI = e^- + FI^{+\cdot} + CDBr$	14.91	
CF^+	$CDBrFI = e^- + D^\cdot + Br^\cdot + I^\cdot + CF^+$	17.65	
	$CDBrFI = e^- + Br^\cdot + DI + CF^+$	14.30	$14.6 \pm 0.13 \pm 0.05$ [1]
	$CDBrFI = e^- + I^\cdot + DBr + CF^+$	14.15	
CI^+	$CDBrFI = e^- + D^\cdot + Br^\cdot + F^\cdot + CI^+$	19.62	
	$CDBrFI = e^- + DBr + F^\cdot + CI^+$	15.85	$16.5 \pm 0.65 \pm 2.75$ [1]
	$CDBrFI = e^- + Br^\cdot + DF + CI^+$	14.78	
CBr^+	$CDBrFI = e^- + D^\cdot + I^\cdot + F^\cdot + CBr^+$	19.34	
	$CDBrFI = e^- + DI + F^\cdot + CBr^+$	15.99	$16.8 \pm 0.39 \pm 1.75$ [1]
	$CDBrFI = e^- + DF + I^\cdot + CBr^+$	14.53	

[1]Interpolation in the range 0.3% - 3 % (normalized to 50 eV).
[2]Interpolation in the range 1% - 10% (normalized to 50 eV).
[3]Interpolation in the range 3% - 20% (normalized to 50 eV).

Table 3.10: Ionization energies from outer valence Green's function calculations, experimental ionization energies and assignments to molecular orbitals.

OVGF (this work) / eV	ROVGF[1] / eV	experiment[1] / eV	Assignment[1]
10.11	9.82	9.86	non-binding I
10.32	10.01	10.49	non-binding I
10.99	10.80	11.02	non-binding Br
11.46	11.27	11.55	non-binding Br
12.74	12.73	12.83	σ(CH/Cl)
13.80	13.77	13.66	σ(CH/CBr)
16.98	16.95	16.80	non-binding F
17.31	17.27	16.80	non-binding F

[1]Data taken from Novak et al. [66].

Chapter 4

Conclusion and Outlook

4.1 Conclusions 87
4.2 Open questions 89

4.1 Conclusions

The described goal of this work was to contribute theoretical, especially quantum mechanical, approaches to the investigation of three gas phase experiments:

In the framework of NRMS I extended the time-dependent generating function ansatz by Huh [13], which is a big advantage over a time-independent algorithm that had been available, and derived equations for the calculation of vibrational population distributions after the neutralisation and reionisation transitions. For the reionisation it was necessary that I extended the dimensionality of the generating function in the sense that I calculated trajectories in two time dimensions. I avoided singularities in the trajectories by tracking the transitions on the Riemann surface of the complex square root function. Furthermore, I cut the infinite sums in the generating function with slowly decaying Boltzmann distributions. I also demonstrated a basis set expansion which uses a basis of exponential functions to represent a population distribution. However, this ansatz showed a much lower accuracy than the previously described. I showed that my equations result in the correct vibrational population distributions for a two-dimensional system by comparing it to the exact result from the time-independent method. Finally, I applied the new method to the molecular system HNSi and combined it with reaction rate calculations with the SACM. I was able to reproduce main features of the NRMS experiment in reference [81].

In the laser cooling experiment the transitions are induced by a laser with specific frequency. Therefore, I extended my equations for the calculation of population distributions and introduced a frequency selection. This lead to a further

increase in dimensionality of the generating function. For laser cooling experiments it is necessary to calculate a large number of cycles so that theoretical descriptions need to be highly accurate due to error accumulation. I developed a strategy in order to further increase the accuracy of my method. Since this was not applicable to all transitions, accuracy remains an issue in the description.

In the context of the determination of absolute configuration with COLTRIMS, I could show that the assignment of isotopic masses does not considerably influence the assignment of absolute configuration for the specific case of CHBrClF. It is reasonable to assume the most frequent isotopes. Evaluation of events with four detected particles give the right absolute configuration for the majority of the events, but events without a detected carbon ion should be handled with care. In these cases the result strongly depends on the selection of the linear momentum vectors for the calculation of the cosine. Furthermore, I analysed the KER in the four-particle events. I showed that the bimodal distribution of the KER of the fluorine ion indicates that some of the events are actual five-particle events with complete break up of the CHBrClF molecule where only four particles were detected. I took a closer look at the ionisation of CHBrClF by investigation of the singly and multiply charged cations. Using quantum chemical methods I found several local minimum structures for the mono-, di- and trication, some of those with planar geometries. As those can impose problems in the determination of the absolute configuration I calculated their dissociation energies and the vertical excess energy and showed that either formation of the planar isomers is unlikely or the metastable structure should have short life times. I also looked at the fragmentation pathways of CDBrFI which is expected to show larger parity violation effects than CHBrClF. I restricted this study to the break up of the monocation and compared the appearance energies of the ionic fragments to experimental values from a mass spectrometry experiment. The overall agreement was good. Discrepancies resulted from kinetic shifts and impurities on the experimental side and from missing spin orbit and higher order corrections on the theoretical side.

Finally I can state that I successfully extended the time-dependent generating function ansatz so that it was possible to calculate vibrational population distributions after vibronic transitions. The resulting concepts are highly versatile and can be applied to different molecules in different gas phase experiments, such as laser cooling, NRMS or photoelectron photoion coincidence spectroscopy. The development demanded fundamental insight into the theoretical concepts of vibronic structure theory, normal modes and the Duschinski relation, Fourier transformation and autocorrelation functions. The explanation for discontinuities in the trajectories of generating functions will be of interest beyond this work for other time-dependent descriptions of vibronic spectra. I applied analytic as well as quantum chemical methods to different topics related to the COLTRIMS experiment.

The answer of the related questions required physical understanding of the ionisation and Coulomb explosion processes, expertise in the computational methods and some creativity.

4.2 Open questions

The presented method for the calculation of vibrational population distributions after vibronic transitions is in principle applicable to all kinds of molecular systems. In practice, the approach shows limitations and includes approximations that could be lifted.

Calculations of population distributions become very time- and resource demanding for systems with large off-diagonal elements in the FC matrix. With the first transition the vibrational population is strongly shifted to higher energies. This requires a very broad Boltzmann distribution for the second transition and therefore a huge integration interval. Otherwise the inaccuracy increases significantly.

For the simulation of many laser cooling cycles the method is still too inaccurate. Also the step by step calculation of the population distributions would be a tedious task for ,e.g., 10 000 laser cooling cycles. It would be desirable to find a way to avoid repeated convolution and Fourier transformation steps and extrapolate the result directly after calculation of a single cycle.

The method does not include anharmonic effects and is from this point of view not able to describe dissociations of molecular systems. This approximation should be lifted in a comprehensive description of the NRMS experiment. The investigation of fragmentation processes can be extended with multi-fragmentation models as, e.g., the approach by Bondorf et al. [51].

Further questions remain in context of the COLTRIMS experiment: It is not yet clear if sequential fragmentation opposed to instantaneous Coulomb explosion prevents the assignment of absolute configuration. The final answer can probably only be given by an experiment on an enantiopure probe.

Appendices

Appendix A

Coherent states overlap

In this appendix I will show how to solve the overlap integral

$$\langle \beta'; t' | \alpha; t \rangle = \int_{-\infty}^{\infty} \hbar^{-\frac{1}{2}} \omega^{\frac{1}{4}} \omega'^{\frac{1}{4}} \pi^{-\frac{1}{2}} \mathrm{e}^{\frac{1}{2}\mathrm{i}(\omega' t' - \omega t)} \mathrm{e}^{-\frac{1}{2\hbar}(\omega' Q'^2 + \omega Q^2)} \mathrm{e}^{-\frac{1}{2}(|\alpha|^2 + |\beta'|^2)} \mathrm{e}^{\sqrt{\frac{2}{\hbar}}(\sqrt{\omega'} Q' \beta'^* \mathrm{e}^{\mathrm{i}\omega' t'} + \sqrt{\omega} Q \alpha \mathrm{e}^{-\mathrm{i}\omega t})} \mathrm{e}^{-\frac{1}{2}((\beta'^*)^2 \mathrm{e}^{2\mathrm{i}\omega' t'} + \alpha^2 \mathrm{e}^{-2\mathrm{i}\omega t})} \, \mathrm{d}Q \tag{A.1}$$

When we rewrite Q' as $SQ + d$ the integral has the form

$$\int_{-\infty}^{\infty} f \mathrm{e}^{aQ^2 + bQ + c} \, \mathrm{d}Q = \frac{\sqrt{\pi} f}{\sqrt{-a}} \mathrm{e}^{-\frac{b^2}{4a} + c} \tag{A.2}$$

The parameters a, b and c are as follows

$$a = -\frac{1}{2\hbar}(\omega' S^2 + \omega) \tag{A.3}$$

$$b = -\frac{1}{\hbar}(\omega' S d - \sqrt{2}\sqrt{\hbar}\sqrt{\omega'} S \beta'^* \mathrm{e}^{\mathrm{i}\omega' t'} - \sqrt{2}\sqrt{\hbar}\sqrt{\omega}\alpha \mathrm{e}^{-\mathrm{i}\omega t}) \tag{A.4}$$

$$c = \frac{1}{2}\mathrm{i}(\omega' t' - \omega t) - \frac{1}{2\hbar}\omega' d^2 - \frac{1}{2}(|\alpha|^2 + |\beta'|^2) + \sqrt{\frac{2}{\hbar}}\sqrt{\omega'} d \beta'^* \mathrm{e}^{\mathrm{i}\omega' t'} - \frac{1}{2}(\beta'^*)^2 \mathrm{e}^{2\mathrm{i}\omega' t'} - \frac{1}{2}\alpha^2 \mathrm{e}^{-2\mathrm{i}\omega t} \tag{A.5}$$

$$f = \frac{1}{\sqrt{\pi\hbar}} \omega^{\frac{1}{4}} \omega'^{\frac{1}{4}} \tag{A.6}$$

We can rewrite a using the definition $J = \sqrt{\omega'} S \frac{1}{\sqrt{\omega}}$

$$a = -\frac{1}{2\hbar}(\omega' S^2 \frac{1}{\omega} + 1)\omega \tag{A.7}$$

$$= -\frac{1}{2\hbar}(J^2 + 1)\frac{\sqrt{\omega'} S \sqrt{\omega}}{\sqrt{\omega'} S \frac{1}{\sqrt{\omega}}} \tag{A.8}$$

$$= -\frac{1}{2\hbar}\frac{J^2+1}{J}\sqrt{\omega'} S \sqrt{\omega} \tag{A.9}$$

For the factor in front of the exponential in equation (A.2) we then get

$$\frac{\sqrt{\pi} f}{\sqrt{-a}} = \frac{1}{\sqrt{S}}\frac{\sqrt{2}\sqrt{J}}{\sqrt{1+J^2}} \tag{A.10}$$

The exponential is

$$\begin{aligned} -\frac{b^2}{4a} + c =& \frac{J}{J^2+1}\left(\frac{1}{2\hbar}\omega'\sqrt{\omega'} S \frac{1}{\sqrt{\omega}} d^2 - \sqrt{2}\frac{1}{\sqrt{\hbar}}\omega' S \frac{1}{\sqrt{\omega}} d\beta'^* \mathrm{e}^{\mathrm{i}\omega' t'} - \sqrt{2}\frac{1}{\sqrt{\hbar}}\sqrt{\omega'} d\alpha \mathrm{e}^{-\mathrm{i}\omega t}\right. \\ &\left. + \sqrt{\omega'} S \frac{1}{\sqrt{\omega}}(\beta'^*)^2 \mathrm{e}^{2\mathrm{i}\omega' t'} + 2\alpha\beta'^* \mathrm{e}^{-\mathrm{i}\omega t}\mathrm{e}^{\mathrm{i}\omega' t'} + \frac{1}{\omega'}\frac{1}{S}\sqrt{\omega}\alpha^2 \mathrm{e}^{-2\mathrm{i}\omega t}\right) \\ &+ \frac{1}{2}\mathrm{i}(\omega' t' - \omega t) - \frac{1}{2\hbar}\omega' d^2 - \frac{1}{2}(|\alpha|^2 + |\beta'|^2) \\ &+ \sqrt{\frac{2}{\hbar}}\sqrt{\omega'} d\beta'^* \mathrm{e}^{\mathrm{i}\omega' t'} - \frac{1}{2}(\beta'^*)^2 \mathrm{e}^{2\mathrm{i}\omega' t'} - \frac{1}{2}\alpha^2 \mathrm{e}^{-2\mathrm{i}\omega t} \end{aligned} \tag{A.11}$$

We use the definitions for J and $\delta = \frac{1}{\sqrt{\hbar}}\sqrt{\omega'} d$ and then sort the terms for their order in δ. We get

$$\begin{aligned} -\frac{b^2}{4a} + c =& -\frac{1}{2}\delta^2 + \frac{1}{2}\frac{J^2}{J^2+1}\delta^2 \\ &- \sqrt{2}\frac{J^2}{J^2+1}\delta\beta'^* \mathrm{e}^{\mathrm{i}\omega' t'} - \sqrt{2}\frac{J}{J^2+1}\delta\alpha \mathrm{e}^{-\mathrm{i}\omega t} + \sqrt{2}\delta\beta'^* \mathrm{e}^{\mathrm{i}\omega' t'} \\ &+ \frac{J^2}{J^2+1}(\beta'^*)^2 \mathrm{e}^{2\mathrm{i}\omega' t'} + 2\frac{J}{J^2+1}\alpha\beta'^* \mathrm{e}^{-\mathrm{i}\omega t}\mathrm{e}^{\mathrm{i}\omega' t'} + \frac{1}{J^2+1}\alpha^2 \mathrm{e}^{-2\mathrm{i}\omega t} \\ &+ \frac{1}{2}\mathrm{i}(\omega' t' - \omega t) - \frac{1}{2}(|\alpha|^2 + |\beta'|^2) - \frac{1}{2}(\beta'^*)^2 \mathrm{e}^{2\mathrm{i}\omega' t'} - \frac{1}{2}\alpha^2 \mathrm{e}^{-2\mathrm{i}\omega t} \end{aligned} \tag{A.12}$$

We can now use the definitions $P = \frac{J^2}{1+J^2}$, $R = \frac{J}{1+J^2}$ and $Q = \frac{1}{1+J^2}$ and get

$$\begin{aligned}
-\frac{b^2}{4a} + c = &-\frac{1}{2}\delta(1-P)\delta \\
&\sqrt{2}(-P\delta\beta'^{*}\mathrm{e}^{\mathrm{i}\omega' t'} - R\delta\alpha\mathrm{e}^{-\mathrm{i}\omega t} + \delta\beta'^{*}\mathrm{e}^{\mathrm{i}\omega' t'}) \\
&-\frac{1}{2}(-2P(\beta'^{*})^2\mathrm{e}^{2\mathrm{i}\omega' t'} - 4R\alpha\beta'^{*}\mathrm{e}^{-\mathrm{i}\omega t}\mathrm{e}^{\mathrm{i}\omega' t'} - 2Q\alpha^2\mathrm{e}^{-2\mathrm{i}\omega t} + (\beta'^{*})^2\mathrm{e}^{2\mathrm{i}\omega' t'} + \alpha^2\mathrm{e}^{-2\mathrm{i}\omega t}) \\
&+\frac{1}{2}\mathrm{i}(\omega' t' - \omega t) - \frac{1}{2}(|\alpha|^2 + |\beta'|^2)
\end{aligned} \tag{A.13}$$

We can define the following matrices and vectors

$$\underline{\xi} = \begin{pmatrix} \alpha \\ \beta'^{*} \end{pmatrix} \tag{A.14}$$

$$\boldsymbol{W} = \begin{pmatrix} 1-2Q & -2R \\ -2R & 1-2P \end{pmatrix} \tag{A.15}$$

$$\underline{r} = \sqrt{2}\begin{pmatrix} -R\delta \\ (1-P)\delta \end{pmatrix} \tag{A.16}$$

$$\boldsymbol{Z} = \mathrm{diag}(\mathrm{e}^{-\mathrm{i}\omega t}, \mathrm{e}^{\mathrm{i}\omega' t'}) \tag{A.17}$$

and obtain for the exponential

$$\begin{aligned}
-\frac{b^2}{4a} + c = &-\frac{1}{2}\delta(1-P)\delta \\
&+\underline{r}^t\boldsymbol{Z}\underline{\xi} \\
&-\frac{1}{2}\underline{\xi}^t\boldsymbol{Z}\boldsymbol{W}\boldsymbol{Z}\underline{\xi} \\
&+\frac{1}{2}\mathrm{i}(\omega' t' - \omega t) - \frac{1}{2}\underline{\xi}^{\dagger}\underline{\xi}
\end{aligned} \tag{A.18}$$

Appendix B

Occupancy representation

This part is adapted from Doktorov et al. [77]. It illustrates how we obtained equation (2.75) from the ansatz of the generating function.

$$G(\boldsymbol{Z}) = \pi^{-2N} \left|\langle \underline{0}'|\underline{0}\rangle\right|^{-2} \int \mathrm{d}^2\underline{\alpha}\, \mathrm{d}^2\underline{\gamma}' \left\langle \boldsymbol{z}'^{*}\underline{\gamma}'|\boldsymbol{z}\underline{\alpha}\right\rangle \left\langle \boldsymbol{z}'\underline{\gamma}'|\boldsymbol{z}^{*}\underline{\alpha}\right\rangle^{*} \tag{B.1}$$

We rewrite the integral with the overlap integrals of the coherent states as given in equation (2.72)

$$\begin{aligned}
&\int \mathrm{d}^2\underline{\alpha}\, \mathrm{d}^2\underline{\gamma}' \left\langle \boldsymbol{z}'^{*}\underline{\gamma}'|\boldsymbol{z}\underline{\alpha}\right\rangle \left\langle \boldsymbol{z}'\underline{\gamma}'|\boldsymbol{z}^{*}\underline{\alpha}\right\rangle^{*} \\
&= \int \mathrm{d}^2\underline{\alpha}\, \mathrm{d}^2\underline{\gamma}' \sum_{\underline{u},\underline{u}'=\underline{0}}^{\infty} \sum_{\underline{v},\underline{v}'=\underline{0}}^{\infty} \langle \underline{u}'|\underline{u}\rangle \langle \underline{v}'|\underline{v}\rangle^{*} \\
&\prod_{k=1}^{N} \exp(-|\alpha_k|^2 - |\gamma'_k|^2) \frac{(z_k)^{u_k+v_k} (z'_k)^{u'_k+v'_k}}{\sqrt{u_k! v_k! u'_k! v'_k!}} \alpha_k^{u_k} (\alpha_k^{*})^{v_k} (\gamma'^{*}_k)^{u'_k} \gamma'^{v'_k}_k
\end{aligned} \tag{B.2}$$

We then write the complex α in polar form $\alpha = |\alpha| \exp(\mathrm{i}\phi_\alpha)$:

$$\begin{aligned}
&= \int_0^{\infty} \mathrm{d}|\underline{\alpha}| \int_0^{\infty} \mathrm{d}|\underline{\gamma}'| \int_0^{2\pi} \mathrm{d}\phi_\alpha \int_0^{2\pi} \mathrm{d}\phi_{\gamma'} \sum_{\underline{u},\underline{u}'=\underline{0}}^{\infty} \sum_{\underline{v},\underline{v}'=\underline{0}}^{\infty} \langle \underline{u}'|\underline{u}\rangle \langle \underline{v}'|\underline{v}\rangle^{*} \\
&\prod_{k=1}^{N} \exp(-|\alpha_k|^2 - |\gamma'_k|^2) (z_k)^{u_k+v_k} (z'_k)^{u'_k+v'_k} \\
&\frac{|\alpha_k|^{u_k+v_k+1} |\gamma'_k|^{u'_k+v'_k+1} \exp(\mathrm{i}\phi_{\alpha_k}(u_k - v_k)) \exp(-\mathrm{i}\phi_{\gamma'_k}(u'_k - v'_k))}{\sqrt{u_k! v_k! u'_k! v'_k!}}
\end{aligned} \tag{B.3}$$

We integrate the angular part $\frac{1}{2\pi}\int_0^{2\pi} d\phi \exp(\mathrm{i}\phi(m-n) = \delta_{mn}$:

$$
\begin{aligned}
=&2^N\pi^{2N}\int_0^\infty \mathrm{d}|\underline{\alpha}|\int_0^\infty \mathrm{d}|\underline{\gamma'}|\sum_{\underline{v},\underline{v'}=\underline{0}}^{\infty}|\langle\underline{v'}|\underline{v}\rangle|^2 \\
&\prod_{k=1}^{N}\exp(-|\alpha_k|^2-|\gamma'_k|^2)(z_k)^{2v_k}(z'_k)^{2v'_k}\frac{|\alpha_k|^{2v_k+1}|\gamma'_k|^{2v'_k+1}}{v_k!v'_k!}
\end{aligned}
\tag{B.4}
$$

We use $\int_0^\infty \mathrm{d}x\exp(-x^2)x^{2n+1} = \frac{1}{2}n!$:

$$
= \pi^{2N}\sum_{\underline{v},\underline{v'}=\underline{0}}^{\infty}|\langle\underline{v'}|\underline{v}\rangle|^2\prod_{k=1}^{N}(z_k)^{2v_k}(z'_k)^{2v'_k} \tag{B.5}
$$

$$
G(\boldsymbol{Z}) = \sum_{\underline{v},\underline{v'}=\underline{0}}^{\infty}\frac{|\langle\underline{v'}|\underline{v}\rangle|^2}{|\langle\underline{0'}|\underline{0}\rangle|^2}\prod_{k=1}^{N}(z_k)^{2v_k}(z'_k)^{2v'_k} \tag{B.6}
$$

Appendix C

Spatial representation

This part shows how we obtained equation (2.77) from the generating function ansatz. It is adapted from Jankowiak et al. [15].

$$G(\boldsymbol{Z}) = \pi^{-2N} \left|\langle \underline{0}'|\underline{0}\rangle\right|^{-2} \int \mathrm{d}^2\underline{\alpha}\, \mathrm{d}^2\underline{\gamma}' \left\langle \boldsymbol{z}'^{*}\underline{\gamma}'|\boldsymbol{z}\underline{\alpha}\right\rangle \left\langle \boldsymbol{z}'\underline{\gamma}'|\boldsymbol{z}^{*}\underline{\alpha}\right\rangle^{*} \tag{C.1}$$

We take the integral and set $\boldsymbol{Z} = \mathrm{diag}(\boldsymbol{z}, \boldsymbol{z}')$:

$$\begin{aligned}
&\int \mathrm{d}^2\underline{\alpha}\, \mathrm{d}^2\underline{\gamma}' \left\langle \boldsymbol{z}'^{*}\underline{\gamma}'|\boldsymbol{z}\underline{\alpha}\right\rangle \left\langle \boldsymbol{z}'\underline{\gamma}'|\boldsymbol{z}^{*}\underline{\alpha}\right\rangle^{*} \\
&= \int \mathrm{d}^2\underline{\alpha}\, \mathrm{d}^2\underline{\gamma}' \langle \underline{0}'|\underline{0}\rangle \exp(-\frac{1}{2}\left(\boldsymbol{Z}\underline{\xi}\right)^{\dagger} \boldsymbol{Z}\underline{\xi}) \exp(-\frac{1}{2}\left(\boldsymbol{Z}\underline{\xi}\right)^{t} \boldsymbol{W}\boldsymbol{Z}\underline{\xi} + \underline{r}^{t}\boldsymbol{Z}\underline{\xi}) \\
&\quad \langle \underline{0}'|\underline{0}\rangle^{*} \exp(-\frac{1}{2}\left(\boldsymbol{Z}^{*}\underline{\xi}\right)^{t} (\boldsymbol{Z}^{*}\underline{\xi})^{*}) \exp(-\frac{1}{2}\left(\boldsymbol{Z}^{*}\underline{\xi}\right)^{\dagger} \boldsymbol{W}(\boldsymbol{Z}^{*}\underline{\xi})^{*} + \underline{r}^{t}(\boldsymbol{Z}^{*}\underline{\xi})^{*}) \\
&= \int \mathrm{d}^2\underline{\alpha}\, \mathrm{d}^2\underline{\gamma}' \left|\langle \underline{0}'|\underline{0}\rangle\right|^{2} \exp(-\underline{\xi}^{\dagger}\underline{\xi}) \exp(-\frac{1}{2}\underline{\xi}^{t}\boldsymbol{Z}\boldsymbol{W}\boldsymbol{Z}\underline{\xi} - \frac{1}{2}\underline{\xi}^{\dagger}\boldsymbol{Z}\boldsymbol{W}\boldsymbol{Z}\underline{\xi}^{*} + \underline{r}^{t}\boldsymbol{Z}(\underline{\xi} + \underline{\xi}^{*}))
\end{aligned} \tag{C.2}$$

where we used that $\boldsymbol{Z}^{*}\boldsymbol{Z} = \boldsymbol{I}$, $\boldsymbol{W}^{*} = \boldsymbol{W}$ and $\underline{r}^{*} = \underline{r}$. We now substitute $\underline{\xi} = \underline{\xi}_R + \mathrm{i}\underline{\xi}_I$ and $\underline{\xi}^{*} = \underline{\xi}_R - \mathrm{i}\underline{\xi}_I$:

$$\begin{aligned}
-\underline{\xi}^{\dagger}\underline{\xi} &= -(\underline{\xi}^{*})^{t}\underline{\xi} \\
&= -(\underline{\xi}_R - \mathrm{i}\underline{\xi}_I)^{t}(\underline{\xi}_R + \mathrm{i}\underline{\xi}_I) \\
&= -\underline{\xi}_R^{t}\boldsymbol{I}\underline{\xi}_R - \underline{\xi}_I^{t}\boldsymbol{I}\underline{\xi}_I
\end{aligned} \tag{C.3}$$

$$\begin{aligned}
\underline{\xi}^{t}\boldsymbol{Z}\boldsymbol{W}\boldsymbol{Z}\underline{\xi} &= (\underline{\xi}_R + \mathrm{i}\underline{\xi}_I)^{t}\boldsymbol{Z}\boldsymbol{W}\boldsymbol{Z}(\underline{\xi}_R + \mathrm{i}\underline{\xi}_I \\
&= \underline{\xi}_R^{t}\boldsymbol{Z}\boldsymbol{W}\boldsymbol{Z}\underline{\xi}_R - \underline{\xi}_I^{t}\boldsymbol{Z}\boldsymbol{W}\boldsymbol{Z}\underline{\xi}_I
\end{aligned} \tag{C.4}$$

$$\begin{aligned}
\underline{\xi}^{\dagger}\boldsymbol{Z}\boldsymbol{W}\boldsymbol{Z}\underline{\xi}^{*} &= (\underline{\xi}_R - \mathrm{i}\underline{\xi}_I)^{t}\boldsymbol{Z}\boldsymbol{W}\boldsymbol{Z}(\underline{\xi}_R - \mathrm{i}\underline{\xi}_I \\
&= \underline{\xi}_R^{t}\boldsymbol{Z}\boldsymbol{W}\boldsymbol{Z}\underline{\xi}_R - \underline{\xi}_I^{t}\boldsymbol{Z}\boldsymbol{W}\boldsymbol{Z}\underline{\xi}_I
\end{aligned} \tag{C.5}$$

We separate the real and imaginary part

$$\begin{aligned}
&\int \mathrm{d}^2\underline{\alpha}\,\mathrm{d}^2\underline{\gamma'}\,\left\langle \boldsymbol{z'}^*\underline{\gamma'}|\boldsymbol{z}\underline{\alpha}\right\rangle\left\langle \boldsymbol{z'}\underline{\gamma'}|\boldsymbol{z}^*\underline{\alpha}\right\rangle^* \\
=&\int \mathrm{d}\underline{\xi}_R \exp(-\underline{\xi}_R^t(\boldsymbol{I}+\boldsymbol{Z}\boldsymbol{W}\boldsymbol{Z})\underline{\xi}_R + 2\underline{r}^t\boldsymbol{Z}\underline{\xi}_R) \\
&\int \mathrm{d}\underline{\xi}_I \exp(-\underline{\xi}_I^t(\boldsymbol{I}-\boldsymbol{Z}\boldsymbol{W}\boldsymbol{Z})\underline{\xi}_I)
\end{aligned} \tag{C.6}$$

Finally we use $\pi^{-\frac{M}{2}}\int \mathrm{d}\underline{x}\exp(-\underline{x}^t\boldsymbol{A}\underline{x}+2\underline{b}^t\underline{x}) = \det(\boldsymbol{A})^{-\frac{1}{2}}\exp(\underline{b}^t\boldsymbol{A}^{-1}\underline{b})$

$$G(\boldsymbol{Z}) = \det(\boldsymbol{I}-\boldsymbol{Z}\boldsymbol{W}\boldsymbol{Z})^{-\frac{1}{2}}\det(\boldsymbol{I}+\boldsymbol{Z}\boldsymbol{W}\boldsymbol{Z})^{-\frac{1}{2}}\exp(\underline{r}^t\boldsymbol{Z}(\boldsymbol{I}+\boldsymbol{Z}\boldsymbol{W}\boldsymbol{Z})^{-1}\boldsymbol{Z}\underline{r}) \tag{C.7}$$

Appendix D

Occupancy representation with thermal integral kernel

This part illustrates how we obtained equation (2.85) from the generating function ansatz with the thermal integral kernel. The derivations are in analogy to appendix B and therefore shortened.

$$G(\boldsymbol{Z}) = \pi^{-2N} \left|\langle \underline{0'}|\underline{0}\rangle\right|^{-2} \int \mathrm{d}^2\underline{\alpha}\, \mathrm{d}^2\underline{\gamma'} K(\boldsymbol{\Lambda}, \underline{\xi}) \left\langle \boldsymbol{z'}^* \underline{\gamma'}|\boldsymbol{z}\underline{\alpha}\right\rangle \left\langle \boldsymbol{z'}\underline{\gamma'}|\boldsymbol{z}^*\underline{\alpha}\right\rangle^* \tag{D.1}$$

$$K(\boldsymbol{\Lambda}, \underline{\xi}) = \mathcal{N}\det(\boldsymbol{I} + \boldsymbol{\Lambda}) \exp\left(-\underline{\xi}^\dagger \boldsymbol{\Lambda} \underline{\xi}\right) \tag{D.2}$$

$$\underline{\xi} = \begin{pmatrix} \underline{\alpha} \\ \underline{\gamma'^*} \end{pmatrix} \tag{D.3}$$

$$\boldsymbol{\Lambda} = \mathrm{diag}(\lambda_1, \lambda_2, \ldots, \lambda'_1, \lambda'_2, \ldots) \tag{D.4}$$

$$(1 + \lambda_k)^{-1} = \exp(\beta_k \epsilon_k) \tag{D.5}$$

We rewrite the integral:

$$\begin{aligned}
&\mathcal{N} \int \mathrm{d}^2\underline{\alpha}\, \mathrm{d}^2\underline{\gamma'} \det(\boldsymbol{I} + \boldsymbol{\Lambda}) \exp\left(-\underline{\xi}^\dagger \boldsymbol{\Lambda} \underline{\xi}\right) \left\langle \boldsymbol{z'}^* \underline{\gamma'}|\boldsymbol{z}\underline{\alpha}\right\rangle \left\langle \boldsymbol{z'}\underline{\gamma'}|\boldsymbol{z}^*\underline{\alpha}\right\rangle^* \\
=&\mathcal{N} \int \mathrm{d}^2\underline{\alpha}\, \mathrm{d}^2\underline{\gamma'} \sum_{\underline{u},\underline{u'}=\underline{0}}^{\infty} \sum_{\underline{v},\underline{v'}=\underline{0}}^{\infty} \langle \underline{u'}|\underline{u}\rangle \langle \underline{v'}|\underline{v}\rangle^* \det(\boldsymbol{I} + \boldsymbol{\Lambda}) \\
&\prod_{k=1}^{N} \exp(-|\alpha_k|^2(1 + \lambda_k) - |{\gamma'}_k|^2(1 + {\lambda'}_k)) \frac{(z_k)^{u_k + v_k} ({z'}_k)^{{u'}_k + {v'}_k}}{\sqrt{u_k! v_k! {u'}_k! {v'}_k!}} \alpha_k^{u_k} (\alpha_k^*)^{v_k} ({\gamma'}_k^*)^{{u'}_k} {\gamma'}_k^{{v'}_k}
\end{aligned} \tag{D.6}$$

We then use $\alpha = |\alpha| \exp(\mathrm{i}\phi_\alpha)$ and integrate the angular part $\frac{1}{2\pi} \int_0^{2\pi} \mathrm{d}\phi \exp(\mathrm{i}\phi(m -$

$n)) = \delta_{mn}$:

$$
\begin{aligned}
=&2^N \pi^{2N} \mathcal{N} \int_0^\infty \mathrm{d}|\underline{\alpha}| \int_0^\infty \mathrm{d}|\underline{\gamma'}| \sum_{\underline{v},\underline{v'}=\underline{0}}^{\infty} |\langle \underline{v'}|\underline{v}\rangle|^2 \det(\boldsymbol{I}+\boldsymbol{\Lambda}) \\
&\prod_{k=1}^{N} \exp(-|\alpha_k|^2(1+\lambda_k) - |\gamma'_k|^2(1+\lambda'_k))(z_k)^{2v_k}(z'_k)^{2v'_k} \frac{|\alpha_k|^{2v_k+1}|\gamma'_k|^{2v'_k+1}}{v_k! v'_k!}
\end{aligned}
\tag{D.7}
$$

We use $\int_0^\infty \mathrm{d}x \exp(-ax^2)x^{2n+1} = \frac{1}{2}a^{-(n+1)}n!$:

$$
= \pi^{2N} \mathcal{N} \sum_{\underline{v},\underline{v'}=\underline{0}}^{\infty} |\langle \underline{v'}|\underline{v}\rangle|^2 \det(\boldsymbol{I}+\boldsymbol{\Lambda}) \prod_{k=1}^{N} (1+\lambda_k)^{-v_k}(1+\lambda'_k)^{-v'_k}(z_k)^{2v_k}(z'_k)^{2v'_k}
\tag{D.8}
$$

$$
= \pi^{2N} \mathcal{N} \sum_{\underline{v},\underline{v'}=\underline{0}}^{\infty} |\langle \underline{v'}|\underline{v}\rangle|^2 \det(\boldsymbol{I}+\boldsymbol{\Lambda}) \prod_{k=1}^{N} \exp(-v_k\beta_k\epsilon_k)\exp(-v'_k\beta'_k\epsilon'_k)(z_k)^{2v_k}(z'_k)^{2v'_k}
\tag{D.9}
$$

$$
G(\boldsymbol{Z}) = \mathcal{N}\det(\boldsymbol{I}+\boldsymbol{\Lambda}) \sum_{\underline{v},\underline{v'}=\underline{0}}^{\infty} \frac{|\langle \underline{v'}|\underline{v}\rangle|^2}{|\langle \underline{0'}|\underline{0}\rangle|^2} \prod_{k=1}^{N} \left[(z_k)^{2v_k}(z'_k)^{2v'_k}\right] \exp -(\underline{v}^t \boldsymbol{B} \underline{\epsilon} + \underline{v'}^t \boldsymbol{B'} \underline{\epsilon'})
\tag{D.10}
$$

Appendix E

Derivation of the classical number of open channels

This follows closely reference [98] in chapter 4 and illustrates how to derive the classical expression for the number of open channels in equation (2.104).

The number of open channels $W(E)$ corresponds to the integrated density of states, which can be obtained as the inverse Laplace transform of the partition function. The partition function of a classical continuous system is

$$Q = \int g(\Gamma) \mathrm{e}^{-\frac{H}{k_B T}} \, \mathrm{d}\Gamma \tag{E.1}$$

where H is the Hamiltonian of the system and $g(\Gamma)$ is a degeneracy factor. The integration coordinate is the spatial coordinate q and the momentum p.

$$Q = \int \mathrm{d}q \int g(q,p) \mathrm{e}^{-\frac{H}{k_B T}} \, \mathrm{d}p \tag{E.2}$$

The states of a molecule in SACM are approximated as free rotor or harmonic oscillator states. For these we need to derive the partition functions. The Hamiltonian for a one-dimensional rotor is

$$H = \frac{p_\theta^2}{2I} \tag{E.3}$$

and the coordinate q corresponds to an angle θ. This leads to

$$Q = \frac{1}{\sigma h} \int_0^{2\pi} \mathrm{d}\theta \int_{-\infty}^{\infty} \mathrm{e}^{-\frac{{p_\theta}^2}{2 I k_B T}} \, \mathrm{d}p_\theta = \frac{\pi^{\frac{1}{2}}}{\sigma} \left(\frac{k_B T}{B} \right)^{\frac{1}{2}} \tag{E.4}$$

where σ is the symmetry number. It corresponds to the number of rotationally equivalent configurations of a molecule. The inverse Laplace transform is using $L\left[\frac{cx^{p+\frac{u}{2}-1}}{\Gamma(p+\frac{u}{2})}\right] = cs^{-(p+\frac{u}{2})}$ with $s = \frac{1}{k_B T}$, $p = 0$, $u = 1$ and provides the density of states for the one-dimensional rotor.

$$\rho(E) = \frac{1}{\sigma}\left(\frac{1}{BE}\right)^{\frac{1}{2}} \tag{E.5}$$

We can get to the density of states for r one-dimensional free rotors by simply multiplying their partition functions and performing an inverse Laplace transform.

$$Q = \prod_{i=1}^{r} \frac{\pi^{\frac{1}{2}}}{\sigma_i}\left(\frac{k_B T}{B_i}\right)^{\frac{1}{2}} \tag{E.6}$$

$$\rho(E) = \frac{\pi^{\frac{r}{2}} E^{\frac{r}{2}-1}}{\Gamma(\frac{r}{2})} \prod_{i=1}^{r} \frac{1}{\sigma_i}\left(\frac{1}{B_i}\right)^{\frac{1}{2}} \tag{E.7}$$

We obtain the sum of states by integration

$$W(E) = \int_0^\infty \rho(\epsilon)\,\mathrm{d}\epsilon = \frac{\left[\Gamma(\frac{1}{2})\right]^r}{\Gamma(\frac{r}{2}+1)} \prod_{i=1}^{r} \frac{1}{\sigma_i}\left(\frac{E}{B_i}\right)^{\frac{1}{2}} \tag{E.8}$$

Now we do the same for harmonic oscillators. For a one-dimensional oscillator we have

$$H = \frac{p^2}{2\mu} + \frac{1}{2}kx^2 \tag{E.9}$$

$$Q = \frac{1}{h}\int_\infty^\infty \exp -\frac{kx^2}{2k_B T}\,\mathrm{d}x \int_\infty^\infty \exp \frac{-p^2}{2\mu k_B T}\,\mathrm{d}p = \frac{k_B T}{h\nu} \tag{E.10}$$

$$\rho(E) = \frac{1}{h\nu} \tag{E.11}$$

For l harmonic oscillators we get

$$Q = (k_B T)^l \prod_{i=1}^{l}\left(\frac{1}{h\nu_i}\right) \tag{E.12}$$

$$\rho(E) = \prod_{i=1}^{l}\left(\frac{1}{h\nu_i}\right)\frac{E^{l-1}}{(l-1)!} \tag{E.13}$$

This would lead to a sum of states of

$$W(E) = \frac{1}{l(l-1)!}\prod_{i=1}^{l}\left(\frac{E}{h\nu_i}\right) = \frac{1}{\Gamma[l+1]}\prod_{i=1}^{l}\left(\frac{E}{h\nu_i}\right) \tag{E.14}$$

We approximate the anharmonic oscillator sum of states as

$$W(E) = \left(\frac{E}{h\nu}\right)^{x} = \left(\frac{E}{\epsilon}\right)^{x} \tag{E.15}$$

which corresponds to the partition function and density of states

$$Q = \left(\frac{1}{\epsilon}\right)^{x}\frac{\Gamma[1+x]}{(\frac{1}{k_BT})^{x}} \tag{E.16}$$

$$\rho(E) = xE^{x-1}\left(\frac{1}{\epsilon}\right)^{x} \tag{E.17}$$

x and ϵ are in this case fitting parameters. The fitting equations can be found in Ref. [56]. In the case when x is 1 this corresponds to the harmonic oscillator. Multiplication of r partition functions of the free rotor and l partition functions of the anharmonic oscillator results in

$$W(E) = \frac{\left[\Gamma(\frac{1}{2})\right]^{r}\prod_{j=1}^{l}\Gamma(1+x_j)}{\Gamma(\frac{r}{2}+1+\sum_{j=1}^{l}x_j)}\prod_{i=1}^{r}\frac{1}{\sigma_i}\left(\frac{E}{B_i}\right)^{\frac{1}{2}}\prod_{j=1}^{l}\left(\frac{E}{\epsilon_j}\right)^{x_j} \tag{E.18}$$

Bibliography

[1] D. J. Tannor, E. J. Heller, *J. Chem. Phys.* **1982**, *77*(1), 202–218.

[2] C. Wesdemiotis, F. W. McLafferty, *Chem. Rev.* **1987**, *87*(3), 485–500.

[3] J. K. Terlouw, H. Schwarz, *Angew. Chem., Int. Ed.* **1987**, *26*(9), 805–815.

[4] F. W. McLafferty, *Science* **1990**, *247*(4945), 925–929.

[5] N. Goldberg, H. Schwarz, *Acc. Chem. Res.* **1994**, *27*(11), 347–352.

[6] T. Sharp, H. Rosenstock, *J. Chem. Phys.* **1964**, *41*, 3453.

[7] E. Doktorov, I. Malkin, V. Man'ko, *J. Mol. Spectrosc.* **1975**, *56*(1), 1 – 20.

[8] E. Doktorov, I. Malkin, V. Man'ko, *J. Mol. Spectrosc.* **1977**, *64*(2), 302 – 326.

[9] R. Islampour, M. Dehestani, S. Lin, *J. Mol. Spectrosc.* **1999**, *194*(2), 179–184.

[10] L. S. Cederbaum, *J. Phys. B: At. Mol. Phys.* **1975**, *8*(2), 290.

[11] L. Cederbaum, W. Domcke, *J. Chem. Phys.* **1976**, *64*, 603.

[12] W. Domcke, L. Cederbaum, H. Köppel, W. Von Niessen, *Mol. Phys.* **1977**, *34*(6), 1759–1770.

[13] J. Huh, PhD thesis, Johann Wolfgang Goethe-Universität Frankfurt am Main, **2010**.

[14] R. Berger, M. Klessinger, *J. Comput. Chem.* **1997**, *18*(10), 1312–1319.

[15] H.-C. Jankowiak, J. Stuber, R. Berger, *J. Chem. Phys.* **2007**, *127*, 234101.

[16] J. Huh, R. Berger, in *J. Phys.: Conf. Ser.*, Vol. 380, IOP Publishing, Vol. 380, 012019.

[17] D. Lavorato, J. Terlouw, G. McGibbon, et al., *Int. J. Mass Spectrom.* **1998**, *179*, 7–14.

[18] P. Jackson, M. Diefenbach, D. Schröder, H. Schwarz, *Eur. J. Inorg. Chem.* **1999**, *1999*(8), 1203–1210.

[19] X. Chen, F. Tureček, *J. Am. Soc. Mass Spectrom.* **2005**, *16*(12), 1941–1956.

[20] S. Grimme, *Angew. Chem., Int. Ed.* **2013**, *52*(24), 6306–6312.

[21] F. Tureček, *Int. J. Mass Spectrom.* **2003**, *227*(3), 327 – 338.

[22] V. H. Wysocki, H. I. Kenttaemaa, R. G. Cooks, *Int. J. Mass Spectrom. Ion Processes* **1987**, *75*, 181–208.

[23] B. Sztaray, A. Bodi, T. Baer, *J. Mass Spectrom.* **2010**, *45*, 1233 – 1245.

[24] W. D. Phillips, *Rev. Mod. Phys.* **1998**, *70*(3), 721–742.

[25] T. Isaev, S. Hoekstra, R. Berger, *Phys. Rev. A* **2010**, *82*(5), 052521.

[26] W. Ketterle, *Phys. B (Amsterdam, Neth.)* **2000**, *280*(1), 11–19.

[27] M. Di Rosa, *Eur. Phys. J. D* **2004**, *31*(2), 395–402.

[28] E. Shuman, J. Barry, D. DeMille, *Nature* **2010**, *467*(7317), 820–823.

[29] P. F. Staanum, K. Højbjerre, P. S. Skyt, A. K. Hansen, M. Drewsen, *Nat. Phys.* **2010**, *6*(4), 271–274.

[30] I. Manai, R. Horchani, H. Lignier, et al., *Phys. Rev. Lett.* **2012**, *109*(18), 183001.

[31] M. Zeppenfeld, B. G. Englert, R. Glöckner, et al., *Nature* **2012**, *491*, 570.

[32] S. Stenholm, *Rev. Mod. Phys.* **1986**, *58*(3), 699.

[33] J. Javanainen, *Phys.Rev. A* **1992**, *46*(9), 5819.

[34] J. Javanainen, S. M. Yoo, *Phys. Rev. A* **1993**, *48*(5), 3776.

[35] S. Jonsell, C. Dion, M. Nylén, et al., *Eur. Phys. J. D* **2006**, *39*(1), 67–74.

[36] F. Svensson, S. Jonsell, C. Dion, *Eur. Phys. J. D* **2008**, *48*(2), 235–240.

[37] J. Dalibard, Y. Castin, K. Mølmer, *Phys. Rev. Lett.* **1992**, *68*(5), 580.

[38] X.-Y. Wu, B.-J. Zhang, J.-H. Yang, et al., *J. Low Temp. Phys.* **2011**, *164*(5-6), 245–263.

[39] H. Wadi, E. Pollak, *J. Chem. Phys.* **1999**, *110*, 11890.

[40] Y. He, E. Pollak, *J. Chem. Phys.* **2002**, *116*, 6088.

[41] J. Tatchen, E. Pollak, *J. Chem. Phys.* **2008**, *128*(16), 164303–164303.

[42] X. Zhuang, A. Le, T. C. Steimle, et al., *Phys. Chem. Chem. Phys.* **2011**, *13*(42), 19013–19017.

[43] T. A. Isaev, R. Berger, *Phys. Rev. Lett.* **2016**, *116*, 063006.

[44] I. Kozyryev, L. Baum, K. Matsuda, J. M. Doyle, *ChemPhysChem* **2016**, *17*(22), 3641–3648.

[45] R. Dörner, V. Mergel, O. Jagutzki, et al., *Phys. Rep.* **2000**, *330*(2), 95–192.

[46] M. Pitzer, M. Kunitski, A. S. Johnson, et al., *Science* **2013**, *341*(6150), 1096–1100.

[47] K. Vékey, *Mass Spectrom. Rev.* **1995**, *14*(3), 195–225.

[48] D. Schröder, H. Schwarz, *J. Phys. Chem. A* **1999**, *103*(37), 7385–7394.

[49] P. Schwerdtfeger, J. K. Laerdahl, C. Chardonnet, *Phys. Rev. A* **2002**, *65*, 042508.

[50] R. Berger, J. L. Stuber, *Mol. Phys.* **2007**, *105*(1), 41–49.

[51] J. Bondorf, R. Donangelo, I. Mishustin, et al., *Nucl. Phys. A* **1985**, *443*(2), 321–347.

[52] L. S. Kassel, *Proc. N. A. S.* **1928**, *14*, 23–30.

[53] R. A. Marcus, O. K. Rice, *J. Phys. Colloid Chem.* **1951**, *55*, 894–908.

[54] R. A. Marcus, *J. Chem. Phys.* **1952**, *20*, 359–364.

[55] M. Quack, J. Troe, *Berichte der Bunsengesellschaft für physikalische Chemie* **1974**, *78*(3), 240–252.

[56] Troe, *J. Chem. Phys.* **1983**, *79*, 6017.

[57] U. Werner, J. Becker, T. Farr, H. O. Lutz, *Nucl. Instrum. Methods Phys. Res., Sect. B* **1997**, *124*(2), 298–302.

[58] M. Adachi, Y. Saitoh, A. Chiba, et al., *Radiat. Phys. Chem.* **2008**, *77*(10), 1328–1332.

[59] B. T. Psciuk, P. Tao, H. B. Schlegel, *J. Phys. Chem. A* **2010**, *114*(29), 7653–7660.

[60] D. L. Bunker, W.-L. Hase, *J. Chem. Phys.* **1973**, *59*, 4621.

[61] C. Guenat, F. Maquin, D. Stahl, W. Koch, H. Schwarz, *Int. J. Mass Spectrom. Ion Processes* **1985**, *63*(2), 265 – 272.

[62] D. Duflot, J.-M. Robbe, J.-P. Flament, *Int. J. Mass Spectrom. Ion Processes* **1997**, *171*(1), 215 – 230.

[63] R. P. Grant, S. R. Andrews, D. E. Parry, F. M. Harris, *Rapid Commun. Mass Spectrom.* **1998**, *12*(7), 382–388.

[64] R. Grant, F. Harris, D. Parry, *Int. J. Mass Spectrom.* **1999**, *192*(1-3), 111–123.

[65] J. Roithová, J. Žabka, Z. Herman, et al., *J. Phys. Chem. A* **2006**, *110*(20), 6447–6453, pMID: 16706400.

[66] I. Novak, D. B. Li, A. W. Potts, *J. Phys. Chem. A* **2002**, *106*(3), 465–468.

[67] F. Hobi, R. Berger, J. Stohner, *Mol. Phys.* **2013**, *111*(14-15, SI), 2345–2362.

[68] P. A. M. Dirac, *Proc. Roy. Soc. (London) A* **1927**, *114*(767), 243–265.

[69] E. Fermi, *Nuclear Physics*, University of Chicago Press, Chicago, **1950**.

[70] P. R. Bunker, P. Jensen, *Molecular Symmetry and Spectroscopy*, 2 Ed., (Ed.: P. B. Cavers), NRC Research Press, Ottawa, Ontario, Canada, **2006**.

[71] J. K. Watson, *J. Mol. Spectrosc.* **2001**, *207*(2), 276 – 284.

[72] R. J. Glauber, *Phys. Rev.* **1963**, *131*, 2766–2788.

[73] F. Duschinski, *Acta. Physiochim.* **1937**, *7*, 551.

[74] J. K. Watson, *Mol. Phys.* **1968**, *15*(5), 479–490.

[75] N. J. D. Lucas, *Journal of Physics B: Atomic and Molecular Physics* **1973**, *6*(1), 155.

[76] T. Beyer, D. Swinehart, *Comm. Assoc. Comput. Machines* **1973**, *16*, 379.

[77] E. Doktorov, I. Malkin, V. Man'ko, *J. Mol. Spectrosc.* **1979**, *77*(2), 178 – 194.

[78] J. Lorquet, B. Leyh-Nihant, F. McLafferty, *Int. J. Mass Spectrom. Ion Processes* **1990**, *100*, 465–475.

[79] V. P. Maslov, *Theorie des perturbations et methodes asymptotiques*, (Ed.: P. Lelong), Dunod, **1972**.

[80] D. W. H. Swenson, Tracking the Maslov Index, **2008**.

[81] N. Goldberg, M. Iraqi, J. Hrušák, H. Schwarz, *Int. J. Mass Spectrom. Ion Processes* **1993**, *125*(2), 267 – 270.

[82] TURBOMOLE V6.6 2014, a development of University of Karlsruhe and Forschungszentrum Karlsruhe GmbH, 1989-2007, TURBOMOLE GmbH, since 2007; available from `http://www.turbomole.com`.

[83] R. Berger, C. Fischer, M. Klessinger, *J. Phys. Chem. A* **1998**, *102*(36), 7157–7167.

[84] J. Huh, M. Neff, G. Rauhut, R. Berger, *Mol. Phys.* **2010**, *108*(3-4), 409–423.

[85] P. Klán, J. Wirz, *Photochemistry of Organic Compounds: From Concepts to Practice*, John Wiley & Sons Ltd, **2009**.

[86] H. L. Kim, T. J. Kulp, J. D. McDonald, *J. Chem. Phys.* **1987**, *87*(8), 4376–4382.

[87] Y. He, E. Pollak, *J. Phys. Chem. A* **2001**, *105*(49), 10961–10966.

[88] Wolfram Research, Inc., *Mathematica*, 10.0 Ed., **2014**.

[89] M. Pitzer, G. Kastirke, M. Kunitski, et al., *Chem. Phys. Chem.* **2016**, *17*, 2465–2472.

[90] J. G. Hill, K. A. Peterson, *J. Chem. Phys.* **2014**, *141*(9), 094106.

[91] S. Marquardt, S. Marquardt, R. Berger In preparation.

[92] K. A. Peterson, D. Figgen, E. Goll, H. Stoll, M. Dolg, *J. Chem. Phys.* **2003**, *119*(21), 11113–11123.

[93] J. L. Holmes, F. Lossing, R. McFarlane, *Int. J. Mass Spectrom. Ion Processes* **1988**, *86*(Supplement C), 209 – 215.

[94] M. Goto, K. Nakamura, H. Toyoda, H. Sugai, *Jpn. J. Appl. Phys.* **1994**, *33*(6R), 3602.

[95] H. Chatham, D. Hils, R. Robertson, A. Gallagher, *J. Chem. Phys.* **1984**, *81*(4), 1770–1777.

[96] http://cccbdb.nist.gov/elecspin.asp.

[97] J. H. D. Eland, J. Berkowitz, *J. Chem. Phys.* **1977**, *67*(11), 5034–5039.

[98] R. G. Gilbert, S. C. Smith, *Theory of Unimolecular and Recombination Reactions*, (Ed.: J. P. Simons), Blackwell Scientific Publications, **1990**.

Kurzfassung

Theoretische Methoden werden entwickelt und angewandt in Bezug zu drei Gasphasenexperimenten: der Neutralisations-Reionisations-Massenspektrometrie (NRMS), der Laserkühlung und *Cold Target Recoil Ion Momentum Spectroscopy* (COLTRIMS). Alle drei sind wichtige Techniken in der Forschung an Ionenchemie in der Gasphase und können mit ähnlichen theoretischen Modellen beschrieben werden: Die untersuchten Moleküle gehen aus einem anfänglichen elektronischen Zustand in einen finalen elektronischen Zustand über und können dabei auch ihre Schwingungsquantenzahl ändern. Diese vibronischen Übergänge sind im Franck-Condon-Limit beschrieben durch Franck-Condon-Faktoren (FCF), welche die Wahrscheinlichkeit für verschiedene elektronische Übergänge anpassen.

Während in der NRMS Übergänge zwischen Zuständen dazu genutzt werden, hochreaktive molekulare Spezies aus stabilen Vorläufern herzustellen, erreicht Laserkühlung damit Translationskühlung von Molekülen durch wiederholte elektronische Übergänge und COLTRIMS bietet Informationen zur Elektronenstruktur und Geometrie.

In dieser Arbeit wird ein zeitabhängiger Generierendenfunktionsansatz von Huh [13] zur Berechnung von FCFen erweitert, um Populationsverteilungen über Schwingszustände im Endzustand nach einem oder mehreren aufeinanderfolgenden Übergängen zu berechnen. Die berechneten Trajektorien sind in manchen Fällen diskontinuierlich, was Veränderungen im Algorithmus der vorherigen Entwicklungen nötig macht. Die Methode wird auf das Molekül HNSi angewandt und mit Berechnungen von Reaktionsraten nach dem Statistischen Adiabatischen Kanalmodell (SACM) verknüpft, um Signale im Massenspektrum vorherzusagen. Die Ergebnisse werden mit NRMS Experimenten verglichen. Eine erweiterte Version der entwickelten Methode wird diskutiert, welche die Beschreibung der Laseranregung mit spezifischer Frequenz beinhaltet. Sie wird auf ein System mit einem Schwingungsfreiheitsgrad in einem Laserkühlungszyklus angewandt.

Im Jahr 2013 zeigten Pitzer et al., dass eine direkte Bestimmung der Absolutkonfiguration für das Molekül CHBrClF mit COLTRIMS möglich ist. [46] In der vorliegenden Dissertation werden experimentelle Daten aus einem Synchrotronexperiment im Jahr 2016 [89] analysiert. Die Unsicherheit ihrer Auswertung

durch die Isotopenzuordnung wird diskutiert. Gleichgewichtsstrukturen und Stabilitäten mehrfach geladener Kationen von CHBrClF werden mit quantenchemischen Methoden bestimmt. Desweiteren werden die Fragmentierungspfade des einfach geladenen CDBrFI untersucht und Auftrittsenergien mit experimentellen Werten verglichen.

Die Arbeit beschreibt Methoden zur Vorhersage und Analyse dreier Gasphasenexperimente, bei denen vibronische Übergänge beteiligt sind. Diese theoretischen Ansätze vereinbaren verschiedene Vorteile: Die entwickelten oder angewandten Methoden sind überwiegend quantenmechanische Methoden, die intrinsisch eine hohe Genauigkeit aufweisen. Die genutzten Algorithmen und Ansätze nutzen Rechenzeit effizient, da zum Beispiel auf explizites Abzählen von elektronischen Übergängen oder Optimierungen mit übermäßig teuren quantenchemischen Methoden verzichtet wird. Die Methoden sind vielseitig anwendbar auf verschiedene Moleküle in unterschiedlichen Gasphasenexperimenten. Desweiteren leistet diese Dissertation einen Beitrag zur weiteren Entwicklung der vielversprechenden COLTRIMS-Methode zur direkten Bestimmung der Absolutkonfiguration.

Acknowlegements

I thank the Studienstiftung des Deutschen Volkes for the ideational and financial support.

I want to thank Prof. Dr. Robert Berger for the place he gave me in his group. I am thankful that he agreed to supervise this thesis and gave me good advice. I am sure I learned a lot more than I was able to express in this manuscript. I also want to thank Prof. Weitzel and Prof. Tallarek because they were willing to work themselves through my writing. The same is true for my good friend Sebastian Klemenz as well as my colleagues Steffen Giessen and Konstantin Gaul.

I want to say a special thanks to all the people who contributed with their excellent work. Thanks to Martin Pitzer, Markus Schöffler and their colleagues, to Alexander Schießer, Fabian Hobi and Jürgen Stohner.

During the past years I was allowed to meet some wonderful people and I want to acknowledge them here because this would not have happened without this thesis: I thank Hauke Westemeier for he never hesitated to help his colleagues out. I am glad I met Anke Wilm. I enjoyed the time we shared. I thank Dr. Paul Jerabek for being a nice office mate and even trusting me with this plant. (I am so sorry.) I am very thankful for Catharina Schmitt, Cornelia Ritter, Tina Meller and Katharina Fritzen who were good friends not only in the good but also in the hard times. And I want to thank all the colleagues from the Theoretical Chemistry for all the good times.

I am grateful for my parents. You always gave me your love and help. I love you, too.

Now there is one person left who I could have mentioned in all the preceding paragraphs. I thank God for my colleague, best friend, husband and love Sebastian. I would not have achieved this without you.

Danksagungen

Ich danke der Studienstiftung des Deutschen Volkes für die ideelle und finanzielle Unterstützung.

Ich möchte Prof. Dr. Robert Berger für den Platz danken, den er mir in seiner Gruppe gegeben hat. Ich bin dankbar, dass er zugestimmt hat, diese Abschlussarbeit zu betreuen, und auch für die guten Ratschläge, die er mir gab. Ich bin sicher, ich habe mehr gelernt als ich in diesem Manusskript ausdrücken konnte. Ich möchte auch Prof. Weitzel und Prof. Tallarek danken, da sie bereit waren, sich durch meine Niederschrift zu arbeiten. Dasselbe gilt für meinen guten Freund Sebastian Klemenz sowie meine Kollegen Steffen Giessen und Konstantin Gaul.

Ich möchte meinen besonderen Dank all den Menschen ausdrücken, die mit ihrer hervorrangenden Arbeit beigetragen haben. Danke an Martin Pitzer, Markus Schöffler und ihre Kollegen, an Alexander Schießer, Fabian Hobi und Jürgen Stohner.

In den letzten Jahren durfte ich einige wundervollen Menschen kennenlernen und ich möchte dies hier anerkennen, denn dies wäre ohne diese Abschlussarbeit nicht passiert: Ich danke Hauke Westemeier, da er niemals zögerte seinen Kollegen zu helfen. Ich bin froh, dass ich Anke Wilm getroffen habe. Ich habe die gemeinsame Zeit genossen. Ich danke Dr. Paul Jerabek dafür, dass er ein netter Bürokollege war und mir sogar seine Pflanze anvertraute. (Es tut mir sehr leid.) Ich bin sehr dankbar für Catharina Schmitt, Cornelia Ritter, Tina Meller and Katharina Fritzen, die gute Freunde waren, nicht nur in guten, sondern auch in harten Zeiten. Und ich möchte allen Kollegen der Theoretischen Chemie danken für die guten Zeiten.

Ich bin dankbar für meine Eltern. Ihr habt mir immer Liebe und Hilfe gegeben. Ich liebe Euch auch.

Nun ist eine Person übrig, die ich in allen vorhergehenden Absätzen hätte erwähnen können. Ich danke Gott für meinen Kollegen, besten Freund, Ehemann und meine Liebe Sebastian. Ich hätte dies ohne dich nicht erreicht.

Wissenschaftlicher Werdegang

Sabrina Marquardt (geb. Kemmerer)
*20.09.1987 in Hanau am Main
Staatsangehörigkeit: deutsch

BILDUNGSWEG

Seit 2013-12	Promotion, Technische Universität Darmstadt und Philipps Universität Marburg, *Development of low-scaling methods for the description of vibronic transitions and application in gas-phase ion chemistry*, Betreuer: Prof. Dr. Robert Berger
2010-10 – 2013-03	Masterstudium Chemie, Technische Universität Darmstadt, Master Thesis: *MD Simulation of DPPC, modified with a nitroxide spin label, in a lipid membrane*, Betreuer: Prof. Faller (UC Davis) und Prof. Dr. Florian Müller–Plathe
2011-09 – 2012-09	Studium an der *University of California Davis*
2007-10 – 2010-10	Bachelorstudium Chemie, Technische Universität Darmstadt, Bachelor Thesis: *Free Volume determination Methods for the analysis of Molecular Dynamics results*, Betreuer: Prof. Dr. Florian Müller–Plathe
2007-07 – 2007-09	Sommerschule Chemie an der Universität Paderborn
1998-09 – 2007-07	Gymnasium an der Marienschule der Ursulinen in Offenbach am Main

AUSZEICHNUNGEN UND STIPENDIEN

2015-06	Teilnahme am Lindau Nobel Laureate Meeting
2013-12 – 2016-05	Promotionsstipendium der Studienstiftung des Deutschen Volkes
2013-01 – 2013-06	Stipendium der Studienstiftung des Deutschen Volkes
2011-10 – 2012-10	Deutschlandstipendium
2010-12	Preis der Dr. Anton Keller Stiftung für sehr gute Leistungen in der B.Sc. Chemie-Abschlussprüfung